Modeling and Coordinating Distributed Energy Resources in Power Systems and Markets

Final Project Report

M-42

Power Systems Engineering Research Center

Empowering Minds to Engineer
the Future Electric Energy System

Modeling and Coordinating Distributed Energy Resources in Power Systems and Markets

Final Project Report

Project Team
Meng Wu, Project Leader
Vijay Vittal
Arizona State University

Alejandro Dominguez-Garcia
University of Illinois Urbana-Champaign

Graduate Students
Adriana Cisco Sullberg
Mohammad Mousavi
Arizona State University

Siddhartha Nigam
Temitope Amuda
University of Illinois Urbana-Champaign

PSERC Publication 22-02

October 2022

For information about this project, contact

Meng Wu
Arizona State University
School of Electrical, Computer, and Energy Engineering
P.O. BOX 875706
Tempe, AZ 85287-5706
Phone: 480-965-8706
Email: mwu@asu.edu

Power Systems Engineering Research Center

The Power Systems Engineering Research Center (PSERC) is a multi-university Center conducting research on challenges facing the electric power industry and educating the next generation of power engineers. More information about PSERC can be found at the Center's website: http://www.pserc.org.

For additional information, contact:

Power Systems Engineering Research Center
Arizona State University
527 Engineering Research Center
Tempe, Arizona 85287-5706
Phone: 480-965-1643
Fax: 480-727-2052

Notice Concerning Copyright Material

Acknowledgments

This is the final report for the Power Systems Engineering Research Center (PSERC) research project titled "Modeling and Coordinating Distributed Energy Resources in Power Systems and Markets" (Project M-42).

The authors would like to thank all the industry advisors for their valuable feedback: Deepak Ramasubramanian (EPRI), Bo Gong (SRP), Hung-Ming Chou (Dominion Energy), Bernardo Orvananos (Centrica), Qiang Zhang (ISO-NE), Di Shi (GEIRI North America), Miaolei Shao (GE), Yingchen Zhang (NREL), Jianzhong Tong (PJM), Aung Oo (CAISO), Yohan Sutjandra (The Energy Authority).

Executive Summary

This project is motivated by the growing integration of distributed energy storage resources (DERs) in the electric power systems. The massive DER integration brings significant voltage stability challenges to the transmission and distribution systems, as well as wholesale market challenges and opportunities to the independent system operators (ISOs) and DER aggregators. This research focuses on three core areas: 1) mitigating fault induced delayed voltage recovery (FIDVR) by using DERs and variable frequency drive (VFD) driven air conditioners; 2) coordinating transmission and distribution operations for massive DER integration in the wholesale electricity markets; and 3) DER coordination for frequency regulation service provision. The research is presented in five chapters (Chapters 2-6).

Chapters 2-3 propose FIDVR mitigation techniques by using DERs and VFD driven air conditioners. By properly modeling the VFD driven air conditioners, which is a relatively new technology in residential air conditioning, in the composite dynamic load models, these chapters investigate the impact of increasing VFD driven air conditioner penetration and DER penetration within a large-scale power system on reducing the severity of FIDVR events.

Chapters 4-5 propose transmission and distribution coordination frameworks which enables the wholesale market participation of massive DERs while ensuring secure operation of the distribution grids. A non-profit distribution system operator (DSO) is adopted as the coordinator between the wholesale market operation and the distribution grid operation. A parametric programming approach and a two-stage stochastic programming approach are proposed for the DSO to coordinate the wholesale market participation of aggregated DERs while satisfying the distribution grid operating constraints.

Chapter 6 presents and implements the centralized and distributed methodologies which enable the microgrids to coordinate multiple DERs in order to provide frequency regulation services to the bulk power systems. Details on the controller hardware-in-the-loop (CHIL) testbed that is used to test the centralized and distributed DER coordination approaches are presented in this chapter.

Project Publications

[1] Mohammad Mousavi and Meng Wu, "A Two-stage Stochastic Programming DSO Framework for Comprehensive Market Participation of DER Aggregators under Uncertainty", *52nd North American Power Symposium (NAPS)*, Virtual Conference, 2021.

[2] Adriana Cisco Sullberg, Meng Wu, Vijay Vittal, Bo Gong and Philip Augustin, "Examination of Composite Load and Variable Frequency Drive Air Conditioning Modeling on FIDVR," in IEEE Open Access Journal of Power and Energy, vol. 8, pp. 147-156, 2021.

[3] Mohammad Mousavi and Meng Wu, "A DSO Framework for Comprehensive Market Participation of DER Aggregators in Unbalanced Distribution Networks", in *IEEE Transactions on Power Systems*, vol. 37, no. 3, pp. 2247-2258, May 2022.

[4] Mohammad Mousavi and Meng Wu, "ISO and DSO Coordination: A Parametric Programming Approach", *2022 IEEE Power & Energy Society General Meeting (PESGM)*, Denver, Colorado, July 2022.

Industry Advisors

Deepak Ramasubramanian	EPRI	dramasubramanian@epri.com
Bo Gong	SRP	Bo.Gong@srpnet.com
Hung-Ming Chou	Dominion Energy	hung-ming.chou@dominionenergy.com
Bernardo Orvananos	Centrica	Bernardo.Orvananos@centrica.com
Qiang Zhang	ISO New England	qzhang@iso-ne.com
Di Shi	GEIRI North America	di.shi@geirina.net
Miaolei Shao	GE	miaolei.shao@ge.com
Yichen Zhang	NREL	yingchen.zhang@nrel.gov
Jianzhong Tong	PJM	Jianzhong.Tong@pjm.com
Aung Oo	CAISO	aoo@caiso.com
Yohan Sutjandra	The Energy Authority	ysutjandra@teainc.org

Table of Contents

List of Figures

List of Tables

1. Introduction

1.1 Background

This project is motivated by the growing integration of DERs in the electric power systems. As US Federal Energy Regulatory Commission (FERC) Order No. 2222 requests all the US system operators to completely open their wholesale electricity markets to the aggregated DERs, the massive adoption of DERs brings significant voltage stability challenges to the transmission and distribution systems, as well as wholesale market challenges and opportunities to the system operators and DER aggregators. Specifically, the following challenges are identified in this project:

- In the distribution grids with high penetration of single-phase air conditioner loads, the fault induced delayed voltage recovery (FIDVR) events have become a credible concern. To investigate FIDVR events in power system planning studies, dynamic load models such as the Western Electricity Coordinating Council (WECC) composite load model are widely adopted. As DERs and other power electronics interfaced loads, such as the variable frequency drive (VFD) driven air conditioners, increase their penetration in the distribution grids, their impacts on the FIDVR events need to be further modeled and studied. FIDVR mitigation approaches using DERs and VFD driven air conditioners can also be investigated after proper modeling of these impacts.
- The massive integration of numerous small DER aggregators into the wholesale electricity markets causes several challenges for the ISOs and distribution grid operations: 1) it imposes complexity and computational burden to the unit commitment and economic dispatch process of the ISOs; 2) it could cause distribution grid voltage/thermal violations if the aggregator-controlled DERs are not properly monitored by the distribution grid and the ISOs. An effective coordination framework among the ISO, the distribution grid, and the DER aggregators is needed to ensure the distribution grid operational security and reliability while enabling the wholesale market participation of the aggregated DERs.
- To enable DER aggregators for providing grid services, the DER aggregators need to properly coordinate and control numerous DERs across the distribution grid for aggregated grid service provision by following the dispatch signals and frequency regulation signals of the ISO.

This project aims at solving the above challenges in the following aspects.

- FIDVR mitigation techniques by using DERs and VFD driven air conditioners are proposed. By properly modeling the VFD driven air conditioners, which is a relatively new technology in residential air conditioning, in the composite dynamic load models, this project investigates the impact of increasing VFD driven air conditioner penetration and DER penetration within a large-scale power system on reducing the severity of FIDVR events.
- The transmission and distribution coordination frameworks are proposed, which enables the wholesale market participation of massive DERs while ensuring secure operation of

the distribution grids. A non-profit distribution system operator (DSO) is adopted as the coordinator between the wholesale market operation and the distribution grid operation. A parametric programming approach and a two-stage stochastic programming approach are proposed for the DSO to coordinate the wholesale market participation of aggregated DERs while satisfying the distribution grid operating constraints.

- The centralized and distributed methodologies which enable the coordination of multiple DERs are presented and implemented in order for the aggregated DERs to provide frequency regulation services to the bulk power systems. Details on the controller hardware-in-the-loop (CHIL) testbed that is used to test the centralized and distributed DER coordination approaches are presented in this project.

1.2 Project Outcomes

The project outcomes and major contributions are summarized below for each chapter of this report.

1.2.1 FIDVR Mitigation using VFD Driven Air Conditioners

Chapter 2 presents a simple method for modeling VFD driven air conditioners as the power electronic load within the composite load model and shows that increasing the penetration of VFD driven air conditioner load leads to reduced severity of FIDVR events. Case studies on practical large-scale power system models show that as the percentage of new air conditioners which are VFD driven increases, the voltage sag following the FIDVR event is less severe, and the time for the voltage to recover to the pre-fault value is shortened. There are also fewer operations of under-voltage load shedding (UVLS) relays as the penetration of VFD driven air conditioners increases, resulting in fewer customers being adversely impacted by the FIDVR event. The increase in VFD driven air conditioners improves post-fault conditions but does not completely eliminate the FIDVR events from occuring.

1.2.2 FIDVR Mitigation using DERs

Built upon the models and studies in Chapter 2, Chapter 3 further investigates the impact of increased DER penetration on the severity of FIDVR events. The DER_A model is adopted to represent the rooftop solar panels in this study. Different categories of DERs defined in IEEE Std 1547-2018 are modeled and their dynamic voltage responses are investigated. The improvement in post-fault voltage sag and voltage recovery time after FIDVR is studied following an increase in the penetration of different categories of DERs.

1.2.3 Transmission and Distribution Coordination for DER Wholesale Market Participation: A Parametric Programming Approach

Chapter 4 presents a framework for the DER aggregators to participate in the wholesale markets while ensuring the distribution grid operational security. The proposed framework is built upon

a non-profit DSO entity which handles the market participation of the DER aggregators in the retail level within its territory. The DSO builds the bid-in cost function to be submitted to the ISO, considering its retail market participants' (i.e., the DER aggregators') offering prices and their operational constraints as well as the physical constraints of teh distribution grid including power balance equations and voltage limitation constraints. Different from existing approaches facing computational difficulties for large-scale ISO-DSO coordination, this work could lead to a coordinated ISO-DSO market clearing procedure which is computationally efficient and scalable toward large-scale systems with many DSOs and numerous DER aggregators.

1.2.4 A Two-stage Stochastic Programming DSO Framework for Comprehensive Market Participation of DER Aggregators under Uncertainty

Chapter 5 presents a DSO framework for comprehensive market participation of DER aggregators under uncertainty in the distribution-level retail market as well as the transmission-level wholesale energy and regulation markets. The proposed DSO framework adopts two-stage stochastic programming for considering uncertainty in the market participation of DER aggregators. Various DER aggregators, including the energy storage aggregators (ESAGs), demand response aggregators (DRAGs), electric vehicle (EV) aggregating charging stations (EVCSs), dispatchable distributed generation (DDG) aggregators (DDGAGs) are considered. The proposed DSO optimally coordinates these DER aggregators for their participation in the retail market and wholesale energy and regulation markets, while maintaining distribution grid security.

1.2.5 DER Coordination for Frequency Regulation Service Provision

Chapter 6 reviews the DER coordination problem with small power systems referred to as microgrids. The centralized as well as distributed solution methologies and their implementation that enables microgrids to coordinate multiple DERs are proposed in order for the microgrids to provide frequency regulation services to the bulk power grid. Details on the controller hardware-in-the-loop (CHIL) testbed that is used extensively to test the centralized as well as distributed approaches are provided. This chapter also provides results obtained as part of the testing of the centralized and distributed DER coordination approaches in the Banshee distribution system operated as a microgrid. A review of the ratio consensus algorithm that is used as the basis for the distribution DER coordination approach within a microgrid is also provided in the appendix.

1.3 Report Organization

The report is organized as follows. Chapter 2 presents the modeling approaches for VFD driven air conditioners and the FIDVR mitigation approaches using VFD driven air conditioners. Chapter 3 investigates the impact of enabling DER controls and increasing DER penetration levels on the severity of FIDVR events. Chapter 4 presents the parametric-programming-based DSO framework which coordinates the wholesale market clearing process and the distribution grid operations. The DSO builds the bid-in cost function based on the distribution system market considering its distribution-level market participant constraints and the distribution system physical constraints

including the power balance equations and voltage limitation constraints. The DSO submits the resulting bid-in cost function to the wholesale market operated by the ISO. After the clearance of the wholesale market, the DSO determines the share of its retail market participants (i.e., DER aggregators). Chapter 5 presents a two-stage stochastic programming based DSO for handling uncertainties of DERs in the distribution-level retail market. Chapter 6 presents the centralized and distributed DER coordination approaches for frequency regulation service provision to the bulk power system and the CHIL testing results of the proposed centralized and distributed approaches. Chapter 7 provides concluding remarks to this report.

2. FIDVR Mitigation using VFD Driven Air Conditioners

Nomenclature

α_{VFD} Penetration of VFD air conditioners among new air conditioners.
ρ'_{VFD} Percentage of VFD driven air conditioners in the power system
ρ_i Percentage of homes with new air conditioners at bus i
$\rho_{VFD,i}$ Percentage of new air conditioners which are VFD driven at bus i
A_{new} Age less than which an air conditioner is considered new, years
A_{rep} Age at which an air conditioner is replaced, years
f_{cn} Fraction of Motor D tripped by contactor tripping
F_{rst} Fraction of Motor D which can restart after stalling
Fel Fraction of the load modeled as power electronic in CMPLDW in the base case
Fel_0 Fraction of the load modeled as power electronic in CMPLDW in the VFD penetration case study
Fma Fraction of the load modeled as Motor A in CMPLDW in the VFD penetration case study
Fma_0 Fraction of the load modeled as Motor A in CMPLDW in the base case
Fmb Fraction of the load modeled as Motor B in CMPLDW in the VFD penetration case study
Fmb_0 Fraction of the load modeled as Motor B in CMPLDW in the base case
Fmc Fraction of the load modeled as Motor C in CMPLDW in the VFD penetration case study
Fmc_0 Fraction of the load modeled as Motor C in CMPLDW in the base case
Fmd Fraction of the load modeled as Motor D in CMPLDW in the VFD penetration case study
Fmd_0 Fraction of the load modeled as Motor D in CMPLDW in the base case
Fmd_i Percentage of load which is single-phase motor load at bus i
$Frcel$ Fraction of the power electronic load which can reconnect after the voltage sags in the VFD penetration case study
$Frcel_0$ Fraction of the power electronic load which can reconnect after voltage sags, in the base case
fth_A Fraction of type A Motor D motors not tripped by thermal protection
fth_B Fraction of type B Motor D motors not tripped by thermal protection
fuv_{tr} Fraction of Motor D with undervoltage relay protection
N_{H_i} Total number of homes at bus i
$N_{H_{new}}$ Number of homes with new air conditioners
$N_{H_{y,i}}$ Number of homes built in year y at bus i
P_{1_0} Load represented by CMPLDW in the base case, MW
P_1 Load represented by CMPLDW in the VFD penetration case study, MW
P_2 VFD air conditioner load represented by LD1PAC in the VFD penetration case study, MW
P_{load_i} Real power load at bus i, MW
R_{stall} Stall resistance, pu
T_{rst} Time delay for F_{rst} fraction of stalled Motor D begins restarting, pu
T_{stall} Time delay for single phase motor stalling, pu
T_{th} Motor D thermal protection time constant, sec
t_{tr1} Motor D unvdervoltage relay time delay 1, sec

t_{tr2} Motor D unvdervoltage relay time delay 2, sec
Th_{1t} Motor D thermal protection trip start level, pu
Th_{2t} Motor D thermal protection trip completion level, pu
uv_{tr1} Motor D unvdervoltage relay voltage setpoint 1, pu
uv_{tr2} Motor D unvdervoltage relay voltage setpoint 2, pu
V_{rst} Voltage at which F_{rst} fraction of stalled Motor D begins restarting, pu
V_{stall} Voltage at which single phase motors stall, pu
V_{tr_1} Power electronic load begin trip voltage, pu
V_{tr_2} Power electronic load finish trip voltage, pu
Vc_{1off} Voltage at which power electronic load begins to disconnect, pu
Vc_{1on} Voltage at which power electronic load begins to reconnect, pu
Vc_{2off} Voltage at which 100% of power electronic load is disconnected, pu
Vc_{2on} Voltage at which 100% of power electronic load is reconnected, pu
X_{stall} Stall reactance, pu
y A given year
Pdgen Real power generator by DER at a load bus in the power flow load table
tv Time constant for voltage and frequency cut-out, sec
tvh0 High voltage cut-out of timer, sec.
tvh1 High voltage cut-out of timer, sec.
tvl0 Low voltage cut-out of timer, sec
tvl1 Low voltage cut-out of timer, sec
vfrac Fraction of device that recovers after voltage returns within vl1 and vh1
vh0 Voltage break-point for high voltage cut-out of the inverter, pu
vh1 Voltage break-point for high voltage cut-out of the inverter, pu
vl0 Voltage break-point for low voltage cut-out of the inverter, pu
vl1 Voltage break-point for low voltage cut-out of the inverter, pu

2.1 Introduction

Fault induced delayed voltage recovery (FIDVR) is a transient of sustained low bus voltage and can occur in power systems with high penetration of single-phase motor loads, most commonly residential air conditioner motors. Power systems located in geographical climates with very high summer temperatures rely heavily on central air conditioning; therefore, single phase motors make up a large percentage of load composition. Furthermore, environments which have not historically used air conditioning during the summer months have increasing air conditioner penetration due to climate change [5]. This trend is seen globally in both areas of high and low income, and trend emphasizes the importance of mitigation of FIDVR [6].

2.1.1 Fault Induced Delayed Voltage Recovery

When a fault causes low bus voltage, the electric torque developed in an induction motor will decrease proportional to voltage. If the electric torque developed is not enough to overcome the mechanical torque required by the load (air conditioner compressor), the motor will stall. Stalled induction motors draw high reactive current from the power system. Inadequate reactive power

availability will keep bus voltage low. FIDVR events are also characterized by an overvoltage following the sustained period of low voltage.

While the motor stalling causes sustained periods of low voltage, a number of protective and corrective measures may act, typically automatically, to restore the voltage [7]. In some rare cases, the air conditioners might have an undervoltage relay installed on the unit, which will disconnect the unit and prevent stalling. All residential air conditioners are equipped with thermal overload protective devices. These are simple bimetallic strip or solder-pot devices which operate on the order of seconds to disconnect the motor to prevent thermal damage to motor windings. Load may be disconnected from system subtransmission or distribution buses by protective relaying; stalling may cause overcurrent relay operation in the distribution system, three-phase, inverter-interfaced loads, and/or other loads equipped with undervoltage protection may disconnect, or the bus voltage can cause actuation of undervoltage load shedding relays. NERC requires utilities to maintain a undervoltage load shedding program to ensure system stability and reliability in the event of low system voltage [8] [9].

High bus voltage following sustained low voltage is typical and is caused by capacitor banks and similar var-supplying equipment remaining connected after the stalled air conditioners have been disconnected from the system. Capacitor banks provide reactive power and act to raise the system voltage during heaving loading. They will remain connected for a period of time where is there is a system overvoltage following the period of undervoltage. The FIDVR event is fully recovered once loads are reconnected, generator excitation levels are stable, and system voltage is stable. Information about real FIDVR events in the Southern California Edison system can are in [10] [11] [12].

FIDVR is sensitive to ambient temperature and the point-on-wave at which the fault occurred. Higher ambient temperatures result in more sever FIDVR events [13] [7]. The point-on-wave at which the fault occurs is a strong indicator of how severe a FIDVR event will be, with events more severe when the voltage sag happens closer to a zero-crossing [14]. Positive sequence transient stability tools are not able to model the impact of point-on-wave data. Hybrid simulations between electromagnetic transient and transient stability simulations have been used to study point-on-wave simulations for FIDVR [15]. Point-on-wave measurement data has been used in [16] to estimate load composition and single-phase induction motor electrical parameters. Point-on-wave measurement devices are in widespread use in distribution systems [17]. Supply voltage rate-of-change also impacts FIDVR, and modeling considerations are discussed in section 2.1.2.

FIDVR detection, mitigation, and correction is an active area of research. Load shedding is determined by a motor kinectic-energy based model to mitigate FIDVR faster than traditional unvervoltage load shedding relays in [18]. A faster-than-real-time digital replica with a FIDVR detection algorithm used to minimize load shedding during FIDVR is proposed in [19]. An dynamic optimization with input from time-domain analysis to determine the size and location of sataic var compensators to reduce FIDVR recovery time is proposed in [20]. Reference [21] real-time voltage trajectories and a self-adaptive probabilistic predication model to quickly detect FIDVR events and allow FIDVR mitigation controls to take effect earlier. Reference [22] proposes a low voltage ride through scheme for industrial buses which are affected by FIDVR, by momentarily overriding

undervoltage relay time delay settings based when FIDVR is detected by a time delay, not dissimilar to T_{stall}, between the fault and current increase from motors stalling. Additional relevant literature is described in their related sections of this report.

2.1.2 WECC Composite Load Modeling and Modeling FIDVR

Load modeling is fundamental to power system studies, and continues to evolve as computational power increases and more is expected of study results. The Western Electricity Coordinating Council (WECC) Load Modeling Task Force was (LMTF) was instrumental in developing more sophisticated load models, building on constant-impedance, constant-current, constant-power (ZIP) load models and other early aggregate-component based models. Part of the drive to improve load models was the need to be able to capture FIDVR event in dynamic simulations, which is not possible with ZIP models, or component models with only three-phase motors [23]. NERC Reliability Standard TPL-001-4 Requirement R2.4.1 requires the use of dynamic load models of induction motors in planning studies and suggests the use of an aggregate dynamic load model [24]. As mentioned in 2.1.1, FIDVR is also often studied in electromagnetic transient simulations. Reference [25] proposes modeling and studying FIDVR in time series power flow or "quasi-static" simulation environments. The rest of this section focuses on modeling and simulation in positive sequence transient stability simulations.

WECC developed the composite load model CMPLDW to model the most common consumer loads in an aggregated fashion. The CMPLDW model contains a representation of a distribution feeder, four types of induction motors – Motors A, B, C, and D, typically with Motors A-C representing three types of three-phase motors and Motor D representing the single-phase motor – the electronic load and the static load. It has been able to successfully reproduce recorded FIDVR events [26]. Figure 2.1 depicts the WECC CMPLDW.

While easing the modeling burden by not modeling each load type independently, the WECC CMPLDW model is complex with a large number (121) of user-defined parameters to characterize the loads [4]. Many of the parameters related to component protection functions have been determined by conducting laboratory tests and reviews of manufacturer literature for devices reported being used during end-use surveys and are typically left unchanged by users. A smaller number of parameters are related to load composition and are meant to be modified based on utility feeder-specific data, such as Fma, Fmb, Fmc, Fmd, and Fel. Both Pacific Northwest National Laboratory (PNNL) and the Electric Power Research Institute (EPRI) have developed software to assist CMPLDW model users adjust model parameters if there is insufficient feeder-specific data available to system planners [27] [28] [29]. The load modeling tools rely on user input of season, operating hour, climate zone, and load type percentages. NERC published a list of typical CMPLDW parameter values and provided guidance regarding the specific parameters that need to be tuned [30]. NERC also suggests that the parameters for which sensitivity studies are most necessary are load composition, three-phase motor voltage trip and reconnection settings, single-phase motor stalling, percentage of single-phase mtors which can recover from stalling, and feeder impedance [24].

Parameter identifiability and estimation for composite load models is an active area of research. An improved particle swarm optimization algorithm as an improvement upone genetic-algorithm

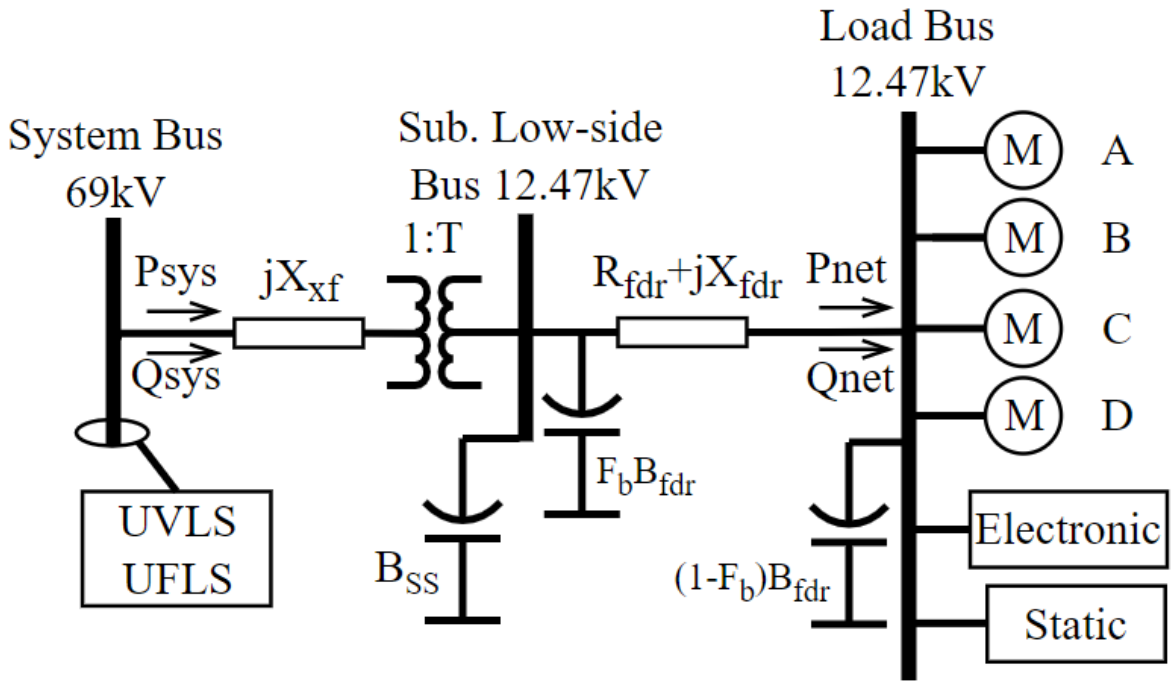

Figure 2.1: One-line diagram of the CMPLDW model [1].

based parameter estimation is proposed in [31]. Parameter sensitivity analysis results are used to weight parameters using a evolutionary deep reinforcement learning to efficiently identify composite load model parameter in [32]. Parameter sensitivity and dependency analysis is used to reduce the number of parameters to be estimated using an interative linear least-squares method in [33]. Parameter dependency and a nonlinear least-squares method with *a priori* parameter value information is used for parameter estimation in [34]. CMPLDW was implemented in open-source software GridPACK for use with the goal that researches can test improvements to the CMPLDW model [35].

Single-Phase Motor Modeling in CMPLDW

In positive sequence power system simulation tools such as GE PSLF®, single-phase motor dynamics, unlike those of three-phase motors, cannot be represented by a suitable dynamic model. Instead, a performance model is used. The performance model is a state-model which uses algebraic equations to calculate motor power in two states: a run state and a stall state. Motor protection is also modeled, which includes the effect of disconnecting the motor and having zero output power. The motor state is characterized by user-defined CMPLDW parameters.

The model of the single-phase motor (Motor D) within the CMPLDW representation is a performance model. In GE PSLF®software, the single-phase motor model, "uses essentially the same model as the LD1PAC model" [4]. The fraction of the load to be represented using Motor D in

CMPLDW is determined by the parameter Fmd. LD1PAC and Motor D in CMPLDW, model compressor motor stalling and reconnection as well as three internal tripping mechanisms: contactor tripping, undervoltage relay protection, and thermal overload protection. Figure depicts a oneline diagram for the single-phase motor (Motor D) performance model.

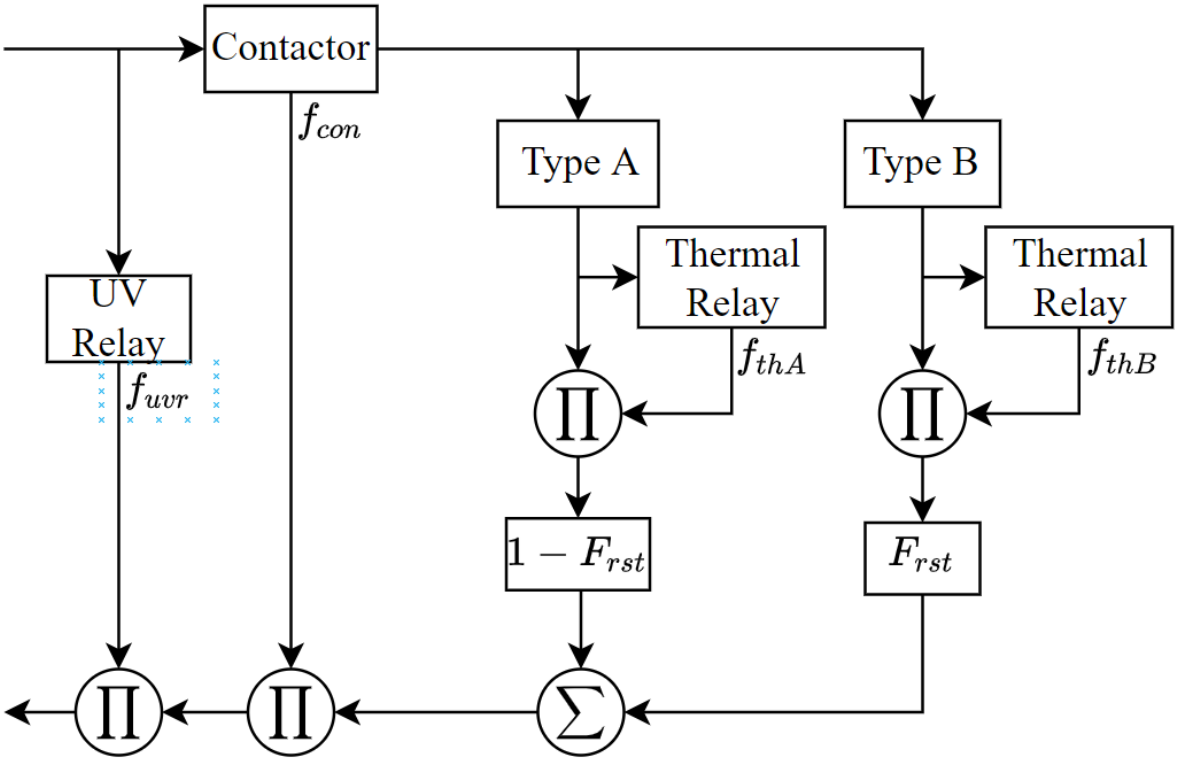

Figure 2.2: One-line diagram of the CMPLDW model [1].

Motor Stalling One hundred percent of the aggregate single-phase motor stalls when the voltage at its terminals falls below V_{stall} for T_{stall} seconds, at which point it is represented as a constant impedance load of $R_{stall} + jX_{stall}$. If the voltage recovers above V_{rst} for T_{rst} seconds, a fraction of the load, F_{rst}, restarts. Parameter F_{rst} is used to split the single-phase motor load into two types, type A and type B. The type A motors are not allowed to restart after stalling, and the type B motors are allowed to restart.

The voltage supply rate-of-change is also determining factor in the severity of FIDVR. Built into the LD1PAC and CMPLDW models in GE PSLF®is an experimentally derived voltage dependent stall time (VDST) curve. This curve is utilized if $T_{stall} < 0$ [24]. At each time step V_{stall} is compared to the look up table depicted in Table 2.1, and T_{stall} is updated accordingly.

Thermal Protection When motors represented as type A or type B are stalled, the thermal overload protection is then modeled. The current and R_{stall} parameter of each set of motors is used to determine a motor temperature. The heat, I^2R_{stall}, is integrated with a time constant of

Table 2.1: Voltage Dependent Stall Time Lookup Table [4]

T_{stall} (cycles)	V_{stall} (pu)
3	0.46
6	0.53
9	0.55
12	0.565
15	0.57

T_{th}. The load linearly trips from temperatures Th_{1t} to Th_{2t}, at which point 100% of that motor load is tripped. This calculation and procedure are performed independently for type A and type B motors. This portion of the model represents the overload protection common in motor starters. A diagram of the thermal protection tripping scheme is shown in Figure 2.3. The fraction of type A and type B motors which are not tripped is output as fth_A and fth_B.

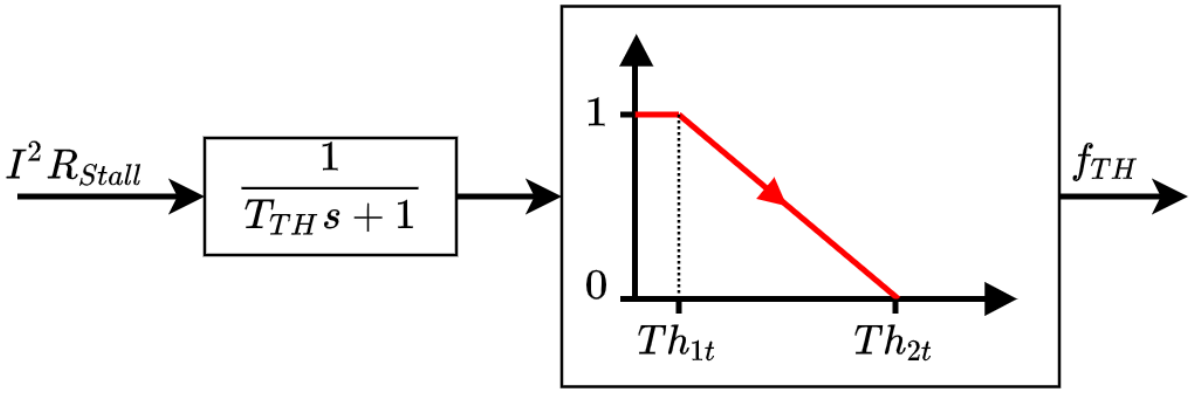

Figure 2.3: 3 Motor D thermal protection tripping scheme [1].

Motor starters typically consist of an electromagnetic contactor in series with an overload device. In small motors, overload devices are usually bimetallic strips or solder-pots in series with the motor [30]. When the motor stalls due to a mechanical failure, such as wiped bearings, or has excess current caused by electrical failures such as single-phasing (in three-phase motors, when one phase is open circuited), the thermal overload will open and disconnect the motor from its source.

Both bimetallic strips and solder-pots operate over an electrically long period of time, in the order of many seconds. Overloads and thermal protection, despite operating due to elevated motor current, is not to be confused with overcurrent protection, which operates in a much faster time frame and protects against electrical faults.

Thermal overload devices can be manually-resetting but are most often automatically resetting in consumer appliances. When the temperature of the overload device decreases, the overload will close and reconnect the motor to its power source. When reconnected, the motor could either stall or not stall. If the cause of the stall is a more permanent issue, such as failed bearings, it is likely that the motor will continue to stall after the overload resets. However, if the cause of stalling is

temporary, such as low voltage, the motor may reconnect and operate normally.

Contactor Tripping Single-phase motors in CMPLDW and LD1PAC experience contactor tripping beginning at voltages of Vc_{1off} to Vc_{2off}, at which point 100% the single-phase motors are tripped [4]. The motors begin to reconnect starting at voltages of Vc_{2on} to Vc_{1on}, at which point 100% of single-phase motors are reconnected. A linear fraction of the load is either tripped or reconnected if the voltage is between the voltage thresholds. All single-phase motors are subject to contactor tripping. There is no time delay for the contactor tripping scheme unlike with motor stalling or thermal protection tripping. The fraction of motors not tripped is output as f_{cn}.

All air conditioners use a contactor to start the compressor motor – it therefore makes sense that there is not a model parameter for the fraction of single-phase motors which have contactor tripping. Contactors are electromagnetic switching devices which typically use a low voltage signal to power an electromagnet which closes the contacts for a higher power application. In the case of residential air conditioners in the United States, the air conditioner control scheme generally relies on a 24V signal from the thermostat, to close a 208V contactor, thereby energizing the compressor motor and providing cooling to the residence.

Low voltage can cause contactor contacts to open and disconnect the motor from its power source. The study of contactors dropping out due to low voltage is important to many industries which may lose significant revenue due to critical motor loads being in-terrupted. References [36] and [37] both study contactors dropping out, but do not discuss when contactors pick back up when voltage recovers. Customer end-use surveys were conducted in order to better understand the effect of voltage sags on residential customers in [38]. In addition to studying contactor drop out voltage, [38] also discusses the time required for contactors to pick up when voltage recovers. The future work section of [16] discusses how their approach to using electromagnetic transient point-on-wave simulation can be used for parameter estimation related to contactor models in the composite load.

Undervoltage Relay Protection Both type A and type B motors can be tripped due to undervoltage relaying, which is modeled in parallel to the contactor and thermal protection tripping, and stalling. A fraction, fuv_{tr}, of single-phase motors will trip if terminal voltage is at uv_{tr1} for t_{tr1} seconds. Similarly, a fraction, fuv_{tr}, of single-phase motors will trip if at a lower terminal voltage uv_{tr2} for t_{tr2} seconds. Motors tripped due to undervoltage relay protection are not reconnected. The fraction of the load tripped is not cumulative [1]. Few residential air conditioners, or other consumer appliances, utilize undervoltage relay protection [30].

Unvervoltage Load Shedding and CMPLDW In GE PSLF®, each portion of the CMPLDW model responds to signals from undervoltage load shedding relay models differently. The undervoltage load shedding relays are devices modeled externally to CMPLDW.

The motor MVA base in CMPLDW is multiplied by the load[@i].shed signal – where @i is the GE

PSLF®internal load bus number – output by the undervoltage load shedding relay model to reduce the motor demand. Feeder reactance and shunt values are lowered proportionate to the load shed signal to mimic tripping an equivalent fraction of the feeder in addition to the load [4].

CMPLDWG

The WECC CMPLDW has an expansion which allows users to include modeling of distributed energy resources at the load bus withing CMPLDW. This update to the model is called CMPLDWG. The model as specified by WECC in [2] inverter-based photovoltaic distributed generation. However, in recent years, positive sequence transient simulation software packages have incorporated CMPLDWG to be used with the DER_A model [4]. More information about the DER_A model is provided in Chapter 3. Figure 2.4 depicts the CMPLDWG model with DER connected at the load bus.

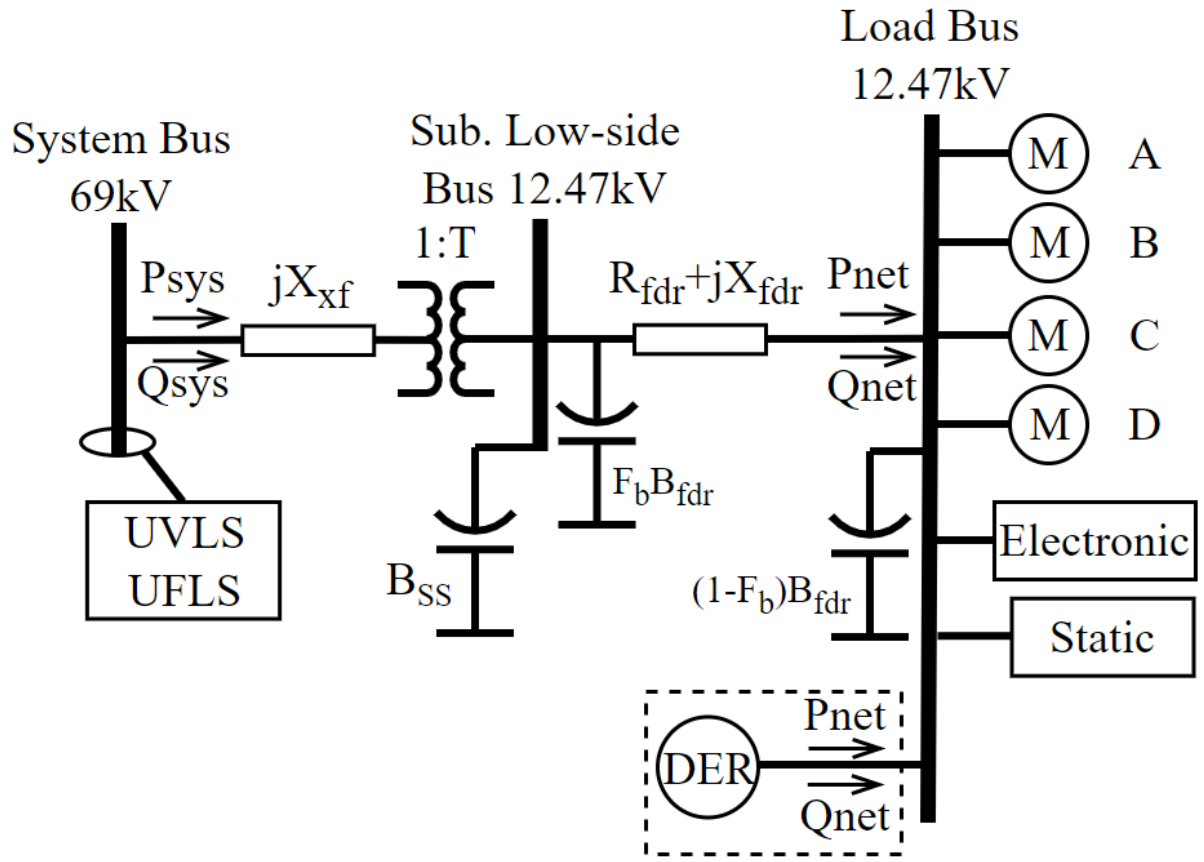

Figure 2.4: One-line diagram of the CMPLDWG model [2]

2.2 VFD Driven Air Conditioners and FIDVR

2.2.1 Background

Variable Frequency Drive (VFD) driven air conditioners are relatively new options available to homeowners. VFD driven air conditioners are power electronic interfaced, allowing air conditioner compressor motors to operate at a range of speeds. This This prevents cycling of air conditioner compressor motors to achieve desired temperatures. Operation of compressor motors at a range of speeds is estimated to be about 35% more efficient over the year [39]. EPRI identifies the Phoenix, AZ area as one more likely to have a higher penetration of VFD driven air conditioning units due to the large range of high temperatures over the summer window [13].

Presently, there are some limitations on the penetration of VFD driven air conditioners. The initial investment cost of VFD air conditioners is higher than that of one- or two-speed air conditioners. While the long-term savings of the VFD driven air conditioner will bring a return on investment, it may take years to do so. If a consumer is unable to afford the initial investment cost or is not planning to continue living in the home until the investment is returned in savings, a one- or two-speed air conditioner is more likely to be installed. There are few residential VFD driven packaged air conditioner units on the market. Packaged units are ones in which all components of the air conditioner are manufactured in one single metal package in a factory, and installed on the exterior of a house, typically on the roof [40]. Smaller homes, homes without basements, and homes with limited or no crawl space are most likely to have packaged air conditioning units. A split air conditioning system is one in which the compressor and condenser are in one metal unit installed on the exterior of a house, and the evaporator and air handling unit is in the interior of a house, often in a crawl space or basement. It is not economical or always feasible to replace a packaged unit with a split system unit. It is possible to retrofit packaged units with VFDs, however data on the practice is only available for commerical units [39].

EPRI has performed laboratory tests of various residential air conditioner types, including VFD driven air conditioners, aiming to improve Motor D parameter tuning [13]. While testing residential air conditioners, EPRI found that the VFD driven air conditioners disconnect when the voltage at the motor terminal drops to 0.75-0.70 pu, and do not reconnect for several minutes. This is a significant departure from the behavior of one- and two-speed air conditioners. Mini-split VFD air conditioners tested in [41] find similar results. These findings are incorporated into the modeling proposed in this chapter by changing the voltage trip and reconnection settings and eliminating stalling for VFD driven air conditioners.

EPRI has also presented an aggregate VFD model in [42] and [23] to represent an aggregation of three-phase industrial VFD loads. The model is not yet available in commercially available positive sequence dynamic simulation packages. The VFDs tested by EPRI to develop the aggregate model were three-phase and, in general, larger in horsepower rating than the single-phase air conditioner EPRI tested in [13].

The NERC-recommended Motor D parameters reflect the behavior of one- and two-speed air conditioners, not VFD driven air conditioners. NERC documentation and software manuals do not specifically address modeling VFD driven air conditioners, and utilities may not have end-

use information on VFD driven air conditioners in their service territory. Appropriately tuning CMPLDW parameters to model residential VFD driven air conditioners can lead to more realistic study results. Hence, in this chapter, the data provided in [13] based on testing VFD driven air conditioners is utilized to appropriately tune the CMPLDW model such that the VFD driven air conditioners trip when voltage lowers to 0.75-0.70 pu and do not reconnect. This is first accomplished by modeling VFD driven air conditioners as a separate load using the LD1PAC model in GE PSLF®, then by incorporating VFD driven air conditioners in CMPLDW using the power electronic representation. The power electronic representation is a constant active and reactive power load which linearly decreases between user-defined voltages V_{tr_1} to V_{tr_2}, at which point 100% of the power electronic load is disconnected. This chapter presents a methodology for representing VFD driven air conditioning as a power electronic load when all air conditioning has been hitherto considered one- and two- speed, as represented by Motor D.

Considering the present and future reasonable penetration of VFD driven air conditioners in residential applications a range of α_{VFD} from 0% to 90% is chosen for this study. Presently, the range of 15% to 30% of new air conditioners being VFD driven is assumed to be reasonable. The availability and affordability of VFD driven residential air conditioners and regulatory mandates to use VFD driven residential air conditioners may drive the penetration of new VFD driven air conditioners to be greater than 30%. The above practical concerns are taken into consideration when modeling future VFD penetration scenarios in this chapter.

The analysis presented in this chapter shows the benefits of VFD driven air conditioners on reducing FIDVR's impact on the system. The study results can provide directions for system upgrades and inform utility consumer rebates for variable speed air conditioners – i.e. where to invest utility capital.

2.2.2 VFD Driven Air Conditioner Modeling Methodology

The heavy summer load power flow and dynamic data for a real utility, and home age information for the homes in the utility's service area were used to study FIDVR events. Within a power system of 24114 buses and 4400 generators, the studied system is comprised of 746 buses and 124 generators. There are 316 load buses at 69kV modeled with CMPLDW. Discounting industrial facilities and power plant auxiliary loads, there are 264 load buses at 69kV modeled with CMPLDW. Load type and home age data was available for 254 of those 69kV load buses with CMPLDW models. The home age data includes the number of homes built each year for each 69kV feeder transformer from 1955 to 2019. .

The US Department of Energy estimates that the average life cycle of residential air conditioners is 15 to 20 years [43]. Due to the very high temperatures experienced in the summer in the utility's service territory, it is assumed that residential air conditioners in the area will have a higher duty cycle and therefore a shorter lifespan. A life span of 15 years is chosen in estimating the number of new air conditioners in the service territory. A "new" air conditioner is defined as one that is less than 5 years old. The percentage of new air conditioners for a given 69kV bus, ρ_i, is calculated as

$$\rho_i = \frac{N_{H_{new,i}}}{N_{H,i}} \tag{2.1}$$

$$N_{H,i} = \sum_{y=1955}^{2109} N_{H_{y,i}} \tag{2.2}$$

$$N_{H_{new,i}} = \sum_{y=1955}^{2019} N_{H_{y,i}} x_y \tag{2.3}$$

where

$$M_y \coloneqq (2019 - y) \mod A_{rep} \tag{2.4}$$

$$x_y \coloneqq \begin{cases} 1 & \text{if} \quad M_y \leq A_{new}, \\ 0 & \text{if} \quad M_y > A_{new}. \end{cases} \tag{2.5}$$

The percentage of new air conditioners which are VFD driven for a given 69kV bus, $\rho_{VFD,i}$, can be calculated as

$$\rho_{VFD,i} = \alpha_{VFD} \rho_i. \tag{2.6}$$

The chosen penetration of VFD driven air conditioners among new air conditioners, α_{VFD}, is system-wide, not bus specific. The range of α_{VFD} was determined based on information from the utility's air conditioner rebate program data and consultation with local air conditioner installers. In the absence of residence sizes, houses are assumed to have the same air conditioner load on average. In reality, larger houses are more likely to have VFD driven air conditioners installed compared to ones; feeders with larger houses would have a higher penetration of VFD driven air conditioners.

The percentage of new air conditioners which are VFD driven is calculated for each load bus modeled with CMPLDW for which home age information was provided, n, a total of 254 buses. However, it is helpful to know the total penetration of single-phase motors in the power system which are VFD driven, ρ'_{VFD}, which is calculated as

$$\rho'_{VFD} \coloneqq \frac{\sum_{i=1}^{n} \rho_{VFD,i} Fmd_i P_{load,i}}{\sum_{i=1}^{n} Fmd_i P_{load,i}}. \tag{2.7}$$

Using LD1PAC

Because the behavior of single-phase VFD driven air conditioners differs considerably from the one- or two-speed single-phase motors which are modeled by Motor D in CMPLDW, a separate and

distinct model was used to model the VFD driven air conditioners. Consequently, the protection parameters of the VFD driven air conditioners could be modeled exactly; the Motor D parameters would not be tuned to account for VFD driven air conditioners. For this purpose, the single-phase performance model LD1PAC is used to model the VFD driven air conditioners.

Each load is represented in the load table of the power flow data file. In the dynamic data, there is one CMPLDW model which corresponds to each load. The use of more than one load model per load is not allowed by PSLF. Therefore, for each of the 254 load buses considered in the case studies, a second load in the power flow is created representing only the VFD driven air conditioners. Then an LD1PAC model is created in the dynamic data model corresponding to the VFD load in the power flow.

The reallocation of load from one represented by the CMPLDW model to load represented by the LD1PAC model requires editing the fractional load parameters in the CMPLDW model, Fma, Fmb, Fmc, Fmd, and Fel. This ensures that the total load – in megawatts – modeled as each type of three-phase motor, power electronic load, or static load remains equal to the base case. At each 69kV load bus, with the bus index i omitted in (2.8)-(2.14), the load and CMPLDW parameter values for the VFD penetration sensitivity studies are calculated as

$$P_1 = P_{1_0} - \rho_{VFD} Fmd_0 P_{1_0} \tag{2.8}$$

$$P_2 = \rho_{VFD} Fmd_0 P_{1_0} \tag{2.9}$$

$$Fmd = \frac{P_{1_0} Fmd_0 - P_2}{P_1} \tag{2.10}$$

$$Fma = \frac{P_{1_0} Fma_0}{P_1} \tag{2.11}$$

$$Fmb = \frac{P_{1_0} Fmb_0}{P_1} \tag{2.12}$$

$$Fmc = \frac{P_{1_0} Fmc_0}{P_1} \tag{2.13}$$

$$Fel = \frac{P_{1_0} Fel_0}{P_1} \tag{2.14}$$

The load P_2 is modeled in the dynamic data as LD1PAC. The LD1PAC parameters Vc_{1off}, Vc_{2off}, Vc_{1on}, and Vc_{2on}, are set to represent all P2 as single-phase VFD driven air conditioners as described

by the findings in [13]. Table I presents the key parameters used in LD1PAC to ensure that P_2 acts as the VFD driven air conditioner described in [13].

Table 2.2: LD1PAC Parameters to Model VFD Driven Air Conditioners

Vc_{1off}	Vc_{2off}	Vc_{1on}	Vc_{2on}	V_{stall}	T_{stall}
0.75	0.70	2.0	2.0	0.0	9999

Using CMPLDW Only

Using the LD1PAC model to model VFD driven air conditioners is burdensome; it requires editing load in the power flow, creating a new load in the power flow, adding a model to the dynamic data, and editing many parameters in the existing models. It is preferable to use only the CMPLDW model which is already in use.

Several attempts are made to match the results of simulations using the LD1PAC model. The VFD driven air conditioners are modeled using this power electronic load by adjusting parameters Fmd and Fel at each load bus (with load bus index i omitted) as

$$Fmd = Fmd_0 - \rho_{VFD} Fmd_0 \tag{2.15}$$

$$Fel = Fel_0 + \rho_{VFD} Fel_0 \tag{2.16}$$

The simulations using the LD1PAC model assumes that 0% of the load disconnected due to low voltage reconnects when voltage recovers. With the CMPLDW parameters used by the studied utility, 100% of power electronic load disconnected by low voltage reconnects when voltage recovers. The fraction of power electronic load which can reconnect at each load bus (with load bus index i omitted), $Frcel$, is calculated as a function of VFD driven air conditioner load added to the power electronic load and is given as

$$Frcel = Frcel_0 - \frac{\rho_{VFD} Fmd_0}{Fel} \tag{2.17}$$

2.2.3 Case Studies

Work performed in [44] identified a critical faults for FIDVR in the power system. A three-phase fault is applied on a 230kV bus, Bus 100, and cleared after five cycles, 0.08s. The 69kV buses supplied by Bus 100 constitute Zone 100. The bus voltages in Zone 100 are monitored, and the 12.47kV load bus with the lowest post-fault voltage is selected for further examination. The bus identified as having the lowest post-fault voltage is named as Bus 112L and corresponds to the 12.47kV substation low-side Bus 112, and Bus 169 at 69kV, on which the CMPLDW model is represented. A simplified diagram showing the bus relationships is depicted in figure 2.5

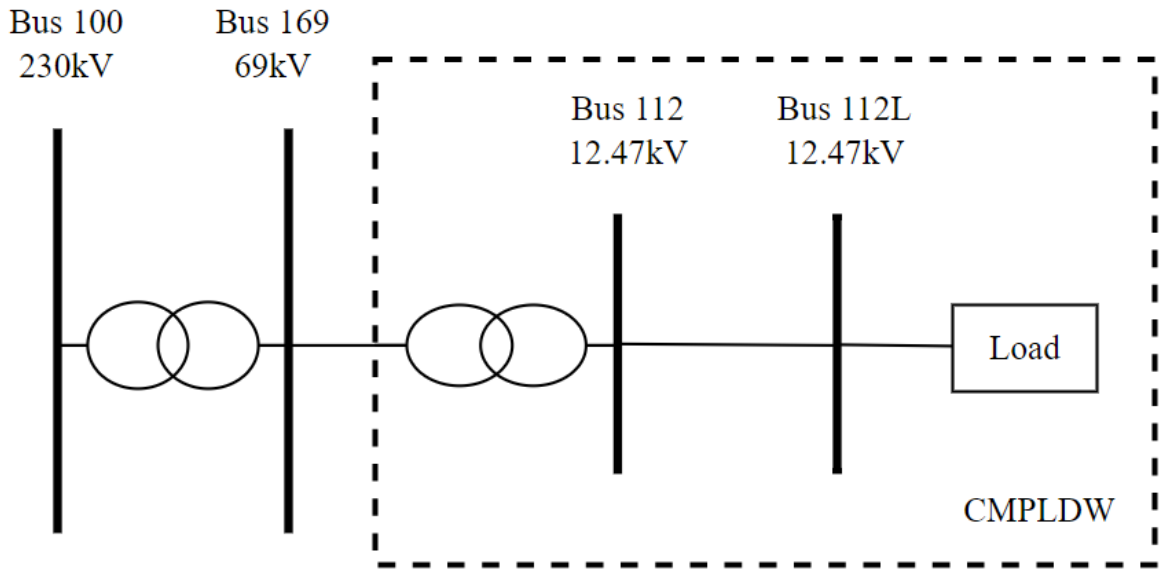

Figure 2.5: Simplified bus diagram. *Note*: This diagram does not depict the entire system. This diagram is to illustrate the relationship between buses described in this chapter. Information about the size of the full system is found in section 2.2.2

Base Case - 0% VFD Air Conditioning

During the fault, voltage magnitudes on buses near the fault location are low, as expected. However, the bus voltages do not recover to their pre-fault values for several seconds until enough stalled single-phase motor load is shed. It takes 17.94s for the voltage magnitude at Bus 112L to recover to its pre-fault value. The fault causes undervoltage load shedding (UVLS) relays across fifty-one 69kV buses to operate, shedding a total of 126.86MW. The UVLS relay on Bus 169 operates at t = 3.07s. Thermal protection devices on single-phase motors at Bus 112L begin opening at t = 8.05s. Figure 2.6 and Figure 2.7 show the nearby bus voltages following the fault on Bus 100.

Because motor speed is not calculated within the performance model, motor stalling is not an explicit output of the model. Therefore, a combination of Bus 169 active and reactive power outputs and Motor D trip-status may be used to assess stalling.

Outputs from the CMPLDW model are fractional values representing the fraction of Motor D motors tripped by the four available tripping mechanisms: undervoltage relay operation, contactor dropout, load shedding, and thermal protection operation. The output of fractional values is not a perfect representation of the model dynamics, as at any given time the total fraction of motors tripped can exceed one, indicating that more than 100% of motors have tripped, an impossibility. The best conclusion drawn from the tripping of thermal protective devices is that all Motor D motors at Bus 112L stalled and eventually tripped.

Bus 169 is operated at unity power factor. Therefore, before the fault, the reactive power is 0 Mvar. After the fault is cleared, the reactive power on the Bus 169 can be seen in Figure 2.8 to increase

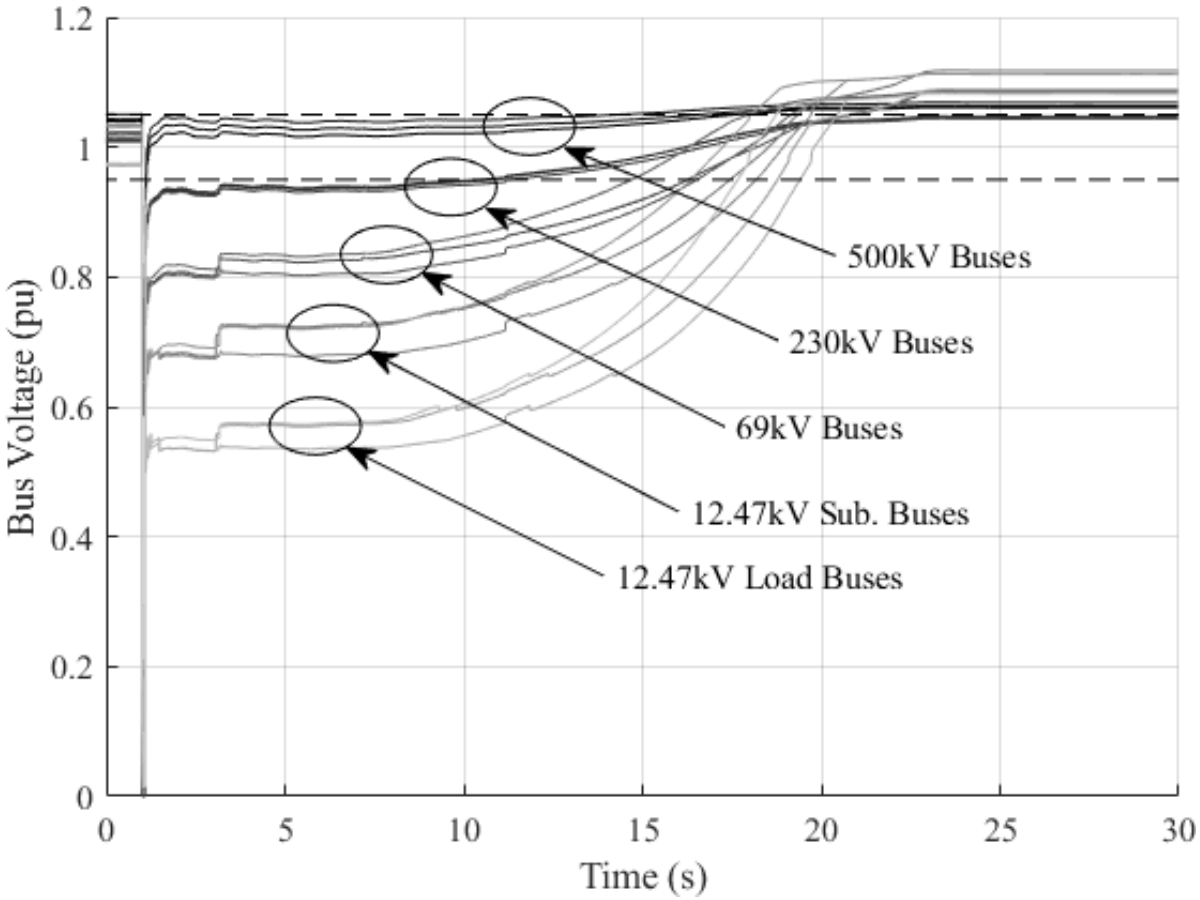

Figure 2.6: Nearby bus voltages following the fault on Bus 100.

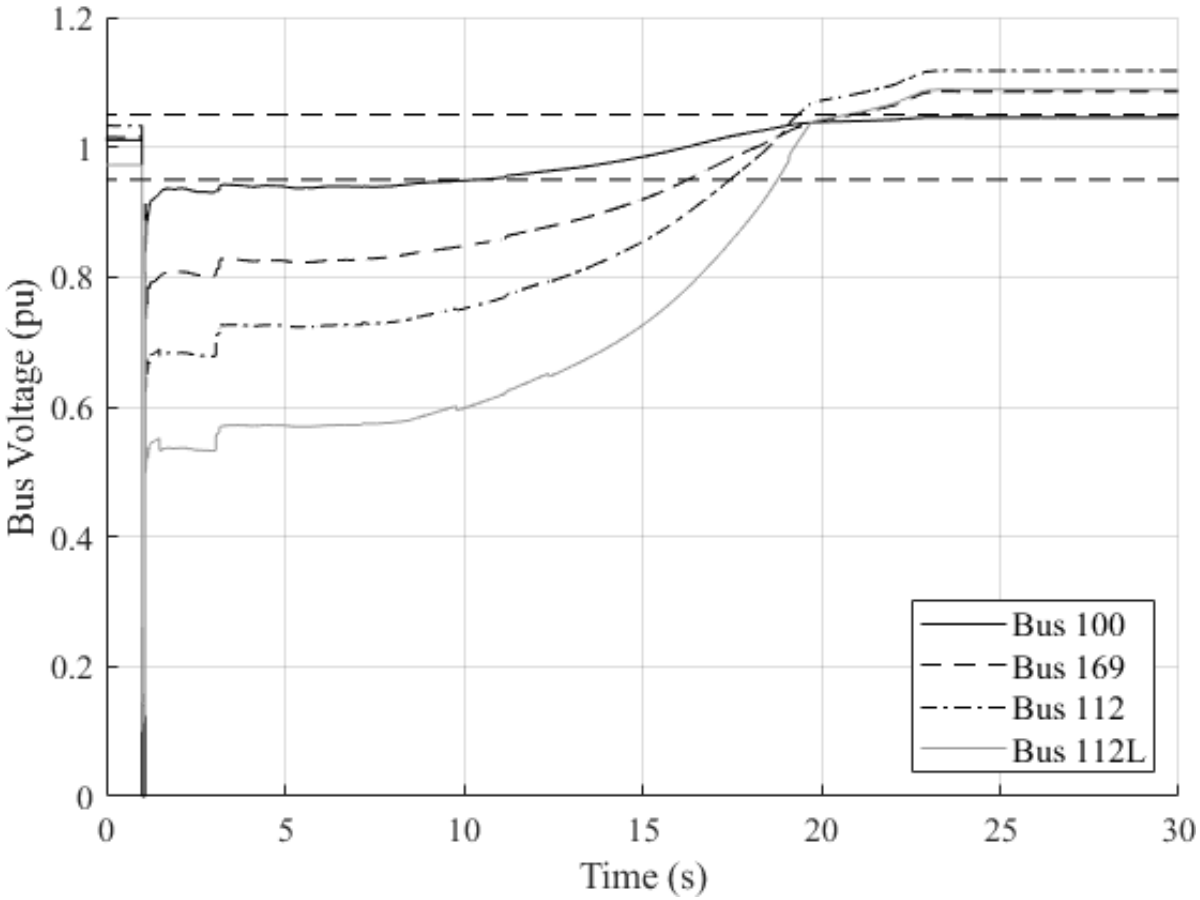

Figure 2.7: Bus voltages following the fault on 230kV Bus 100.

significantly and exceed the active power on the bus. This indicates stalled motors connected to the bus drawing high reactive currents.

As stalled single-phase motors are disconnected from Bus 112L by thermal protection operation, as shown in Figure 2.9 and Figure 2.10, the reactive power on Bus 169 decreased below its pre-fault value, and bus voltage increased beyond its pre-fault value. The voltage of Bus 169 reached steady state when all the stalled single-phase motors were tripped.

Two additional case studies were performed by applying two different three-phase faults on 230kV buses in two additional zones with different load compositions and Motor D penetration levels. The results of the two additional case studies reinforce the findings for the fault applied at Bus 100. The bus naming convention follows that of the case study presented.

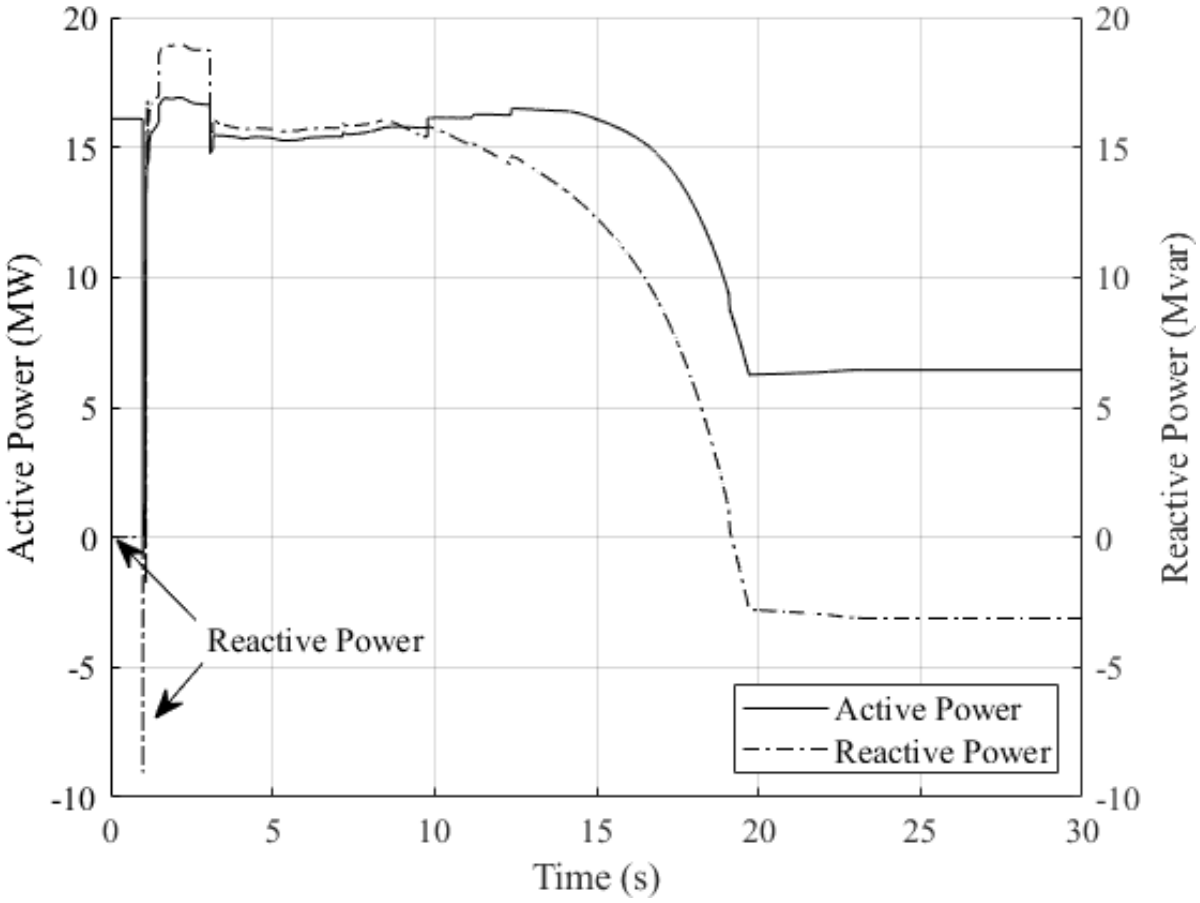

Figure 2.8: Bus 169 active and reactive power following the fault on Bus 100.

VFD Air Conditioner Modeling with LD1PAC

Following (2.1) – (2.14), various percentages – 5, 10, 15, 20, 25, 30, 50, 70, and 90% - of new air conditioner loads in the power system were modeled as VFD driven air conditioners using LD1PAC. The same three-phase fault was applied on bus 100 and cleared after 5 cycles.

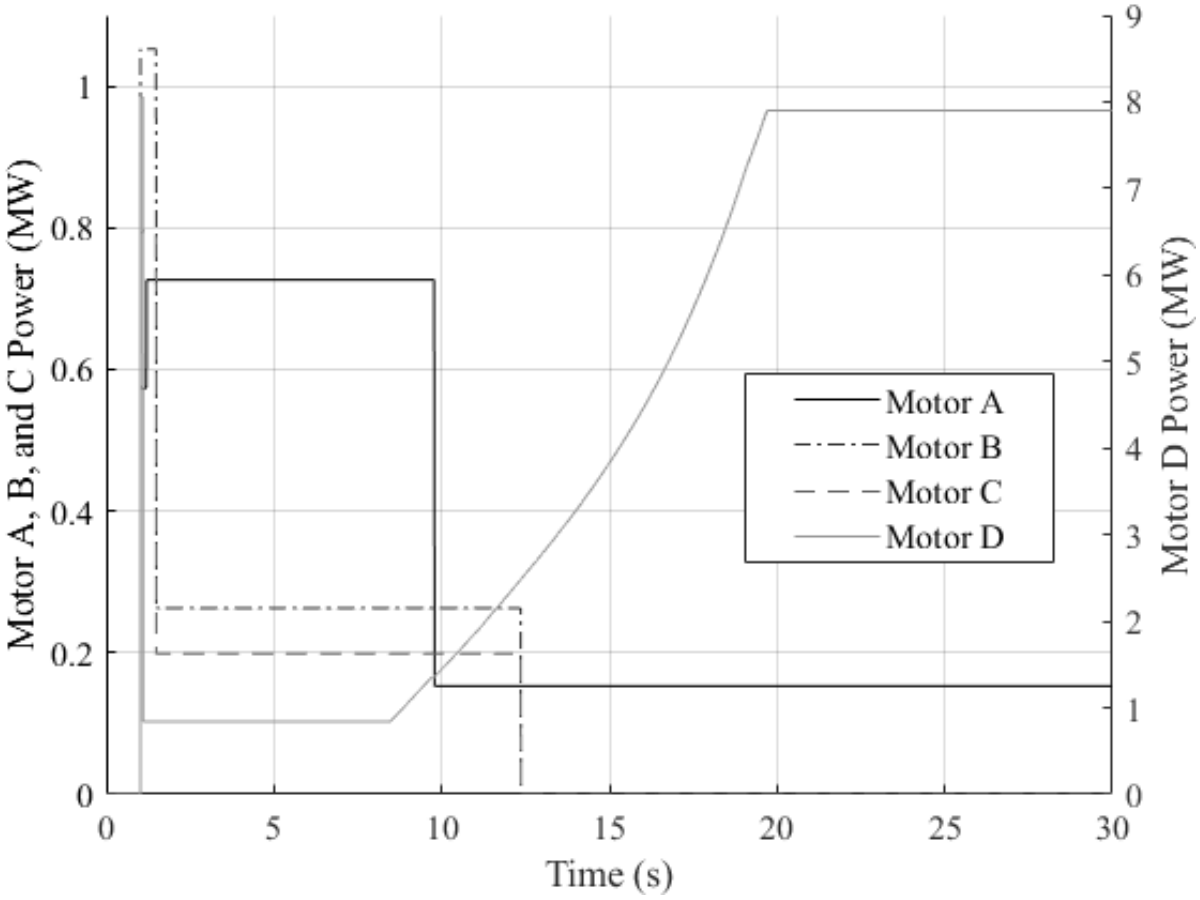

Figure 2.9: Single- and three-phase motors tripped offline from Bus 112L, measured in MW.

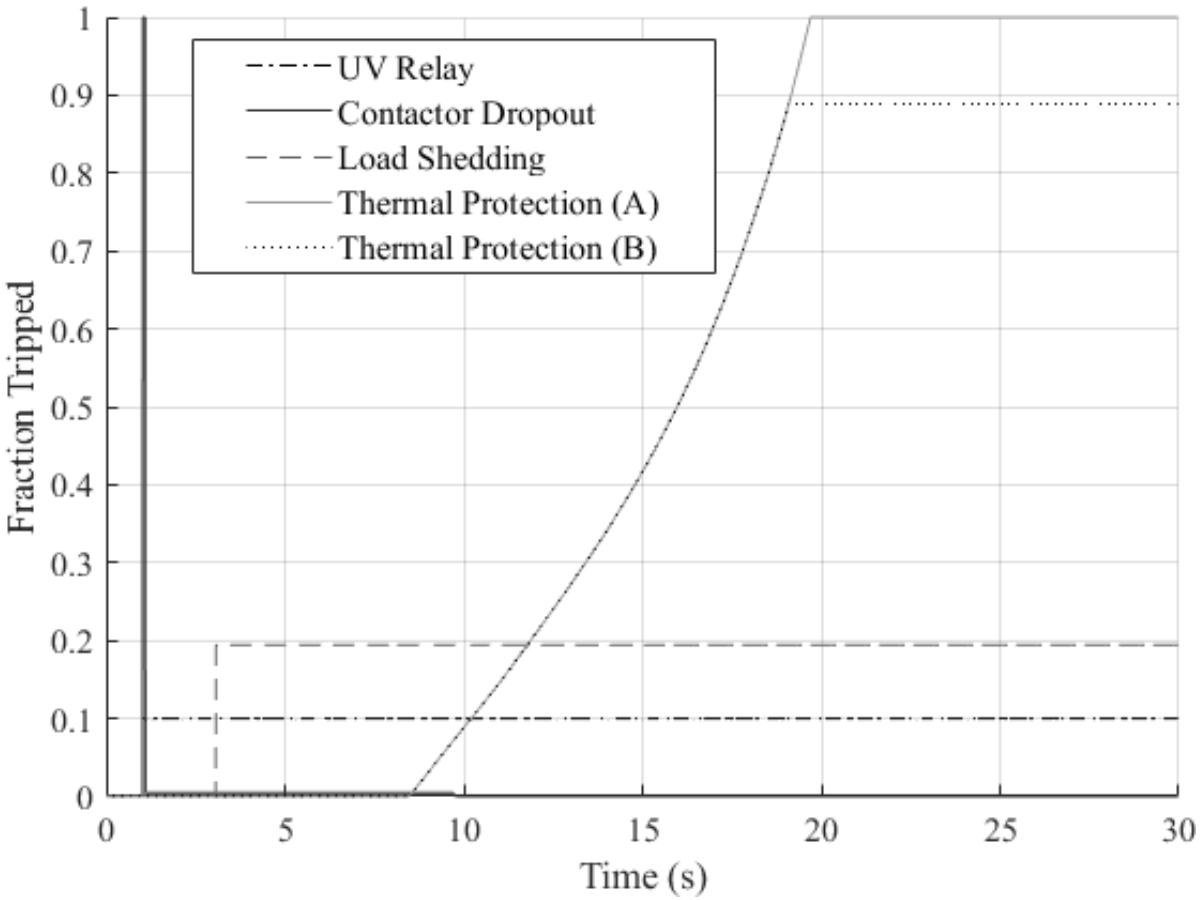

Figure 2.10: Fraction of Motor D tripped.

Table 2.3: Post-Fault Voltage Recovery Time and Total Load Shed

VFD (%)	Recovery Time (s)			Total Load Shed (MW)		
	112L	212L	312L	112L	212L	312L
0	17.94	20.36	19.53	126.86	183.32	27.37
5	17.13	19.86	19.21	126.86	183.32	35.51
10	16.74	19.53	19.01	126.86	183.32	34.15
15	16.49	19.17	18.17	125.85	183.32	16.52
20	16.28	18.80	18.30	125.85	183.32	14.00
25	16.10	18.40	18.03	123.30	183.32	14.00
30	15.80	18.01	17.67	120.89	183.32	4.84
50	14.72	16.76	16.86	102.40	176.09	0
70	13.65	15.51	15.53	76.99	170.60	0
90	12.92	13.90	15.01	50.08	154.08	0

Figure 2.11 shows that as VFD driven air conditioner penetration is increased, both the magnitude of the post-fault voltage drops, and the bus voltage recovery time is reduced. Because the post-fault voltage recovers sooner, there are fewer UVLS relay operations.

VFD air conditioners trip at much higher voltages due to VFD controller protection settings. The VFD air conditioners will not reconnect for several minutes while the VFD controller restarts. Shedding this load during and immediately after the fault results in post-fault bus voltage magnitudes being higher.

However, the one- and two-speed single-phase air conditioners, represented by Motor D in CMPLDW, still stall post-fault, and keep the post-fault bus voltage suppressed by drawing high reactive current. In the cases studied, all stalled Motor D motors tripped post-fault, as shown in Figure 2.12. Therefore, the severity of the FIDVR event was reduced, but not eliminated. Table II presents the bus voltage recovery time of the buses with the lowest post-fault voltages, and total load shed for the three faults studied as VFD air conditioner penetration is increased in the three different zones.

The improvement in post-fault bus voltage magnitude and recovery time is observed across bus voltages in the area surrounding the fault, as depicted in Figures 2.13, 2.14, and 2.15.

VFD Modeling with CMPLDW Only

As described above, it is preferable to use only the CMPLDW model to decrease the data preparations and modeling effort required for representing VFD driven air conditioners. The 30% penetration of VFD driven air conditioners among new air conditioners case was chosen to use only CMPLDW to model VFD driven air conditioners.

The steps described by (2.1) – (2.7) and (2.15) – (2.17) were used to migrate a portion of single-phase motor loads representing VFD driven air conditioners from Motor D to the power electronic

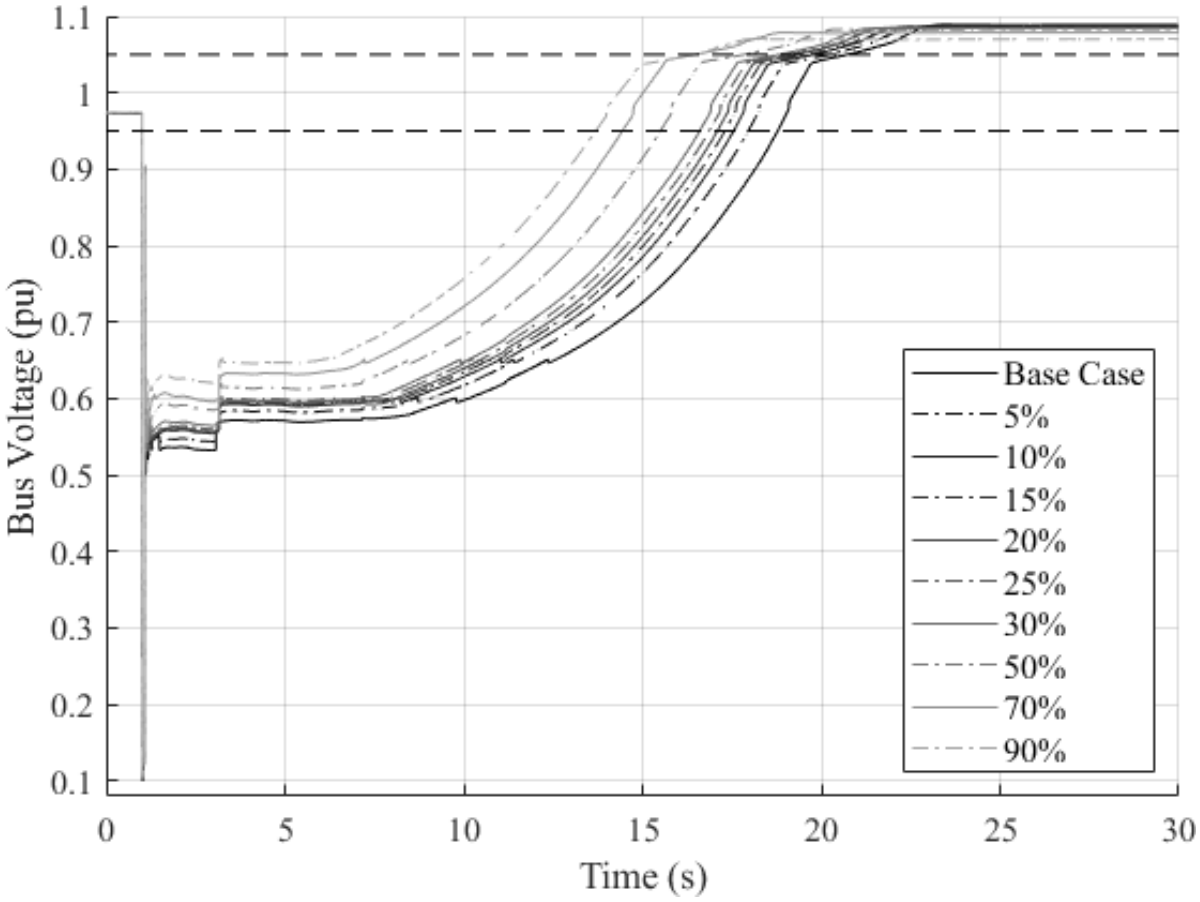

Figure 2.11: Bus 112L voltages under varying penetration of VFD driven air conditioners modeled with LD1PAC.

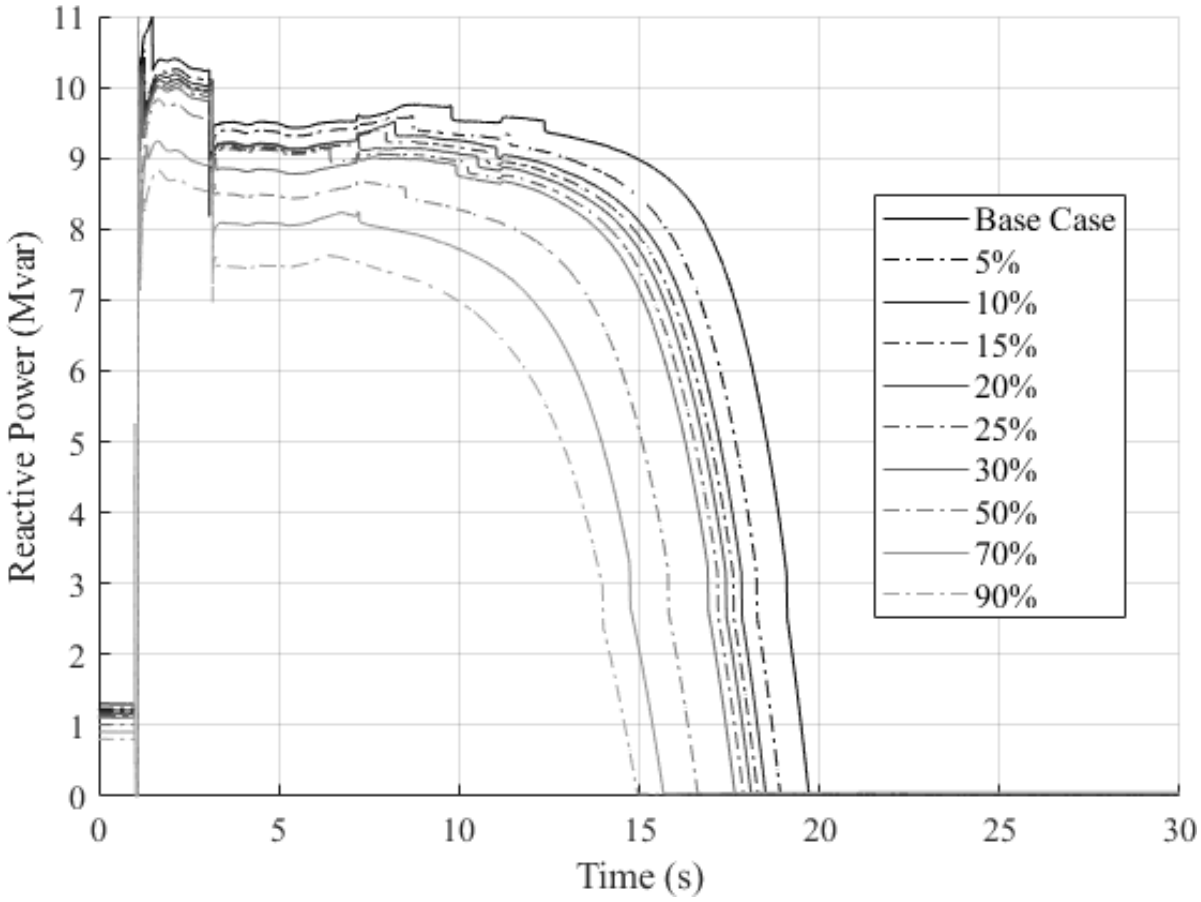

Figure 2.12: Bus 112L Motor D reactive power under varying penetration of VFD driven air conditioners modeled with LD1PAC.

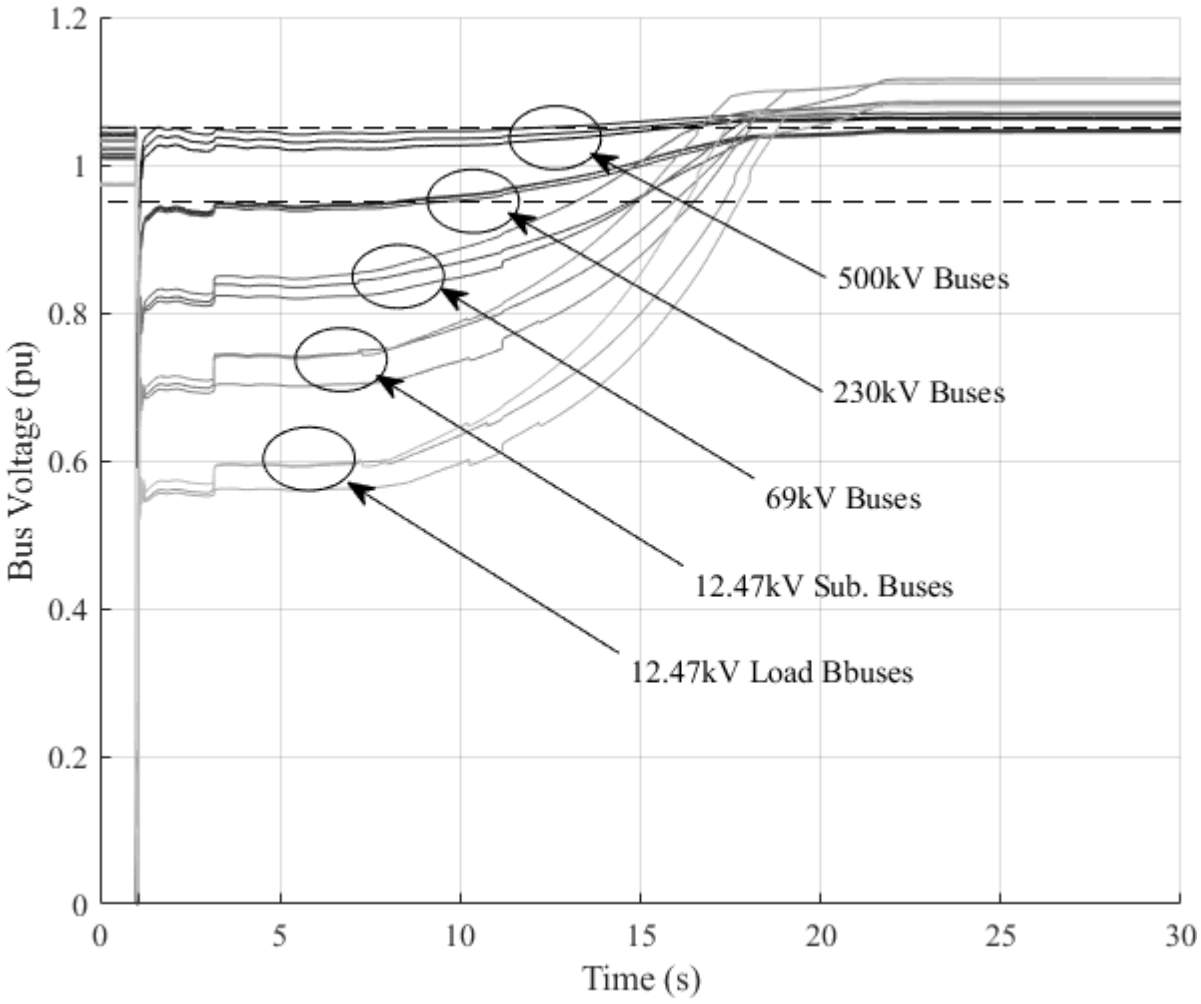

Figure 2.13: VFD Penetration at 15%: Bus voltages following the fault on Bus 100.

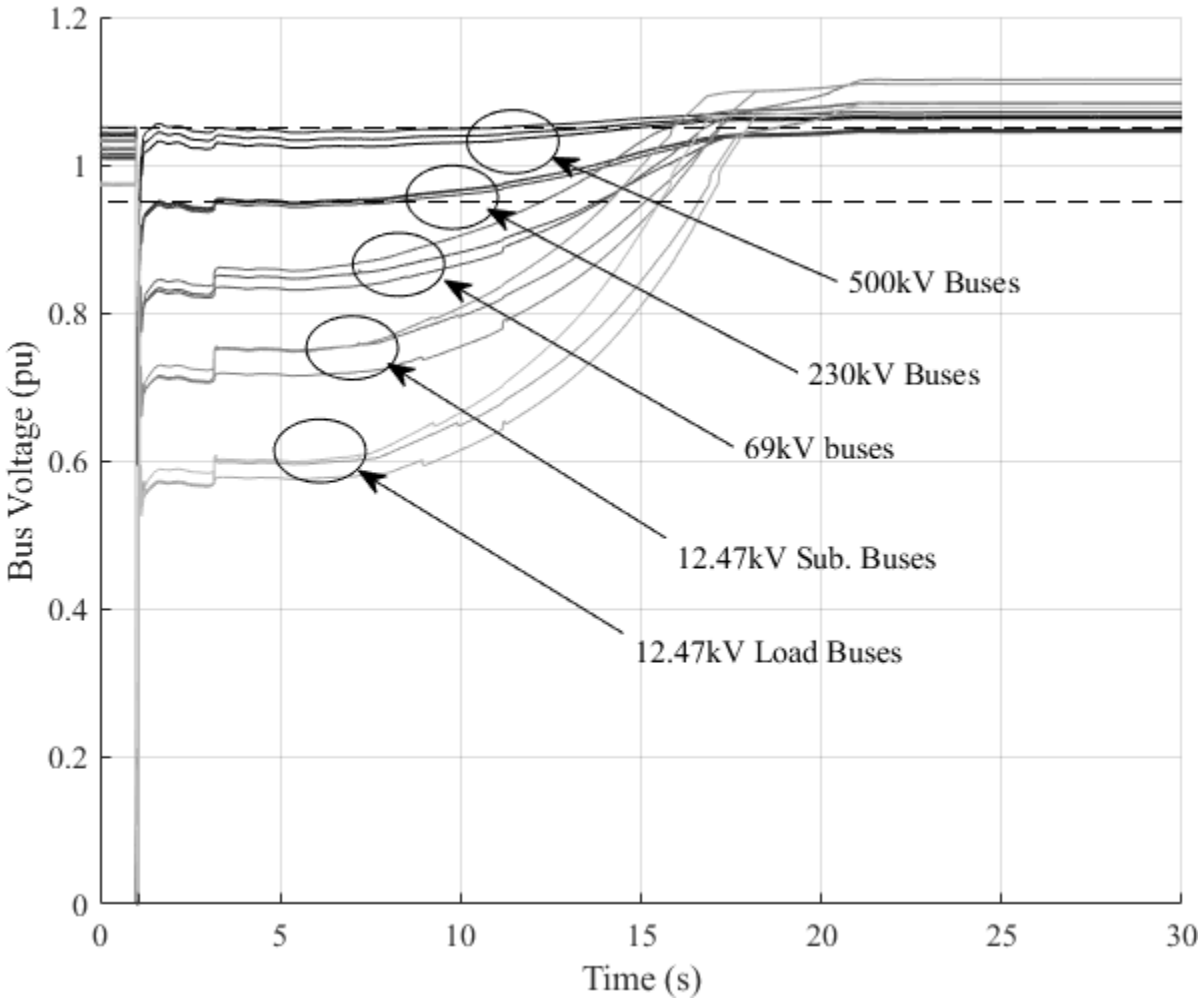

Figure 2.14: VFD Penetration at 30%: Bus voltages following the fault on Bus 100.

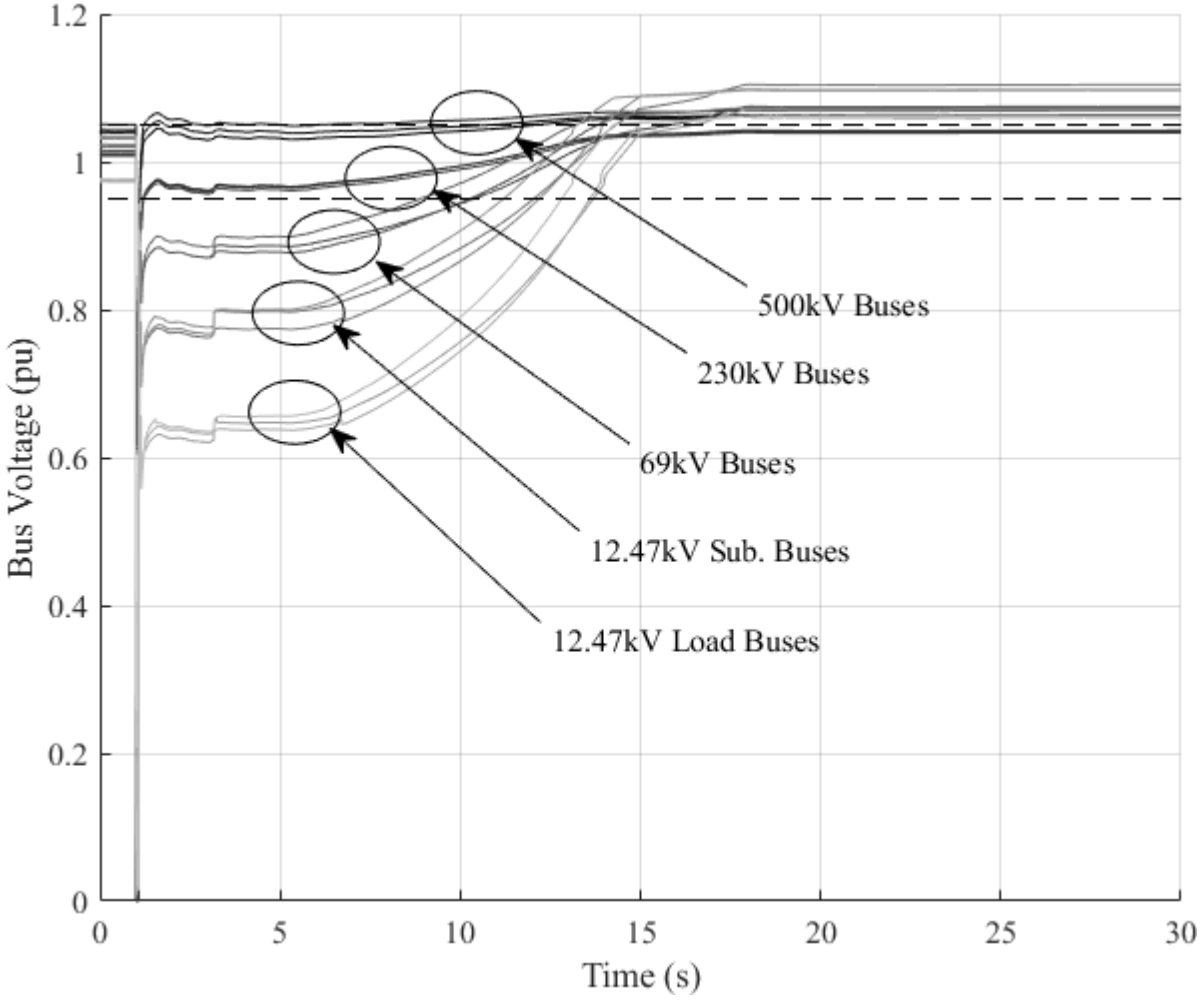

Figure 2.15: VFD Penetration at 90%: Bus voltages following the fault on Bus 100.

load. First, only the Fel power electronic load parameter was changed, using (2.15) and (2.16). Results are shown in Figures 2.16. Then the $Frcel$ parameter was changed to be a function of VFD driven air conditioner load added to the power electronic portion of CMPLDW, using (2.17). Results of this effort are depicted in Figures 2.17.

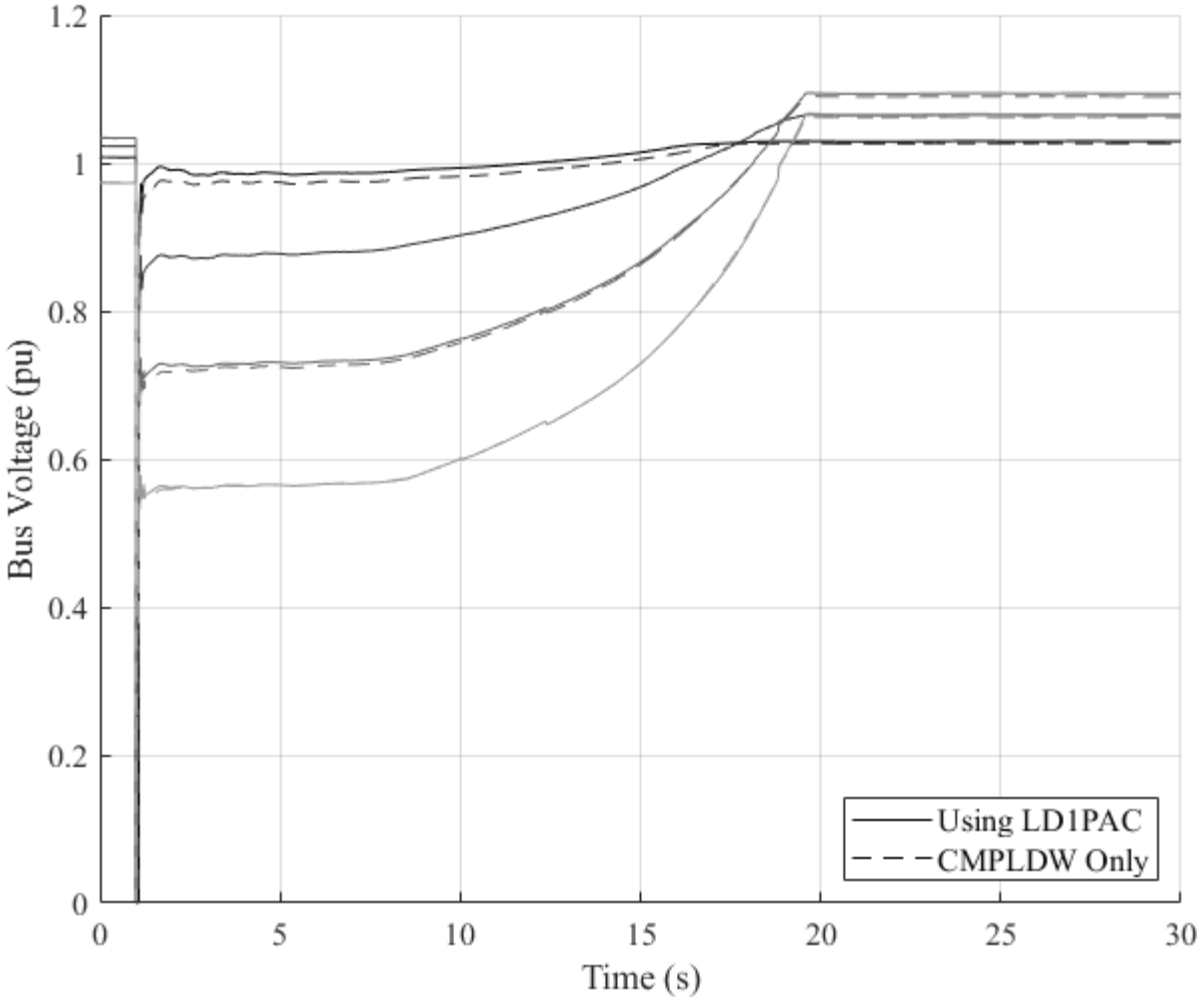

Figure 2.16: VFD Penetration at 30%: Bus voltages following the fault on Bus 100 modeled with LD1PAC and CMPLDW only changing the Fel parameter.

It is apparent that editing the $Frcel$ parameter to be a function of VFD driven air conditioner load added to the power electronic load does not yield more desirable results but increases modeling burden for the power system planner. It is shown in Figure 2.18 that even when tested on the simulations with 90% VFD driven air conditioner penetration among new air conditioners, changing only the Fel parameter results in satisfactory results; the general shape of the voltage recovery curve is preserved, as is the voltage recovery time. This cannot be said for the simulations where $Frcel$ is changed per (2.17). Figure 2.19 shows a far more optimistic voltage recovery time.

Therefore, only changing the Fel and Fmd parameters within CMPLDW is necessary for capturing the effect of modeling a portion of single-phase air conditioners as VFD driven for planning studies.

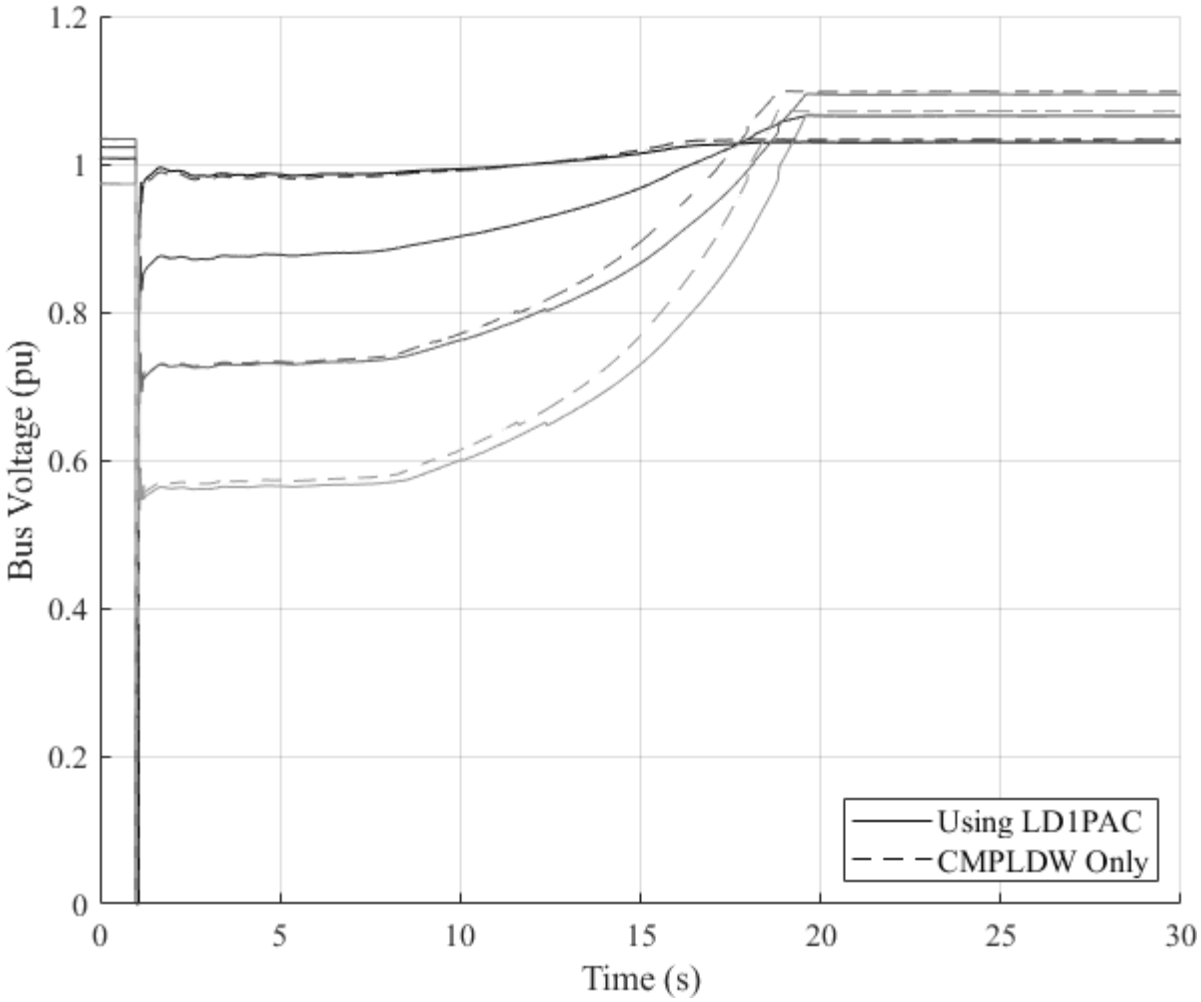

Figure 2.17: VFD Penetration at 30%: Bus voltages following the fault on Bus 100 modeled with LD1PAC and CMPLDW changing the Fel and $Frcel$ parameters.

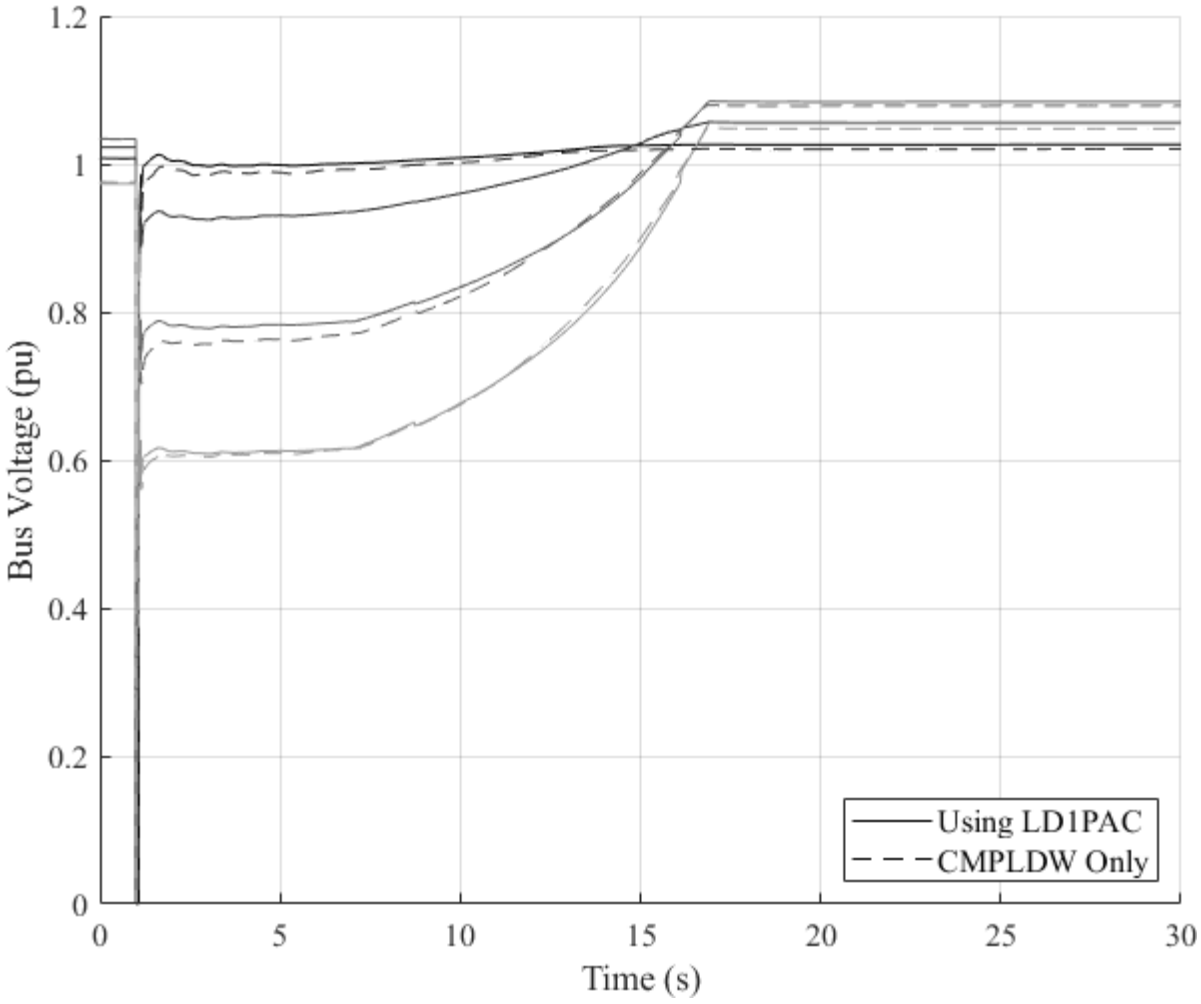

Figure 2.18: VFD Penetration at 90%: Bus voltages following the fault on Bus 100 modeled with LD1PAC and CMPLDW only changing the Fel parameter.

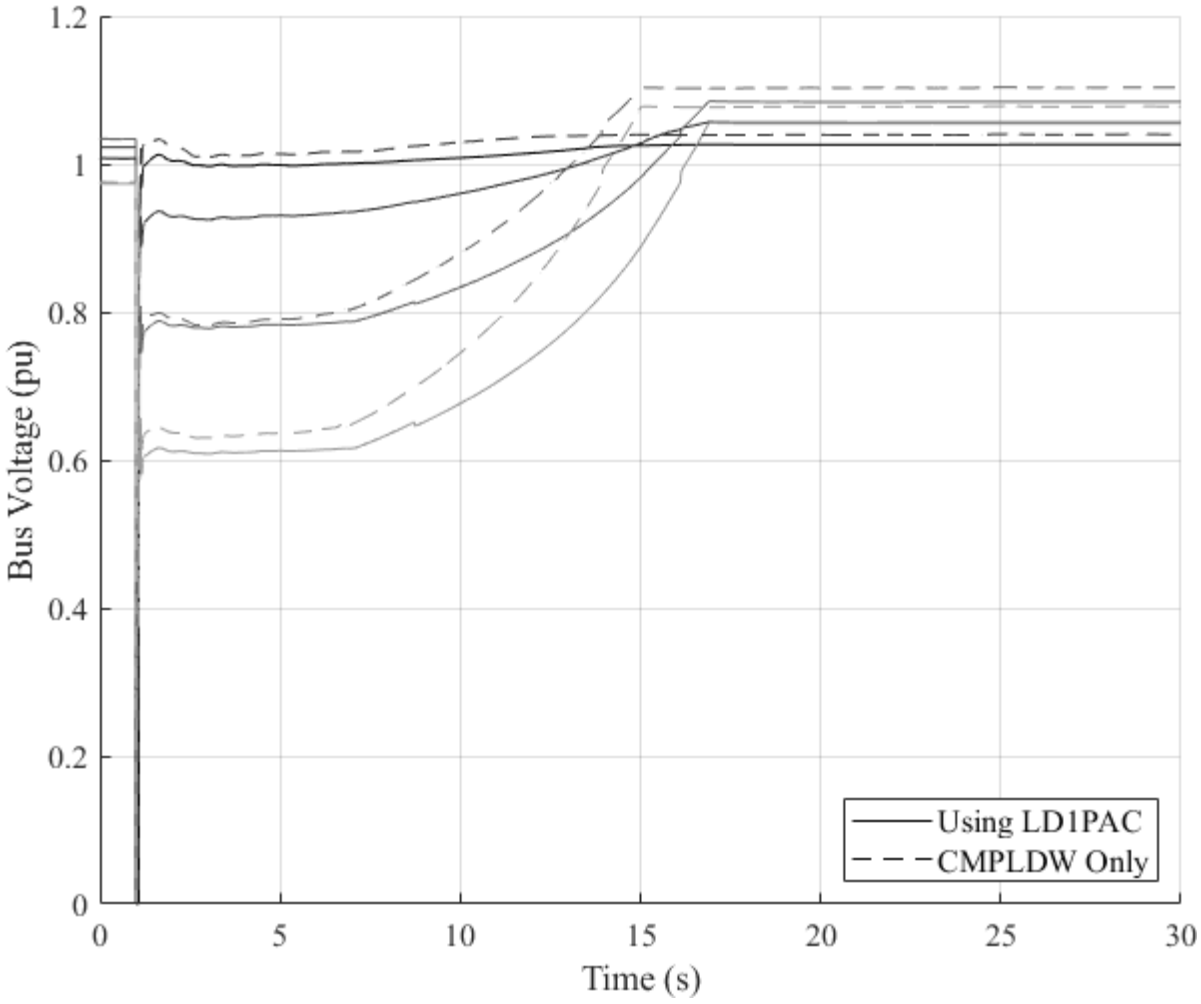

Figure 2.19: VFD Penetration at 90%: Bus voltages following the fault on Bus 100 modeled with LD1PAC and CMPLDW changing the Fel and $Frcel$ parameters.

2.2.4 Conclusions

This chapter presents a simple method for modeling VFD driven air conditioners as the power electronic load within the CMPLDW model and shows that increasing the penetration of VFD driven air condition load leads to reduced severity of FIDVR events. The simulations of three case studies showed that as the percentage of new air conditioners which are VFD driven increases, the voltage sag following the fault is less severe, and the time for the voltage to recover to the pre-fault value is shortened. There are also fewer operations of UVLS relays as the penetration of VFD driven air conditioners increases, resulting in fewer customers being adversely impacted by the fault. The increase in VFD driven air conditioners improves post-fault conditions but does not eliminate the FIDVR events from occurring.

The utility whose system was studied in this chapter had available information on the age of the homes on their 69kV sub-transmission feeders, and air conditioning rebate information. However, VFD driven air conditioner penetration sensitivity studies can be performed using other information which is available to the utility to establish ρ_{VFD} or ρ'_{VFD}.

Information about FIDVR events when VFD air conditioners are modeled can enhance power system planning and facilitate the design of corrective actions for FIDVR events or provide insight to customer programs for offering rebates to customers installing VFD driven air conditioners.

3. FIDVR Mitigation using DERs

3.1 Introduction

Power systems are experiencing an increase in penetration of inverter-interfaced distributed energy resources (DERs) – primarily rooftop photovoltaic solar – at the distribution level. The added DER results in changes to power system dynamics which require careful study. Interconnection agreements between utilities and interconnectors establish the steady state and dynamic requirements of the interconnected DERs. Adoption of new standards in interconnection agreements impact reliability of the power system.

The publication of IEEE Std 1547-2018 [3] is a reflection of the industry consensus that protection setpoints of DERs need to be better defined. Standards provide a basis for utilities to develop interconnection agreements and guidelines for the growing number of interconnectors at the distribution level, a large number of whom are homeowners investing in rooftop solar. Solar generation accounts for the largest share of new generation installed in 2021, continuing a trend from 2021 and 2020 [45]. NREL research found that about 65% of rooftop solar eligibility is from small roofs such as residences [46]. Due to the small generation capacity of residential rooftop solar installations, interconnection agreements and guidelines have been straightforward with simple protection and control requirements for residential rooftop solar installations [47]. The requirements for interconnection for rooftop solar is becoming more strict, but rely on the protection requirements described within Standards [48].

There is active research into the use of DER and novel control schemes for dynamic var support and mitigation of FIDVR. The authors of [49] leverage a 75MW photovoltaic solar generation farm as a var support with a novel control scheme, which they call PV-STATCOM, for FIDVR mitigation. The authors find that their PV-STATCOM performs better than traditional STATCOM devices, and costs less than STATCOM integration. A signal-temporal-logic embedded model predictive control strategy to control multiple battery energy storage systems' reactive power output is presented in [50]. This control scheme is centralized to the power system requiring global access to system parameters and communication ability with all end-devices, which the authors note may be overcome with a "local" model predictive control approach for distribution systems. A control scheme which coordinates switchable capacitors with DERs with smart inverters is proposed in [51] which acts to mitigate FIDVR and prevent the overvoltage typical in FIDVR events.

This chapter aims to study the impact of residential rooftop solar with protection settings defined in different versions of the IEEE Std 1547 on FIDVR. The DER of a real power system in the desert southwest was incorporated into their dynamic data using the DER_A representation within the WECC Composite Load Model (CMPLDWG) in GE PSLF®software. Different DER protection settings were modeled under various DER penetration levels. Faults on two 230kV transmission lines are studied and the voltage response under different representations and penetrations of DER is examined.

3.2 The DER_A Model

DER_A was developed to address the need to capture the effects of the growing number of DERs in power systems on power system reliability [52]. Earlier models used to represent renewable energy resources such as, the REGC_A, REEC_A, and REPC_A models have a high number of parameters and states and are better used for modeling individual, utility-scale energy resources, often referred to as U-DER[1]. The basis of the DER_A model is synthesizing the standalone renewable energy models into one model to represent aggregated, retail-scale DER (R-DER) with fewer parameters [52]. More detailed definitions for U-DER and R-DER are given in [53]. Due to the reduction in model complexity, the DER_A model is not able to fully represent the full range of DER dynamics, so parameterization must be carefully considered to account for what kind of study is being done [53]. The authors of [54] present a mathematical model of DER_A developed in MATLAB.

When using DER_A, the R-DER power output is represented within the power flow load table, and not as standalone generation. Then one DER_A management model needs to be used for the entire dynamic data file. The numerical identifier of the DER_A management model is a parameter within CMPLDWG which then establishes the R-DER behavior within the composite load model. Ideally, one DER_A management model is used for the entire utility area, but more than one can be used if there are a handful of buses with known deviations from the rest of the electric power system. An example of this would be a new bus which feeds a development built after the adoption of a new interconnection guideline where all of the DER is required to use smart inverters, and the rest of the buses in the electric power system have a mixture of DER with smart and legacy inverters.

NERC has published a reliability guideline detailing the features of the DER_A model and gives a parameterization of the model depending on which protection standard the DER is following [55].

3.2.1 Voltage Partial Tripping

Of high importance to the DER_A block is the partial voltage tripping block, particularly for voltage stability studies. DER's response to abnormal system voltage and frequency has been an early and increasing concern for power system operators who are responsible for ensuring system reliability. As the penetration of DERs increases in power systems, the ability of DERs to trip during, ride through, or to provide voltage support during abnormal system voltage events has become more important to system reliability.

The voltage partial tripping block within DER_A is important for modeling the voltage response to abnormal system voltage and requires careful understanding for performing FIDVR-related planning studies. There are ten DER_A parameters associated with the partial tripping block: tv, vl0, vl1, vh0, vh1, tvl0, tvl1, tvh0, tvh1, and vrfrac. When the voltage seen at the DER falls below vl1, a fraction of DERs de-energize. DERs will de-energize linearly as the voltage is lowered between vl1

[1]U-DER, and DER in general, is not technology specific; DERs can be, for example, synchronous machines which are connected at distribution buses can be considered DER, and should be modeled appropriately either with DER_A or synchronous machine models. Guidance is given in [3].

and vl0, at which point all DERs will be de-energized. When the voltage is less than vl1, a timer is initiated. The same is true when the voltage is less than vl0. If the voltage remains lower than vl1 for tvl1 seconds, or vl0 for tvl0 seconds, the DERs begin to trip offline. When the voltage recovers above vl0, the fraction of DERs that reconnect after tripping is determined by vrfrac (the red line in Figure 3.1). If the voltage is less than vl1 or vl0 for less than tvl1 or tvl0 seconds, respectively, 100% of DERs will re-energize when voltage recovers. The same process applies for over voltages.

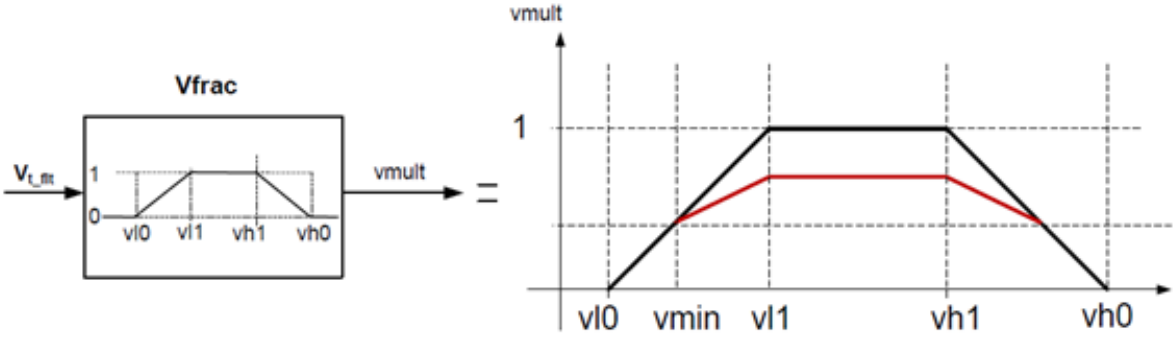

Figure 3.1: The DER_A model voltage partial tripping block diagram.

The difference between vl1 and vl0 and between vh1 and vh0 is designed to be the voltage drop across the feeder. To model the low voltage protection settings, lv0 is set equal to the per-unit voltage at which all DER is expected to be de-energized, and vl1 is set equal to the vl0 plus the voltage drop across the feeder. To model the high voltage protection setting vh0 is set equal to the per-unit voltage at which all DER is expected to be de-energized, and vh1 is set equal to vh0 minus the voltage drop across the feeder. This captures the effect of DERs de-energizing at the end of the feeder first, where the voltage is lower than toward the head of the feeder. This means that the DER_A model does not model multiple low and high voltage trip settings, even though the inverters are likely to have multiple protection requirements, many akin to inverse time undervoltage protection. More information about the technical requirements for DERs to respond to abnormal system voltage is given in section 3.3. EPRI suggests a voltage drop across the feeder of about 2-5% is reasonable [2]. For the case studies presented in section 3.4, a voltage drop across the distribution feeders of 4% was assumed.

3.3 IEEE Std 1547

3.3.1 Overview

Like the introduction of the DER_A model for stability studies, the IEEE Std 1547-2003 was created to address the changing impact of DERs interconnection experienced by electric utilities as more generation sources were connected at the distribution level [56]. Since the original publication, the standard was updated to incorporate experience gained by the industry and changing technologies [57]. The IEEE Std 1547a-2014 amendment was created, ". . . in response to a widely expressed need to make changes to IEEE Std 1547-2003 existing sections 4.1.1 Voltage Regulation, 4.2.3 Voltage, and 4.2.4 Frequency" [58]. The changes to the voltage requirements enabled DERs

to regulate voltage, require field adjustable under- and over-voltage protection settings, and to add more specificity in the voltage clearing times. California Rule 21 preceded the IEEE Std 1547-2018 revision and had led the industry in setting technical requirements for distribution level interconnectors, particularly those who wished to export energy into the power system [59]. California Rule 21 also required the use of "smart inverters" for large investor-owned utilities.

IEEE Std 1547-2018 is a technology agnostic standard which establishes interconnection technical and testing requirements for DERs connected at the distribution level [3] [57]. The standard notes that it is applicable to most DER applications. Special interconnection requirements may be required for large interconnections, which is another indicator that the standard is an evolving document and utilities may face additional challenges as DER penetration increases [3]. IEEE Std 1547-2018 incorporates requirements that necessitate the use of "smart inverters" for inverter interfaced DERs. Smart inverters enable DERs to provide voltage and frequency regulation and ride-through, where legacy inverters (those capable of meeting IEEE Std 1547-2003 standards) did not.

Given the motivation of this work, only the voltage setpoints for response to abnormal conditions required by the IEEE Std 1547 revisions will be explored in sections below.

3.3.2 IEEE Std 1547-2003 Revision

The IEEE Std 1547-2003 revision required DERs to cease to energize (no energy exchange between the DER and the electric power system) when system voltages fell below 0.88 pu voltage. The DER was allowed up to two seconds to cease energization, with less time to disconnect the lower the system voltage was. Testing standards for inverters ensured that inverters tripped when system voltage fell to 0.88 pu voltage [60].

3.3.3 IEEE Std 1547a-2014 Amendment

The IEEE Std 1547a-2014 amendment expanded the abnormal voltage requirements, giving latitude to electric power system operators to agree to longer clearing times [58]. This does not mean that there was a low voltage ride-through requirement as the clearing time was a maximum time to trip and no minimum ride-through time was established. Furthermore, this amendment got rid of the prohibition of DER to regulate system voltage, but it did not provide any more technical information about DERs providing voltage support.

Reference [58] required that DERs follow the latest version of IEEE Std 1547 for undervoltage protection. It is likely that the majority of DERs connected in present day power systems follow the IEEE Std 1547a-2014 amendment. However, with no other information provided in [58] or by the utility whose system is studied in section 3.4 about the exact clearing times settings, a maximum clearing time of two seconds was assumed. Therefore, the IEEE Std 1547-2003 and IEEE Std 1547a-2014 undervoltage protection settings are the same in this study.

3.3.4 IEEE Std 1547-2018 Revision

IEEE Std 1547-2018 introduced a number of significant revisions to requirements for DERs during normal operations and in response to abnormal system conditions. Abnormal voltage and frequency ride-through requirements were added to this standard, and more detailed guidelines established for voltage support by DERs [3]. For example, Section 5.3.3 of [3] covers volt-var mode for normal operation of DERs.

Several new definitions were also added to the standard to establish voltage ride-through operation. The definitions are important to consider when deciding how to model DERs in power system studies. As mentioned earlier, the DER_A model is not sophisticated enough to model every possible capability of the interconnected DER. The definitions for continued operation, mandatory operation, permissive operation, momentary cessation, ride-through, and restore output given in [3] were used to determine the vl0, vl1, vh0, vh1, tvl0, tvl1, tvh0, and tvh1 DER_A parameters for the case studies presented in section 3.4. The definitions are provided in Table 3.1 for the reader's conveniences.

Table 3.1: Phrases defined by IEEE Std 1547-2018 used to determine DER_A model

Phrase	IEEE Std 1547-2018 Definition [3]
Continued Operation	Exchange of current between the DER and an EPS within prescribed behavior while connected to the Area EPS and while the applicable voltage and the system frequency is within specified parameters.
Mandatory Operation	Required continuance of active current and reactive current exchange of DER with Area EPS as prescribed, notwithstanding disturbances of the Area EPS voltage or frequency having magnitude and duration severity within defined limits.
Permissive Operation	Operating mode where the DER performs ride-through either in mandatory operation or in momentary cessation, in response to a disturbance of the applicable voltages or the system frequency.
Momentary Cessation	Temporarily cease to energize an EPS, while connected to the Area EPS, in response to a disturbance of the applicable voltages or the system frequency, with the capability of immediate Restore Output of operation when the applicable voltages and the system frequency return to within defined ranges.
Ride-through	Ability to withstand voltage or frequency disturbances inside defined limits and to continue operating as specified.
Restore Output	Return operation of the DER to the state prior to the abnormal excursion of voltage or frequency that resulted in a ride-through operation of the DER.

Figures 3.2, 3.3, and 3.4 depict the IEEE Std 1547-2018 abnormal operation performance criteria for Catergories I, II, and III, respectively. The DER_A model's partial tripping block for voltage does not include a time delay for DER cessation. The time delays tvl0, tvl1, tvh0, and tvh1 are for tripping the DERs only, meaning that the DERs do not restore output following voltage recovery. Because of this design of the partial tripping block, the beginning of the momentary cessation region for each standard/category of DER response to abnormal system is chosen as the vl0, vl1, vh0, and vh1 parameters in the DER_A model.

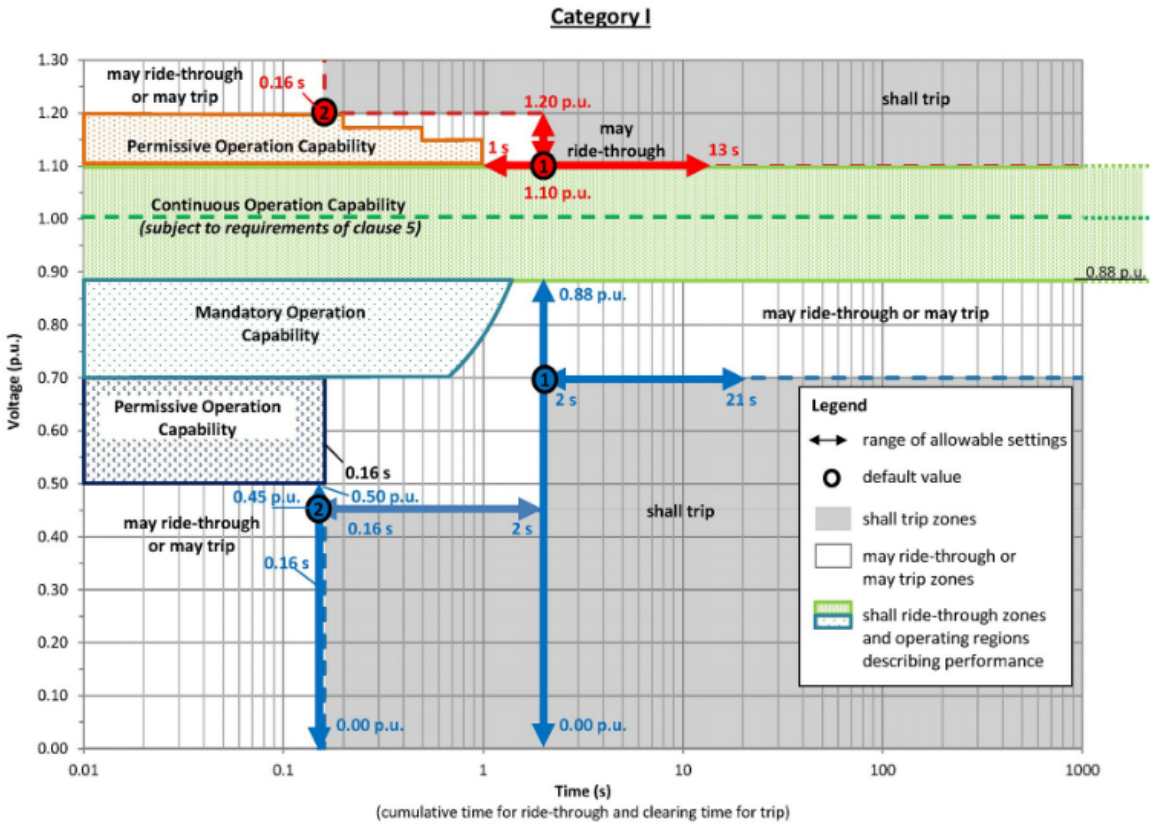

Figure 3.2: DER response for abnormal operating conditions Category I DERs [3].

3.3.5 Testing Standards

IEEE Std 1547-2018 requires DERs be tested in compliance with IEEE Std 1547.1-2020 [3] [61]. Before the publication of IEEE Std 1547.1-2020, California Rule 21 required compliance with UL 1741 Supplement A, which included testing requirements for smart inverters. Since the publication of IEEE Std 1547.1-2020, UL 1741 Supplement B has incorporated updates to reference IEEE Std 1547.1 [60].

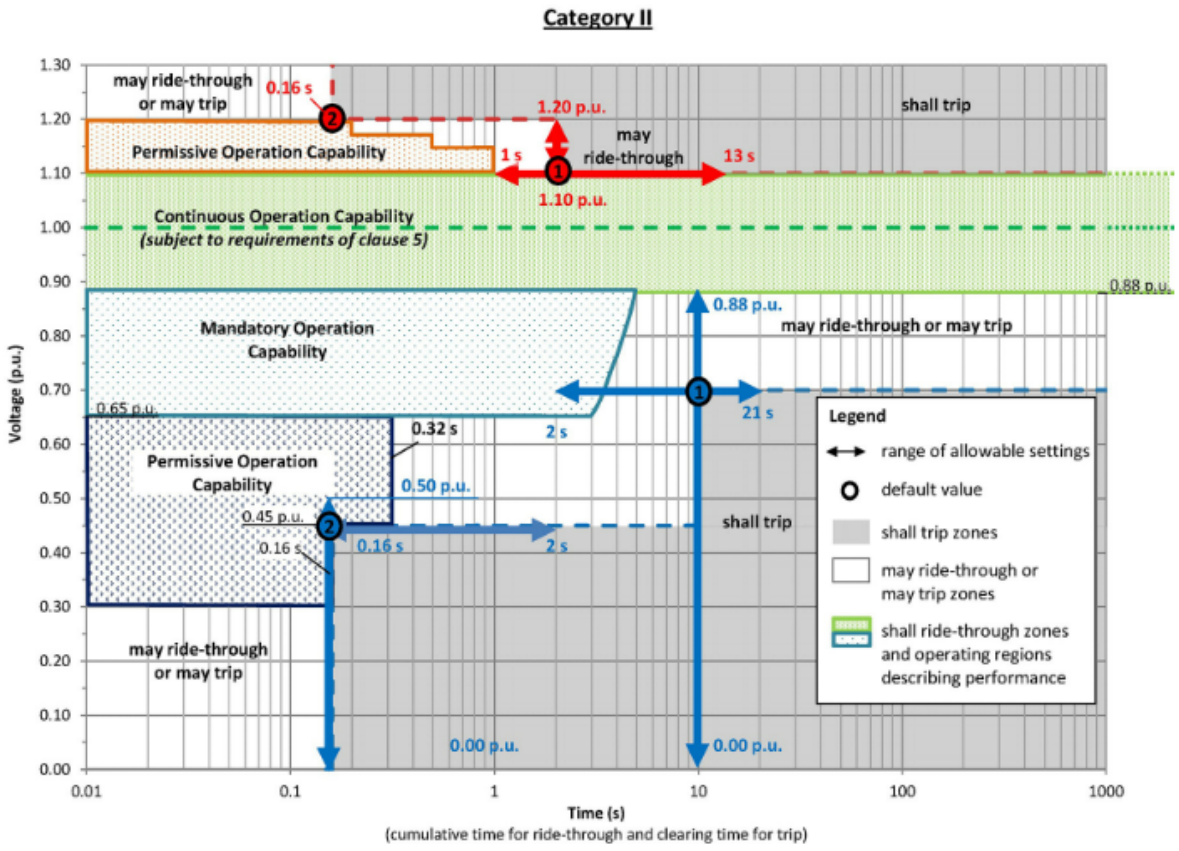

Figure 3.3: DER response for abnormal operating conditions Category II DERs [3].

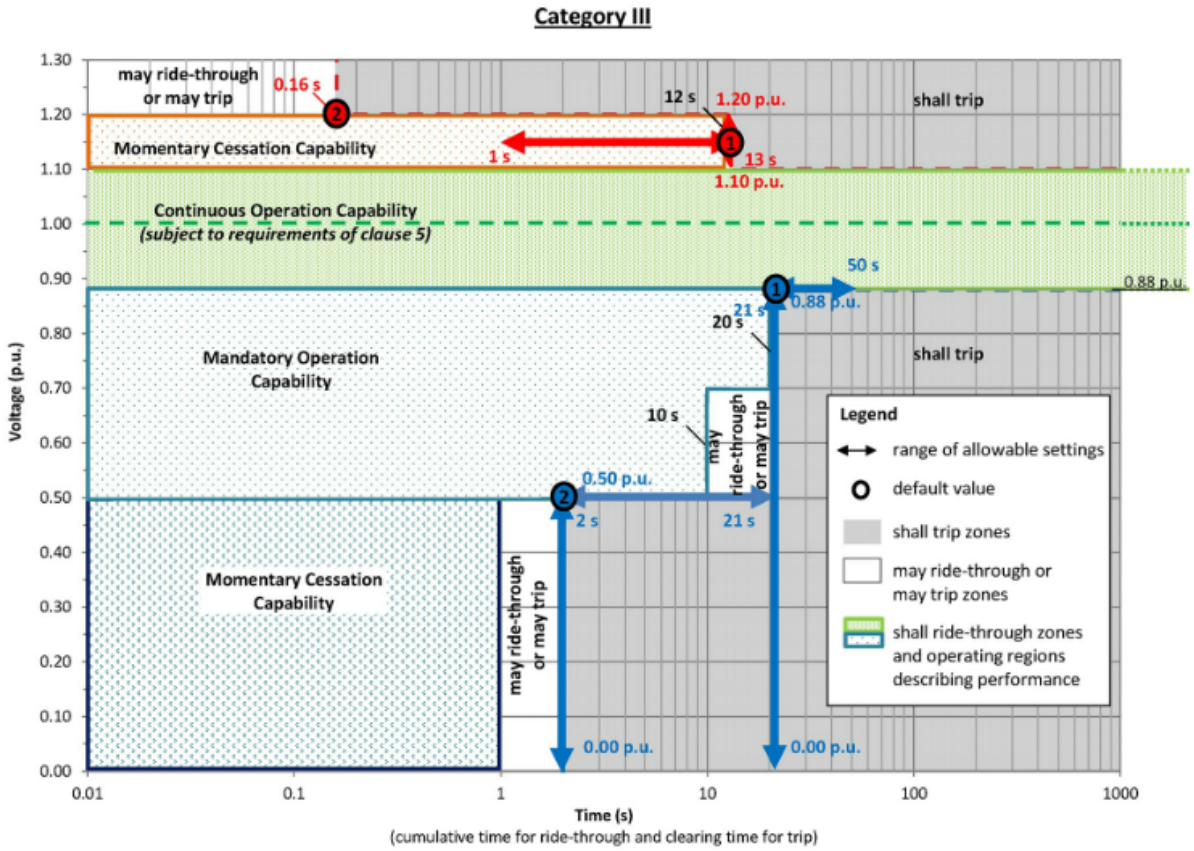

Figure 3.4: DER response for abnormal operating conditions Category III DERs [3].

3.4 Case Studies

3.4.1 Overview

A real power system in the desert southwest provided ASU with a 2025 Heavy Summer planning case power flow and dynamic data. The same system was studied in section 2.2, with composite load parameters updated in 2020. Also provided was the nameplate power ratings of the rooftop solar installed on each 69kV bus in the system. Based on work described in section 2.2 and published in [62], the composite load models were adjusted to include 30% of single-phase air conditioning load in the system to be VFD driven.

Then, 254 composite load models were converted to CMPLDWG using the DER_A representation for the R-DER in the composite load model. The power output of the DER on each bus modeled by CMPLDWG is added as Pdgen in the load table within the power flow.

The power output of the rooftop solar DER is closest to the nameplate value during the shoulder months in Arizona due to the high irradiance and favorable temperatures. However, FIDVR there is not enough single-phase motor load to cause FIDVR like there is in the Heavy Summer case. During the Heavy Summer case, the peak load is later in the day, and the temperature is far above the standard operating temperature at which nameplate ratings of PV cells are determined. Both of these factors combine to result in the power output of rooftop solar being far lower than the nameplate rating. For example, the system's peak load in 2020 was on July 30 at 5:00pm. The irradiance during peak load was 142 W/m2, and the temperature was 47.22°C (117°F). The standard irradiance and temperature for PV cells are 1000 W/m2 and 25°C (77°F). When the power output is derated for the Heavy Summer case to adjust for irradiance and ambient temperature, the power output by DER was about 19% of the nameplate rating of all the rooftop solar in the system. The DER output on many buses was reduced to 0 MW. The 2020 nameplate rating of rooftop solar was modeled with DER_A for the Heavy Summer case. As just described, this is more Pdgen is higher than would be expected in 2020, but might be a fair approximation of the derated rooftop solar production in 2025.

Work performed in [44] identified a critical faults for FIDVR in the power system. A three-phase fault is applied on a 230kV bus, Bus 100, and cleared after five cycles, 0.08s. The 69kV buses supplied by Bus 100 constitute Zone 100. The bus voltages in Zone 100 are monitored, and the 12.47kV load bus with the lowest post-fault voltage is selected for further examination. The bus identified as having the lowest post-fault voltage is named as Bus 112L and corresponds to the 12.47kV substation low-side Bus 112, and Bus 169 at 69kV, on which the CMPLDW model is represented. A simplified diagram showing the bus relationships is depicted in figure 3.5.

An additional case study was performed by applying another three-phase fault on a 230kV bus in an additional zone with a different load composition and rooftop solar penetration levels. The results of the additional case study reinforce the findings for the fault applied at Bus 100. The bus naming convention follows that of the case study presented.

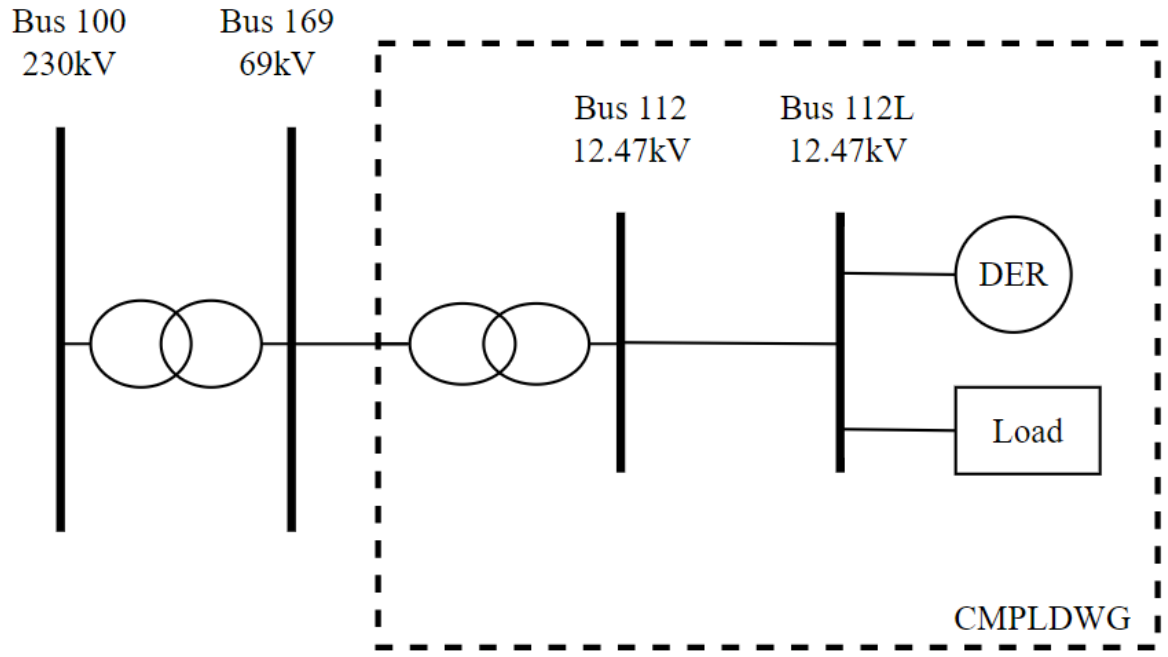

Figure 3.5: Simplified bus diagram. *Note*: This diagram does not depict the entire system. This diagram is to illustrate the relationship between buses described in this chapter. Information about the size of the full system is found in section 2.2.2

3.4.2 Protection Settings Case Study

Five different cases were studied with the faults described above: no rooftop solar modeled at all (called the baseline case in the following figures), DER modeled with IEEE Std 1547-2003 voltage protection parameters, DER modeled with IEEE Std 1547-2018 Category I response to abnormal voltage parameters, DER modeled with IEEE Std 1547-2018 Category II response to abnormal voltage parameters, and DER modeled with IEEE Std 1547-2018 Category III response to abnormal voltage parameters. Then, penetration studies were performed when the DER is modeled with IEEE Std 1547-2018 Category III response to abnormal voltage parameters used.

When a three-phase fault is applied on the 230kV Bus 100 at t = 1s and cleared after five cycles, a FIDVR event does occur. Bus 100 bus voltage falls below acceptable limits for 2 seconds before recovering to within the acceptable range. The 69kV bus, Bus 169, bus voltage drops to about 0.85 pu and takes approximately six seconds for the voltage to recover to its pre-fault value. Similarly, the 12.47kV load bus, Bus 112L, bus voltage drops to 0.6 pu after the fault and takes approximately six seconds for the voltage to return to the pre-fault value. Figures 3.6, 3.7, and 3.8 depict the Bus 100, 169, and 112L bus voltages when modeled with different IEEE Std 1547 protection setting requirements.

Category III with its requirement of low voltage ride through requirement for voltages as low at 0.5pu for up to one second is the only protection setting is the only one which does not cease operation during the period of several seconds of low voltage after the fault is cleared. Figures

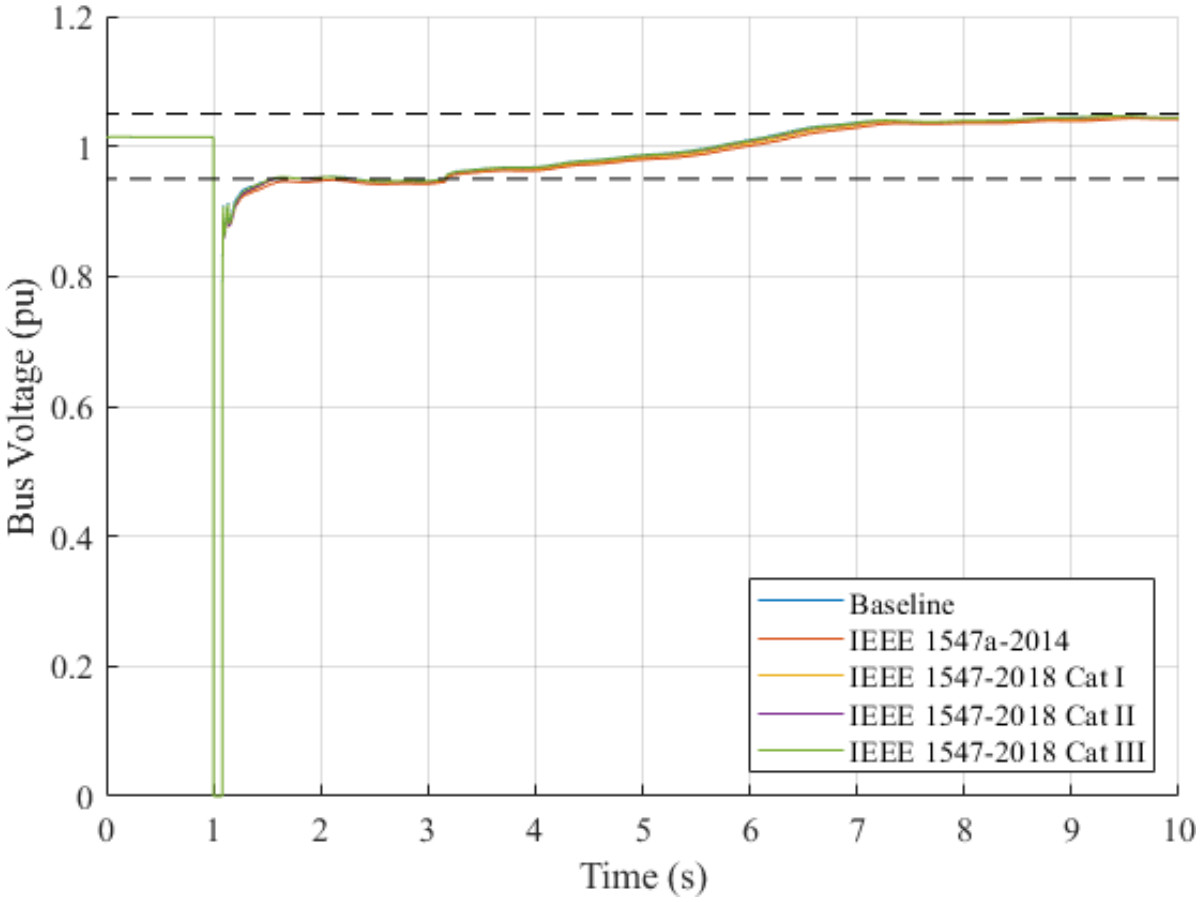

Figure 3.6: Bus 100 voltage after a fault with different DER protection settings modeled with DER_A.

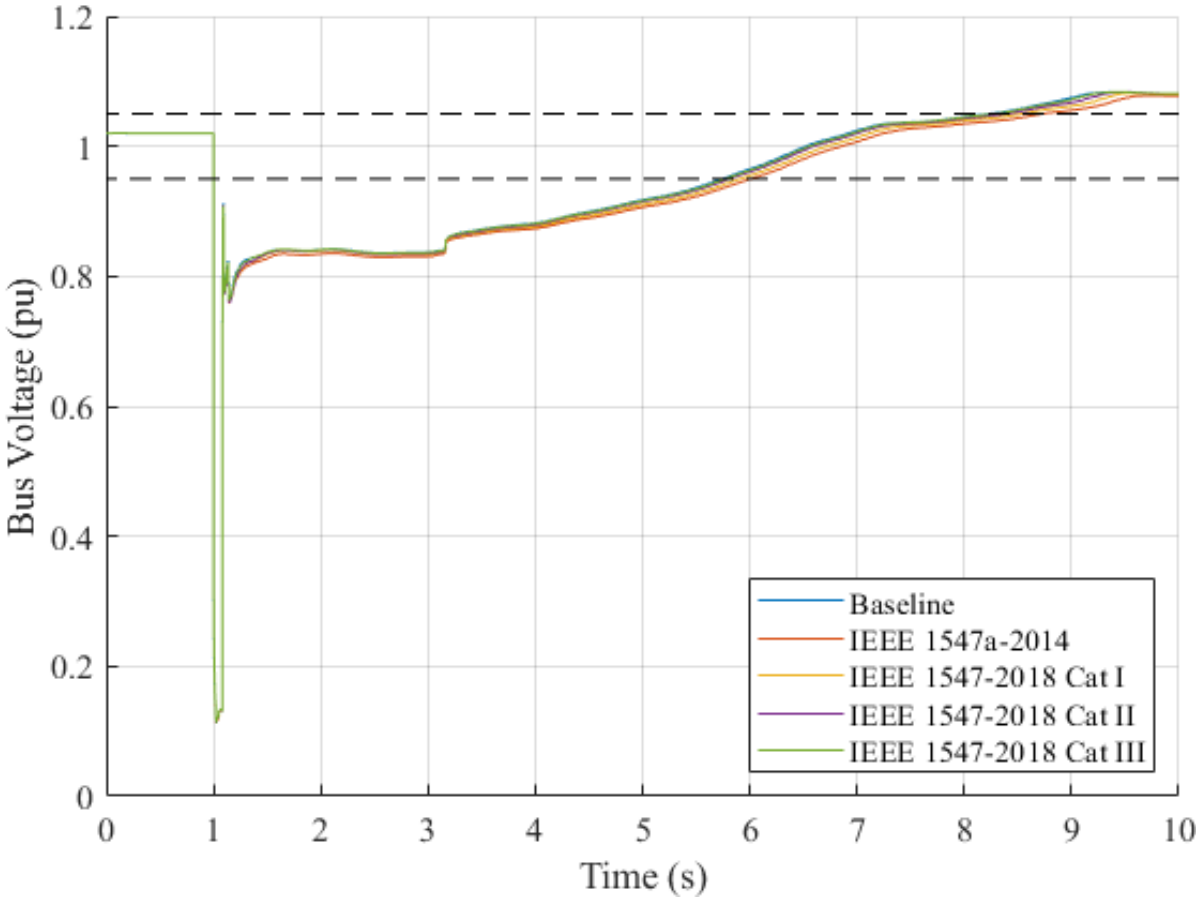

Figure 3.7: Bus 169 voltage after a fault with different DER protection settings modeled with DER_A.

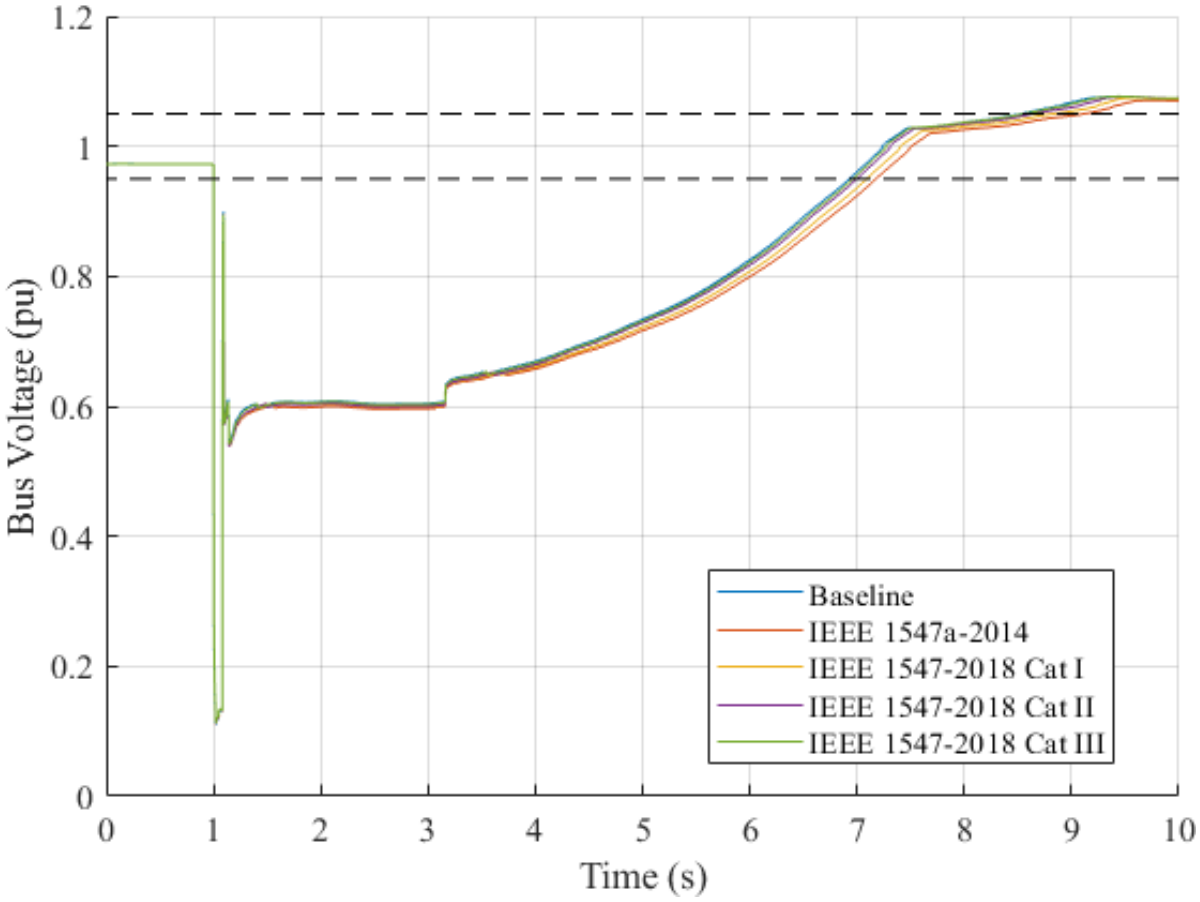

Figure 3.8: Bus 112L voltage after a fault with different DER protection settings modeled with DER_A.

3.9 and 3.10 show the active and reactive power generation by the rooftop solar on Bus 112L. Figure 3.11 depicts the fraction of rooftop solar installations which are not tripped by under- or over-voltage protection during the simulation length.

The rooftop solar panels with protection settings described in IEEE Std 1547-2003 [56] and IEEE Std 1547-2018 Category I [3] disconnect from undervoltage protection shortly after the fault occurs and do not reconnect for the simulation duration. The rooftop solar panels with IEEE Std 1547-2018 Category II protection setting are disconnected during the first several seconds after the fault is cleared, but reconnect as load shedding relays operate and Motor D thermal protection operates and voltage begins to recover. The Category II rooftop solar are operating within the permissive operating region, meaning per the standard they are allowed to either ride through and continue current exchange or momentarily cease. Per the model definition and parameters used, operation in the permissive region is treated as momentary cessation, which allows the Category II rooftop solar to resume current exchange when the bus voltage recovers, as opposed to tripping and staying disconnected like the IEEE Std 1547-2003 and IEEE Std 1547-2018 Category I rooftop solar did. Both Category II and Category III modeled rooftop solar begin disconnecting from overvoltage protection as the FIDVR event enters its characteristic overvoltage following tripping of motor loads.

Rooftop solar modeled with Category III protection settings, momentarily cease operation during the fault, but both active and reactive current are injected into the power system after the fault is cleared. The active power is curtailed somewhat compared to the pre-fault values so that the rooftop solar and inject more reactive power into the system while providing dynamic voltage support.

3.4.3 Rooftop Solar Penetration Case Study

From the examination of the results of faults when DER is modeled with different response to abnormal voltage settings, it became clear that only when DER was modeled as IEEE Std 1547-2018 Category III was there any improvement upon the baseline case. Therefore, DER modeled as IEEE Std 1547-2018 Category III was chosen to for a penetration study. The baseline case (no DER modeled) was compared with rooftop solar DER modeled as IEEE Std 1547-2018 Category III at 100%, 200%, 300%, and 400% nameplate rated power output. The same faults were studied as described in section 3.4.1: a three-phase fault applied on Bus 100 at t = 1s and cleared after five cycles.

When a three-phase fault is applied on Bus 100 at t = 1s and cleared after five cycles, a FIDVR event does occur. Bus 100 bus voltage remains within acceptable limits for the duration of the fault. However, the Bus 169 bus voltage drops to about 0.83 pu without DER and 0.85 pu with 400% nameplate DER. It takes 0.26 seconds longer for voltage to return to its pre-fault value in the baseline case than in the 400% nameplate DER. Similarly, Bus 112L bus voltage drops to about 0.61 pu without DER and 0.63 pu with 400% nameplate DER. It takes 0.25 seconds longer for load bus voltage to return to its pre-fault value in the baseline case than in the 400% nameplate DER.

Figures 3.12, 3.13, and 3.14 depict the bus voltage with increasing penetration of rooftop solar modeled with Category III protection settings. It is easy to see that there is very minimal improve-

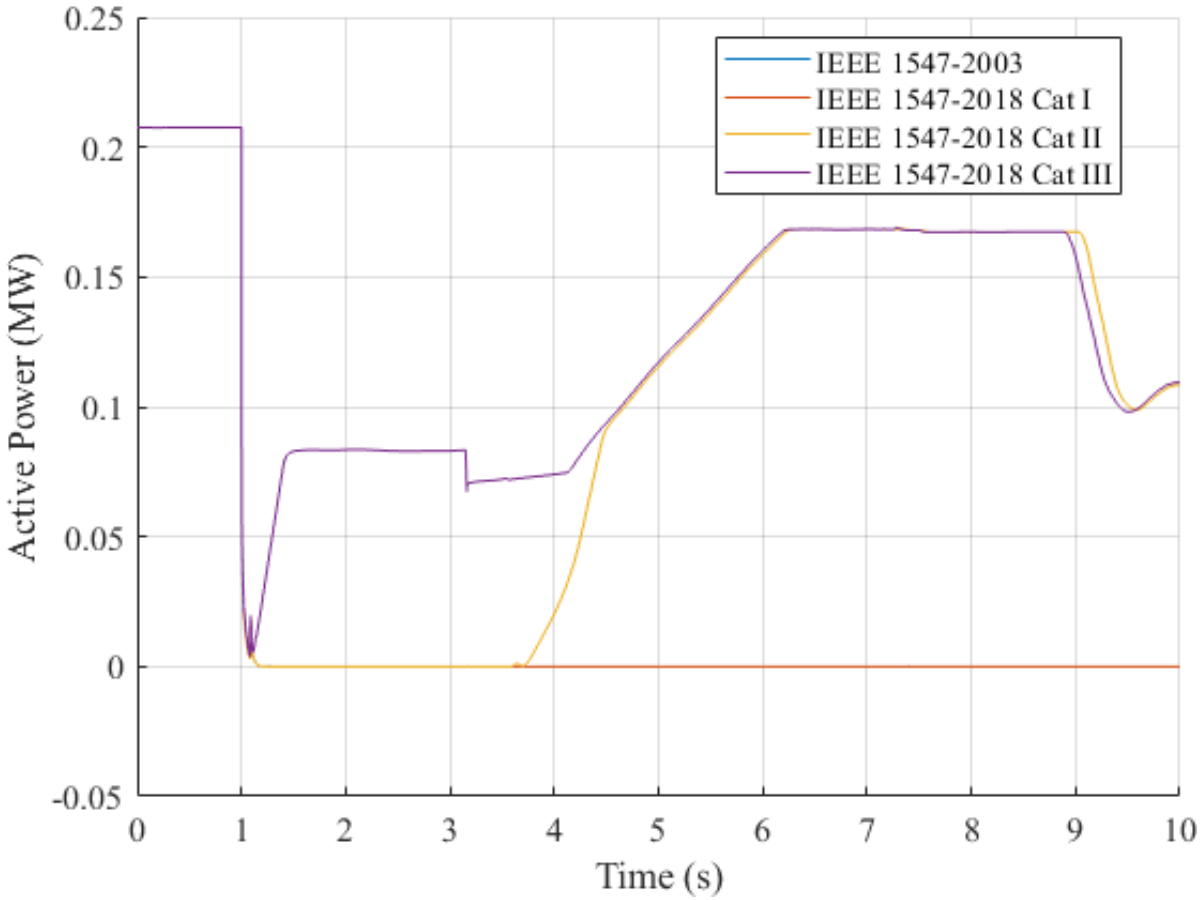

Figure 3.9: Active power generated by rooftop solar connected to Bus 112L.

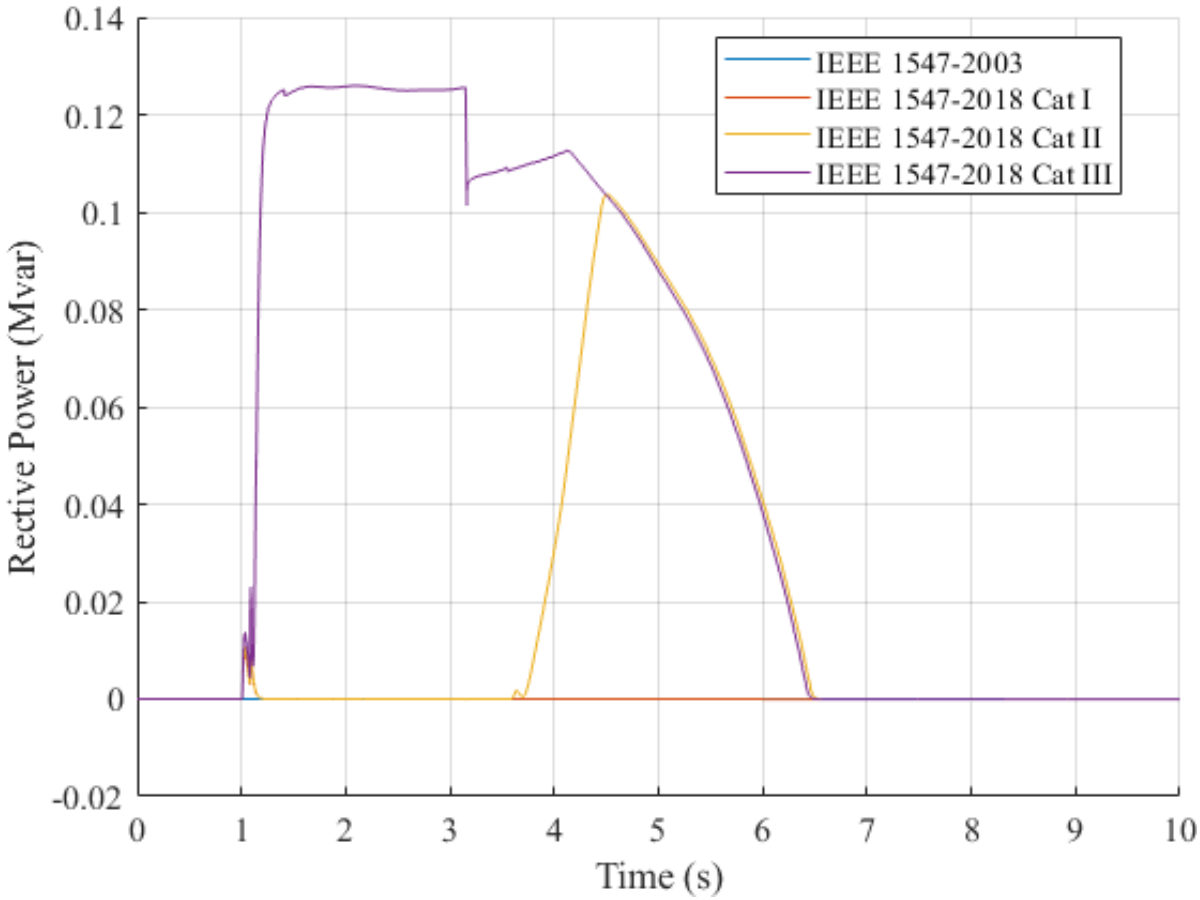

Figure 3.10: Reactive power generated by rooftop solar connected to Bus 112L.

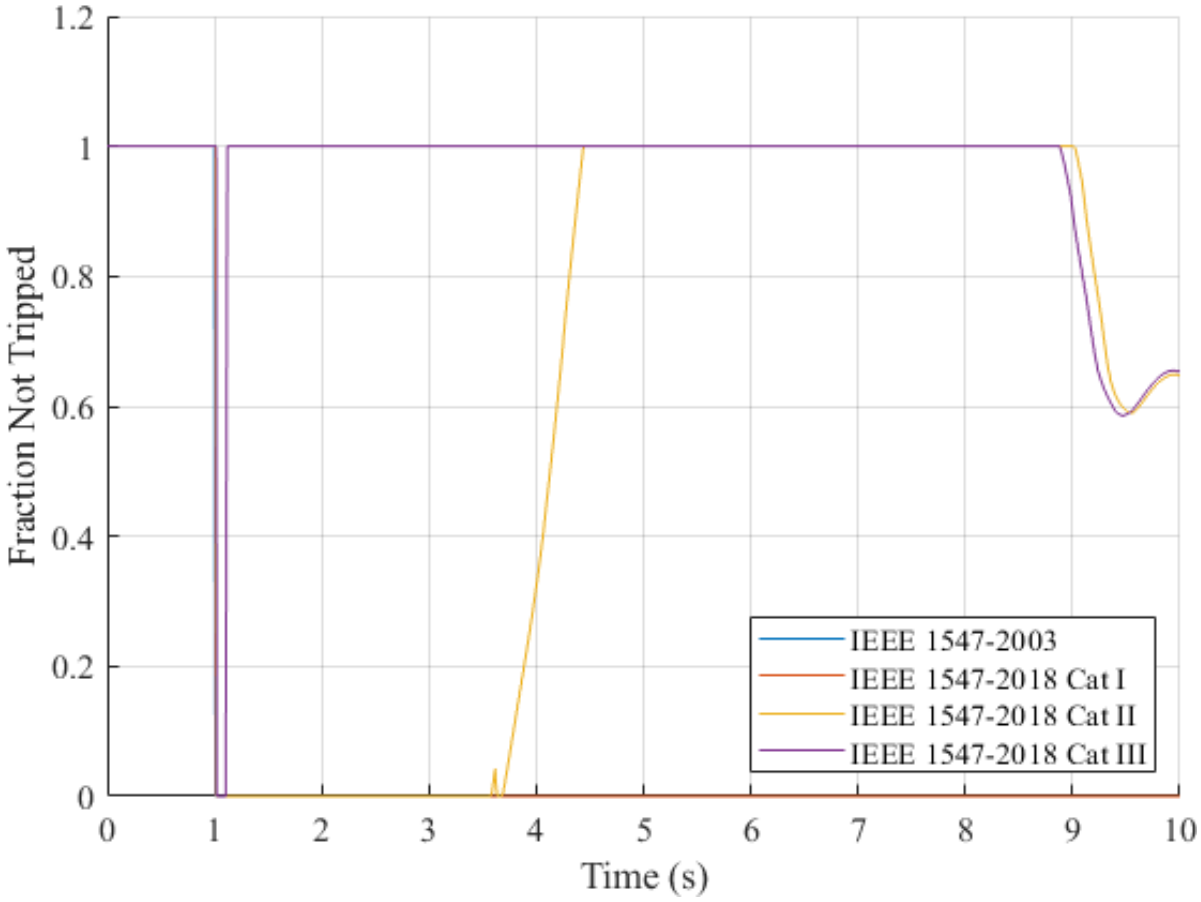

Figure 3.11: Fraction of solar panels connected to Bus 112L not tripped by under- or over-voltage protection relays.

ment in the recovery of FIDVR even when there is a substantial increase in rooftop solar penetration with very strict low voltage ride through requirements.

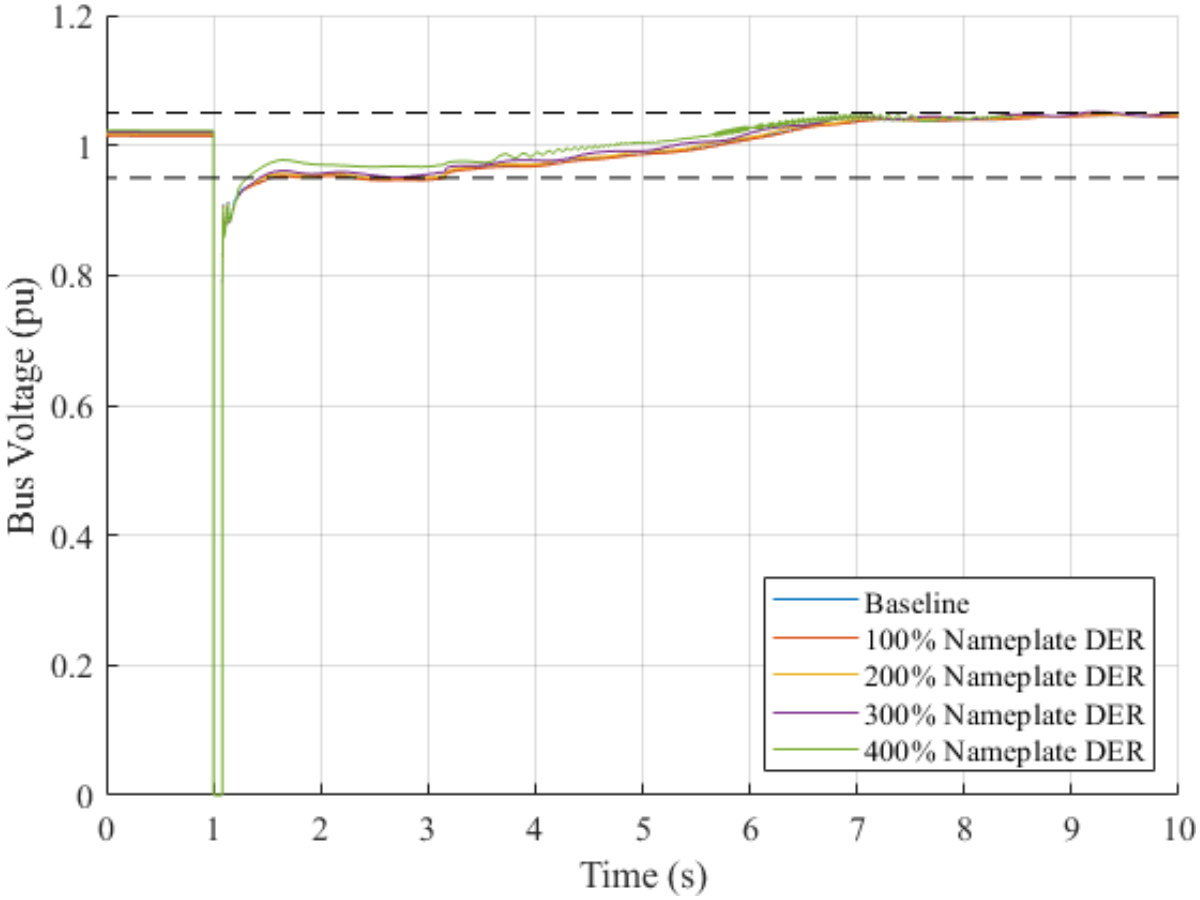

Figure 3.12: Bus 100 voltage after a fault with increasing penetration of rooftop solar modeled with DER_A.

3.5 Conclusions

The publication of IEEE Std 1547-2018 includes a wider range of technical requirements for interconnections with DERs to ensure that electric power systems maintain reliable operation with higher penetrations of DERs. The DER_A model is able to model aggregate DERs, such as rooftop solar, with fewer parameters required than previous methods of modeling renewable energy sources. DER_A can be used to model inverters which follow older DER interconnection standards such as IEEE Std 1547-2003 and IEEE Std 1547a-2014, DERs which use smart inverters per California Rule 21 and IEEE Std 1547-2018, and a mixture of DERs of various vintages and standards.

When DER_A model is used to model the rooftop solar in a real power system to investigate the effect on FIDVR, there turns out to be very little difference between the different DER standards. However, only for DERs following IEEE Std 1547-2018 Category III response to abnormal system voltage settings is there reliably improved results from the baseline case. Furthermore, an increase in

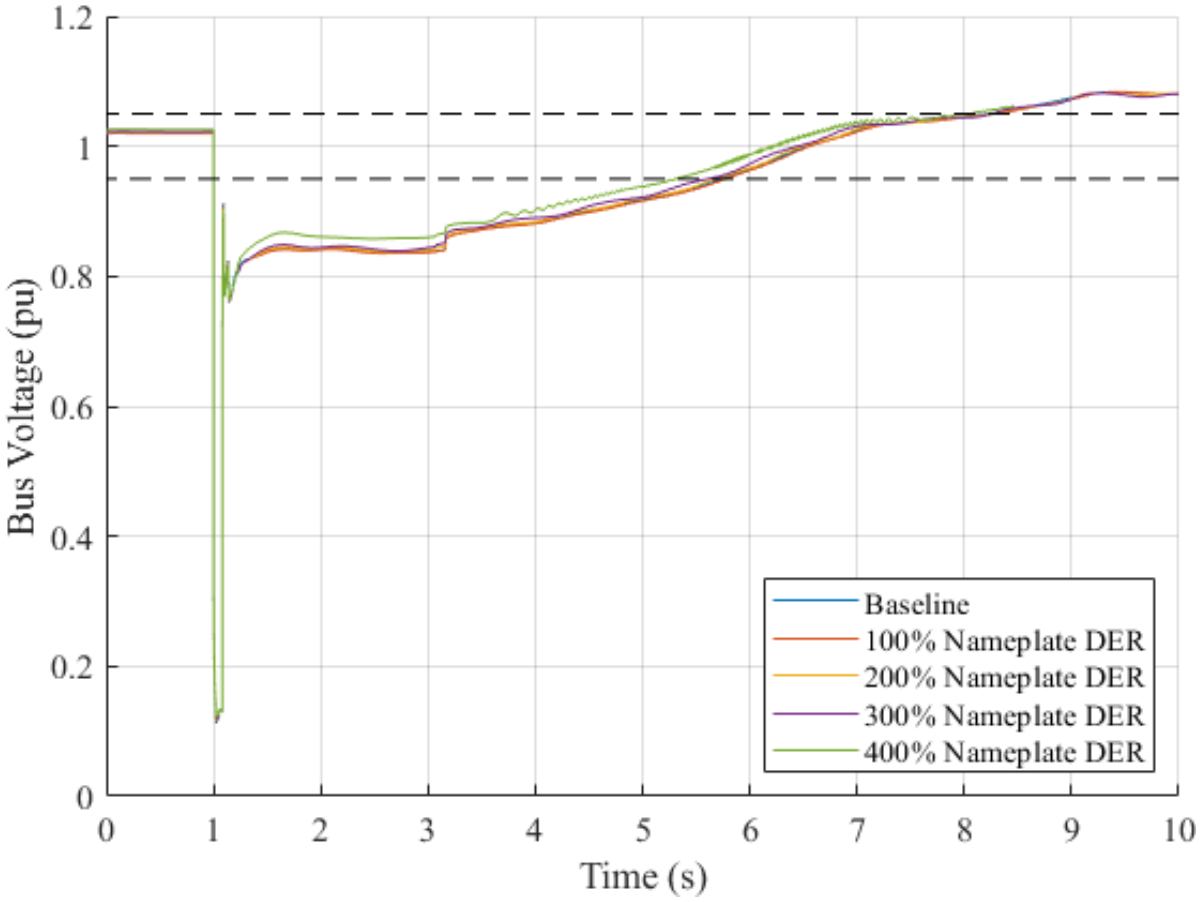

Figure 3.13: Bus 169 voltage after a fault with increasing penetration of rooftop solar modeled with DER_A.

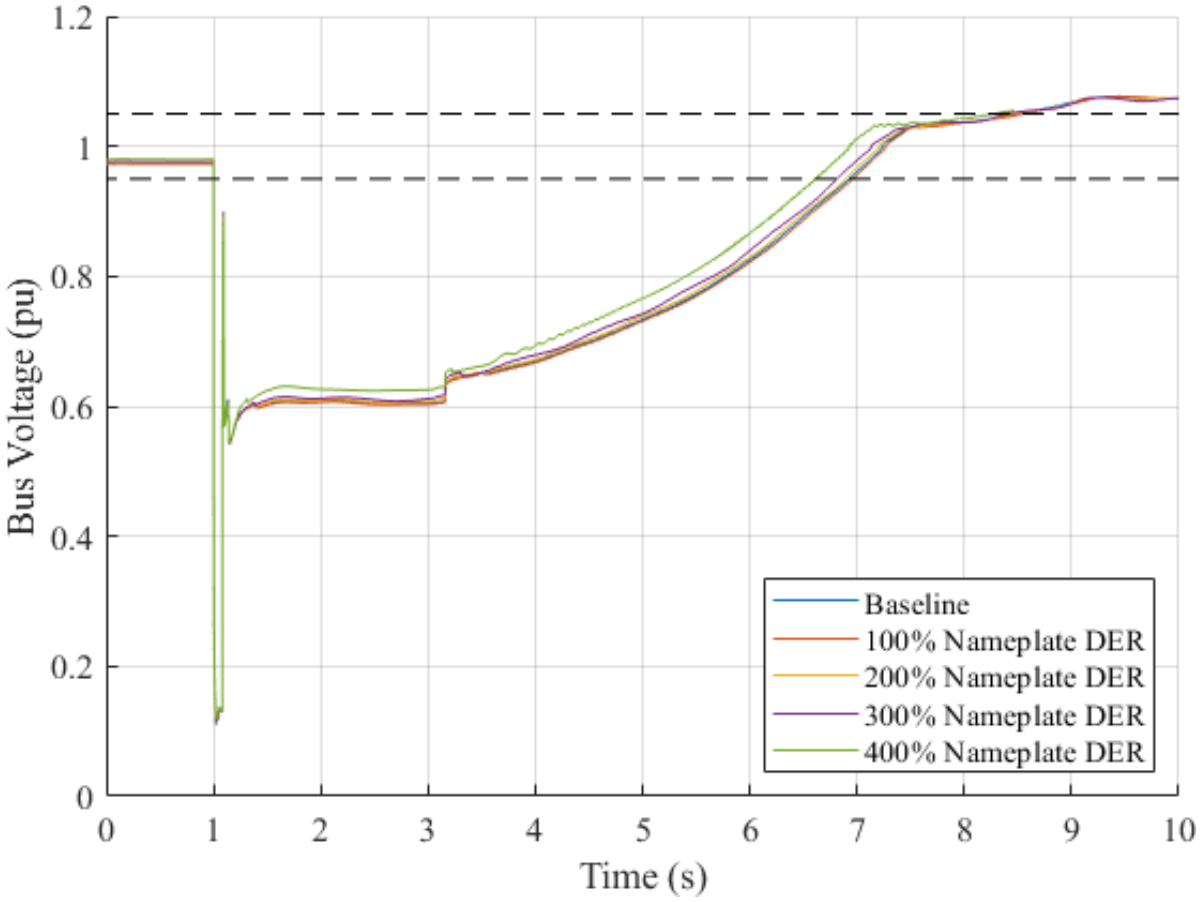

Figure 3.14: Bus 112L voltage after a fault with increasing penetration of rooftop solar modeled with DER_A.

penetration of DERs all following the Category III requirements leads to only marginal improvement in post-fault voltage sag and voltage recovery time.

4. Transmission and Distribution Coordination for DER Wholesale Market Participation: A Parametric Programming Approach

4.1 Introduction

US Federal Energy Regulatory Commission issued Order No. 2222 to promote wholesale market competition by leveraging the market participation of distributed energy resources (DERs) [63]. Integrating numerous small DERs into today's wholesale market causes challenges for the independent system operators (ISOs) as 1) it imposes complexity and computational burden; and 2) it could cause distribution grid voltage/thermal violations if the aggregator-controlled DERs are not properly monitored by system operators. An effective solution to this problem is considering the distribution system operator (DSO) which runs the retail market to coordinate the DERs market participation while assuring the secure/reliable operation of the distribution grid [64]. However, there is a need for a coordination framework between the ISO and the DSO.

Recent works studied the ISO-DSO coordination problem [65–73]. They fall into two categories based on the solution method. The first category proposed bi-level and transformed the problem to single level optimization [65, 66]. In [65], a bi-level optimization model is proposed for DSO market clearing and pricing considering ISO-DSO coordination. The clearing conditions for the DSO and ISO markets are proposed in the upper-level and lower-level problems, respectively. The problem is converted to mixed-integer linear programming via an equilibrium problem with equilibrium constraints (EPEC) approach. In [66] a bi-level optimization model is proposed for the energy storage sizing and siting problem in the DSO-ISO coordination framework. However, bilevel optimization is hard to solve for large systems.

The second category of works uses decentralized and decomposition algorithms [67–73]. In [67], an extension of the decentralized market framework is proposed to consider loss allocation and its impact on the market outcome. However, the decentralized market framework is not compatible with the current market structures. In [68], a transactive market framework starting from the ISO to the DSO is proposed. The DSO runs the transactive market using an iterative method. However, the convergence of the proposed method is not guaranteed. In [69], a Nash bargaining-based method is proposed for the market-clearing process and the ISO-DSO coordination. However, there is no guarantee that the proposed algorithm converges especially when the number of DSOs increases. In [70], a three-stage unit commitment (UC) is proposed for the transmission-distribution coordination. A convex AC branch flow model is proposed to handle the distribution grid physical constraints. In [71], a distributed optimization algorithm is proposed for modeling the DSO retail market considering energy and ancillary services. However, the DSO's impact on wholesale market clearing is not considered. In [72], the optimal operation and coordination of the ISO-DSO is proposed. A decomposition algorithm is proposed and the original problem is decomposed to ISO and DSO sub-problems. In [73], a non-cooprative game approach is proposed for ISO-DSO coordination in which they optimize their own operational costs. The approaches in [70, 72, 73] are hard to solve for large systems.

This chapter proposes an ISO-DSO coordination framework based on parametric programming. The DSO builds the bid-in cost function (submitted to the ISO), considering its retail market

participants' offering prices and their operational constraints as well as physical constraints of the distribution grid including power balance equations and voltage limitation constraints. To our best knowledge, this is the first attempt which shows the parametric programming based DSO offers optimal interactions with existing ISO markets. Different from existing approaches facing computational difficulties for large-scale ISO-DSO coordination, this work could lead to a coordinated ISO-DSO market clearing procedure which is computationally efficient and scalable toward large-scale systems with many DSOs and numerous DER aggregators. This work is an extension to our recent work [64] to present a coordination framework for the DSO and ISO which is practical with the current wholesale market structures.

4.2 DER Market Participation Framework

4.2.1 Direct Participation of the DERs in the ISO Market

This section presents the ideal case for DER market participation. This ideal case assumes the DERs participate in the ISO's wholesale market directly, and the ISO considers not only transmission-level operating constraints but also distribution grid physical constraints to ensure transmission and distribution security operations, since the DERs are located in the distribution grid. It is assumed that the ISOs have revised their tariffs such that DERs can participate in the wholesale market under one of the participation models. A unified formulation for the security constrained UC and economic dispatch (ED) problem of this ideal case is as follows:

$$\text{Min}_{x,q} \quad \sum_{t\in T}\sum_{i\in N} c_{i,t}(x_{i,t-1}, x_{i,t}, q_{i,t}) \tag{4.1}$$

$$\begin{aligned} \text{s.t.} \quad & (x, q) \in S^{Tra} \\ & (x, q) \in S^{Dis} \\ & (x_{i,t-1}, x_{i,t}, q_{i,t-1}, q_{i,t}) \in S_i^{player}, \forall i, t \\ & x_{i,t} \in \{0, 1\}, q_{i,t} \in \mathbb{R}^1, \forall i, t \\ & c_{i,t}(x_{i,t-1}, x_{i,t}, q_{i,t}) : \mathbb{R}^3 \mapsto \mathbb{R}^1, \forall i, t \end{aligned} \tag{4.2}$$

where t (T) and i (N) are the index (set) for the operating timespan and the market participants (generators/aggregators), respectively; $x_{i,t}$, $q_{i,t}$, and $c_{i,t}(x_{i,t-1}, x_{i,t}, q_{i,t})$ are the binary UC decision variable (start-up/shut-down), continuous ED decision variable (dispatched power), and bid-in cost function (with UCED decisions) of market participant i at time t, respectively; x and q denote the vectors of $x_{i,t}$ and $q_{i,t}$ for $t \in T$ and $i \in N$, respectively; S^{Tra}, S^{Dis}, and S_i^{player} denote the search space defined by the system-wide transmission grid constraints, system-wide distribution grid constraints, and operating constraints of the market participant i, respectively.

This is the ideal case for DERs' wholesale market participation. However, implementing this procedure is not possible for ISOs since 1) it adds many variables/constraints to the ISO problem from the distribution grids, making the ISO problem computationally expensive; and 2) it increases the ISO's burden on modeling the distribution-level constraints in its market clearing problem, while the distribution-level models/constraints are currently not available to ISOs.

4.2.2 Market Participation of the DERs through DSO and ISO Coordination Framework

This section presents our proposed ISO-DSO coordination framework. This framework decomposes the ideal case in Section II.A into an ISO sub-problem and several DSO sub-problems (one for each distribution system). This decomposition reduces the ISO's modeling and computation burdern by 1) considering distribution-level operating security in the DSO sub-problems; 2) considering distribution-level variables/constraints and optimization computations in the DSO sub-problems; and 3) introducing minimal changes to the existing ISO market structures. Without the DSO-level market, market participation of all the aggregators need to be handled by the ISO. These aggregators are modeled as numerous small generators in the ISO's UCED problem presented by (4.1)-(4.2). If locational marginal pricing (LMP) is adopted by the ISO and DSO markets, the market clearing outcomes of this ISO-DSO coordination framework are identical to those of the ideal case in Section II.A.

Each DSO is defined as a mediator which gathers offers from the DER aggregators to submit an aggregated bid to the wholesale energy market. The DER aggregators submit their offers to the DSO. The DSO gathers these offers and runs the retail market to build an aggregated offer to participate in the ISO wholesale market. Considering the DSOs as wholesale market participants, the wholesale market (ISO) security constrained UCED problem is as follows:

$$\text{Min}_{x,q} \quad \sum_{t\in T} \sum_{i\in N_{gen}\cup N_{dso}} c_{i,t}(x_{i,t-1}, x_{i,t}, q_{i,t}) \tag{4.3}$$

$$\begin{aligned} \text{s.t.} \quad & (x, q) \in S^{Tra} \\ & (x_{i,t-1}, x_{i,t}, q_{i,t-1}, q_{i,t}) \in S_i^{gen}, \forall i \in N_{gen}, \forall t \\ & (x_{i,t-1}, x_{i,t}, q_{i,t-1}, q_{i,t}) \in S_i^{dso}, \forall i \in N_{dso}, \forall t \\ & x_{i,t} \in \{0, 1\}, q_{i,t} \in \mathbb{R}^1, \forall i, t \\ & c_{i,t}(x_{i,t-1}, x_{i,t}, q_{i,t}) : \mathbb{R}^3 \mapsto \mathbb{R}^1, \forall i, t \end{aligned} \tag{4.4}$$

where N_{gen} and N_{dso} are the set of all generaors and DSOs in the wholesale market, respectively; S_i^{gen} and S_i^{dso} denote the search space defined by operating constraints of individual generators and DSOs, respectively; $N = N_{gen} \cup N_{dso}$.

Each DSO submits its bid-in cost function to the ISO's UCED problem in (4.3)-(4.4), following the ISO-defined non-convex cost function structure $c_{i,t}^{dso}(x_{i,t-1}, x_{i,t}, q_{i,t})$. Considering aggregator controlled DERs do not have start-up/no-load costs or binary UC decision variables, the bid-in cost function of aggregator j within DSO i at time t reduces to $c_{i,j,t}^{agg}(q_{i,j,t}^{agg})$, which is convex (piecewise linear/quadratic in many markets), where $q_{i,j,t}^{agg}$ is the bid-in power quantity of this aggregator to the DSO. The bid-in cost function of the DSO i, $c_{i,t}^{dso}(q_{i,t}^{dso})$ to be submitted to ISO (where $q_{i,t}^{dso}$ is the bid-in power quantity of this DSO to the ISO), is determined by following optimization problem

(for single-period DSO markets):

$$
\begin{aligned}
c_{i,t}^{dso}(q_{i,t}^{dso}) = \text{Min}_{q^{agg}} \quad & \sum_{j \in DSO_i} c_{i,j,t}^{agg}(q_{i,j,t}^{agg}) \\
\text{s.t.} \quad & q_{i,t}^{dso} \leq \sum_{j \in DSO_i} q_{i,j,t}^{agg} \\
& q_{i,j,t}^{agg} \in S_{i,j}^{agg}, \forall j \in DSO_i \\
& q^{agg} \in S_i^{Dis}
\end{aligned}
\tag{4.5}
$$

where DSO_i is the set of all aggregators in i^{th} DSO; $S_{i,j}^{agg}$ is the search space defined by operational constraints of individual aggregators within each DSO; S_i^{Dis} is the search space defined by the physical constraints of each DSO (i.e., the distribution system); q^{agg} is the vector of $q_{i,j,t}^{agg}$ for $j \in DSO_i$.

For a single-period DSO market, Equation (4.5) is a parametric convex optimization problem parameterized by a single parameter $q_{i,t}^{dso}$, since its objective function is sum of convex bid-in cost functions from aggregators, and its constraints are all linear. The optimal solution of (4.5) is a function of parameter $q_{i,t}^{dso}$ which is the bid-in cost function of i^{th} DSO, $c_{i,t}^{dso}(q_{i,t}^{dso})$. Based on approximate multi-parametric convex programming [74], the optimal bid-in cost function from DSO to ISO, $c_{i,t}^{dso}(q_{i,t}^{dso})$, is also a convex function of parameter $q_{i,t}^{dso}$. If the aggregator bid-in cost functions are (piecewise) linear (following the cost function structure in existing ISOs), this problem reduces to a parametric linear optimization. Based on theories of multi-parametric linear programming [75,76], the resulting $c_{i,t}^{dso}(q_{i,t}^{dso})$ is also (piecewise) linear, following the cost function structure in many existing ISO markets. The optimal outcomes of (4.5) determines: 1) the optimal bid-in cost function $c_{i,t}^{dso}(q_{i,t}^{dso})$ submitted from DSO to ISO (the minimal operating cost for DSO to offer $q_{i,t}^{dso}$ MW of generation/consumption in the ISO market); and 2) the optimal dispatch of total DSO generation/consumption $q_{i,t}^{dso}$ among all aggregators $q_{i,j,t}^{agg}$ to achieve minimal operating cost. Retail LMPs can be obtained by the dual model (not discussed in this chapter). If a multi-period DSO market is considered, this problem generalizes to a multi-parametric convex optimization problem and all the above discussions are still valid.

This convex (multi)-parametric-programming-based retail energy dispatch can be solved by existing multi-parametric programming solvers [77–79]. If single-period market clearing is considered (currently implemented by many real-world ISOs, as shown in (4.5)), this problem boils down to a convex parametric programming problem parameterized by a single parameter. To solve this single-period DSO market clearing problem, we have adopted sensitivity analysis procedure, in which we gradually adjust $q_{i,t}^{dso}$ by a pre-defined small step size and solve the optimization in (4.5) at each step to obtain $c_{i,t}^{dso}(q_{i,t}^{dso})$. The range for adjusting $q_{i,t}^{dso}$ is determined by upper/lower generation limits of individual DER aggregators.

The parametric programming in (4.5) is further expanded to obtain detailed formulation for the DSO market. The bid-in cost function of each DSO is determined by solving (4.6)-(4.14):

$$
c^{dso}(P^{dso}) = Min \sum_{g \in G} \sum_{b \in B} P_{g,b} \pi_{g,b} - \sum_{d \in D} \sum_{b \in B} P_{d,b} \pi_{d,b} \tag{4.6}
$$

s.t.

$$\sum_{d\in D}\sum_{b\in B} H_{n,d}P_{d,b} + H_n^{sub}P^{dso} + L_n^P - \sum_{g\in G}\sum_{b\in B} H_{n,g}P_{g,b} + \sum_{j\in J} Pl_j A_{j,n} = 0; \quad \forall n \in N \tag{4.7}$$

$$\sum_{d\in D}\sum_{b\in B} H_{n,d}P_{d,b}tan\phi_d + H_n^{sub}Q^{dso} + L_n^Q - \sum_{g\in G}\sum_{b\in B} H_{n,g}P_{g,b}tan\phi_g + \sum_{j\in J} Ql_j A_{j,n} = 0; \forall n \in N \tag{4.8}$$

$$0 \le P_{g,b} \le P_{b,g}^{max}; \quad \forall b \in B, \forall g \in G \tag{4.9}$$

$$0 \le P_{d,b} \le P_{d,g}^{max}; \quad \forall b \in B, \forall d \in D \tag{4.10}$$

$$U_m = U_n - 2(r_j Pl_j + x_j Ql_j); \quad \forall m \in N, \quad \forall n \in N,\ C(m,n) = 1,\ A(j,n) = 1 \tag{4.11}$$

$$\underline{U} \le U_n \le \overline{U}; \quad \forall n \in N \tag{4.12}$$

$$-Pl^{max} \le Pl_j \le Pl^{max}; \quad \forall j \in J \tag{4.13}$$

$$-Ql^{max} \le Ql_j \le Ql^{max}; \quad \forall j \in J \tag{4.14}$$

where t and T are the index and set for the entire operating timespan; g and G are the index and set for all generating aggregators; d and D are the index and set for all demand response aggregators; b and B are the index and set for all production/demand blocks; j and J are the index and set for all lines; n and N are the index and set for all nodes; P^{dso} is the DSO's aggregated offers (in MW) to ISO market; $P_{g,b}$ are $P_{d,b}$ are energy offer submitted by the generating aggregators and demand response aggregators, respectively with corresponding prices $\pi_{g,b}$ and $\pi_{d,b}$, respectively; $H_{n,d}$, $H_{n,g}$, and H_n^{sub} are mapping matrix of generating aggregators, demand response aggregators, substation to node n, respectively; Pl_j and Ql_j are the active and reactive power of branch j, respectively; $A_{j,n}$ is the incidence matrix of branches and nodes; ϕ_g and ϕ_d are the phase angle of the generating aggregators and demand response aggregators, respectively; Q_n^D is the reactive power of the firm load at each node; L_n^P and L_n^Q are the active and reactive power load at each node; $P_{g,b}^{max}$ and $P_{d,b}^{max}$ are the maximum production/consumption at each block of the generating aggregators and demand response aggregators, respectively; U is the square of voltage of each node; $\underline{U}$ and $\overline{U}$ are the square of minimum and maximum permitted voltage values, respectively; r_j and x_j are resistance and reactance of the branches; Pl^{max} and Ql^{max} are maximum active and reactive power of branches.

Equation (4.6) defines the DSO's objective function to minimize the total system cost. Equations (4.7)-(4.8) define the active and reactive power balance equations, respectively. The produced/consumed power at each block of the generating aggregators and demand response aggregators are limited by (4.9)-(4.10), receptively. The price responsive demand is considered in this model. Voltage at each node is defined by (4.11). The minimum and maximum voltage limitations are met by (4.12). Constraints (4.13)-(4.14) limit the active and reactive power of each branch, respectively. More details for this DSO problem are in our prior work [64]. For simplicity, formulation (6)-(14) is presented for single-period markets and can be extended to consider multi-period markets.

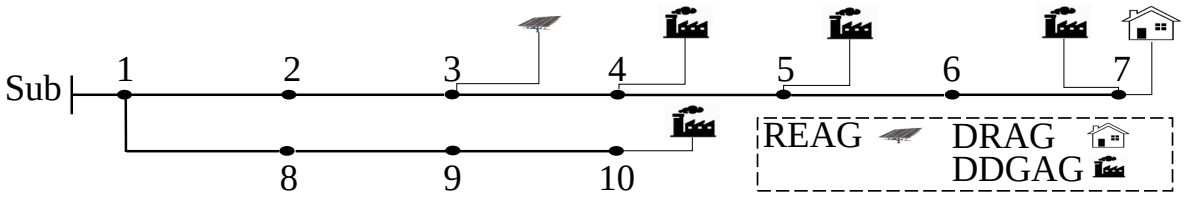

Figure 4.1: The small distribution network for case studies.

Table 4.1: Wholesale market participants information

Participant	Pmin (MW)	Pmax (MW)	Offering price ($/MWh)
Gen 1	0	10	8
Gen 2	0	20	20
Gen 3	0	30	22
DR 1	0	10	30
DR 2	0	20	32
DR 3	0	20	34

The ISO gathers the bid-in cost function of the all DSOs and other market participants to run the wholesale market and determine the share of the all market participants including DSOs. Note that we need to determine the bid-in cost function for each DSO. Once we provide these cost functions, we can submit them to the ISO. Then ISO will clear the wholesale market and determine the share of each DSO in the ISO market. The merit of this procedure is that the ISO does not need to know the inner (distribution-level) constraints of the DSOs. This means that ISO does not need to consider a lot of variables and constraints to ensure the DERs' wholesale bidding activities do not cause voltage/thermal violations in the distribution grids. If LMP is adopted in the ISO-DSO markets, market clearing outcomes of this framework are the same as those of the ideal case in Section II.A, as the ISO is considering market participation of the small DER aggregators in the wholesale market (through the DSO). This is due to the fact that every share that ISO determines for each DSO lies on the best response function of that DSO (already submitted to the ISO). Hence, the results are the same as those in the ideal case when DERs participate in the ISO market directly. Due to space limitation, mathematical proofs are not included.

In the DSO problem, a parameter P^{dso} determines the amount of the power imported/exported from/to the ISO. In other words, the DSO is considered as a unit that is going to determine the cost function or demand function based on its generating units and demand response units as well as physical constraints of the distribution network. Indeed, the resulting cost function determines the true value cost of the energy consumed or produced in the distribution network considering all the physical constraints of the distribution network.

Table 4.2: DSO market participants information

Participant	Pmin (MW)	Pmax (MW)	Offering price ($/MWh)
DDGAG 1	0	0.5	20
DDGAG 2	0	1	10
DDGAG 3	0	1.2	15
DDGAG 4	0	2	24
DRAG	0	20	28

Table 4.3: ISO market outcomes in the ideal case

Participant	Share (MW)	Participant	Share (MW)
Gen 1	10	DDGAG 1	0.5
Gen 2	20	DDGAG 2	1
Gen 3	13.8	DDGAG 3	1.2
DR 1	10	DDGAG 4	0
DR 2	20	DRAG	2.5
DR 3	10		

4.3 Simulation Results

The case studies are implemented on a small system containing the ISO running wholesale-level ED and a small distribution network operated by the DSO shown in Fig. 4.1. In the wholesale-level ED, three generating units, three demand response units, and a firm load of 5 MW is considered. The generating units (Gen) and demand response (DR) units information is in Table. 4.1. The distribution system in Fig. 4.1 includes 10 nodes, 9 lines, 4 dispatchable distributed generation aggregators (DDGAG), 1 renewable energy aggregators (REAG), and 1 demand response aggregator (DRAG). The distribution system market participants' information is in Table. 4.2. The REAG production is considered to be 1 MW with no cost. It is assumed that REAG production is constant.

4.3.1 The Ideal Case

In this section, the simulation results are obtained using the model presented by (4.1) and (4.2). In this case, the DERs participate in the wholesale market directly and submit their offering bids directly to the ISO. This case is ideal since the ISO oversees all the market participants' operation constraints as well as transmission and distribution network constraints. This case is the best case for secure and optimal market participation of the DERs. However, this is not implementable with the current wholesale market structures. The market share of each market participant in this model is given in Table. 4.3.

Table 4.4: ISO market outcomes in the ISO-DSO coordination case

Participant	Share (MW)	Participant	Share (MW)
Gen 1	10	DR 1	10
Gen 2	20	DR 2	20
Gen 3	13.8	DR 3	10
DSO	1.2		

Table 4.5: DSO market outcomes in the ISO-DSO coordination case

Participant	Share (MW)	Participant	Share (MW)
DDGAG 1	0.5	DDGAG 3	1.2
DDGAG 2	1	DDGAG 4	0
DRAG	2.5		

4.3.2 Participation through the DSO

In this case, the bid-in cost function of the DSO is first determined based on the formulation in (4.5). The DSO's total (minimal) operating costs at different output power levels are shown in Fig. 4.2. The breakpoints in Fig. 4.2 are determined by the retail market participants' minimum and maximum output power. The bid-in marginal cost function (price-quantity pairs offered by the DSO to ISO, which is the derivative of the DSO operating cost curve in Fig. 4.2) is in Fig. 4.3. The bid-in marginal cost function starts with the output power of -1.5 MW which means that DSO can consume energy of 1.5 MW since the DRAG has the (consumption) capability of 2.5 MW and the REAG produces 1 MW. The bid-in price of this consumption is 10 $/MWh. This is due to the fact that the cheapest unit's price in the DSO market is 10 $/MWh which means that the wholesale market price should be lower than this value in order for the DSO to buy energy from the wholesale market otherwise it provides that energy from the DDGAG 2. The DSO buys energy with this cost until the capacity of the DDGAG 2 is reached. Then, DDGAG 3, which is the next cheapest generating unit starts to be dispatched. This procedure continues until the last (most expensive) DDGAG is dispatched, which occurs at 3.2 MW. In the end, the DSO sells energy to the wholesale market at the price of 28 $/MWh which is actually the offering price of the DRAG (for energy consumption). This is due to the fact that if the offering price of the wholesale market is greater than 28 $/MWh, the DSO sells the energy to the ISO instead of to the DRAG.

The DSO submits this bid-in marginal cost function to the ISO. Then, ISO runs the wholesale market and determines the wholesale market share of the DSO and other participants. The ISO market outcomes are shown in Table. 4.4. By comparing Tables. 4.3 and 4.4, it is clear the market outcomes for generating units (Gen) and demand response units (DR) directly participating in the ISO market are identical in the ideal case and the ISO-DSO coordination case. The share of the DSO is 1.2 MW. In order to determine the share of the market participants in the DSO market, we need to substitute the parameter in the parametric optimization given in (4.5) which results in a simple optimization problem. The results of this optimization problem are given in Table. 4.5. By comparing Tables. 4.3 and 4.5, it is obvious the market outcomes for various aggregators are identical in the ideal case (when participating in the ISO market directly) and the ISO-DSO

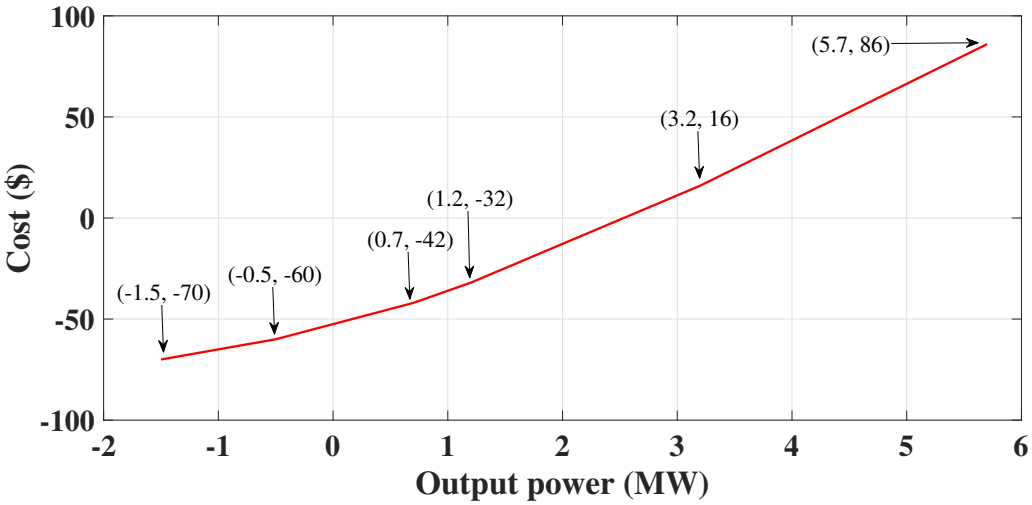

Figure 4.2: DSO total (minimal) operating cost

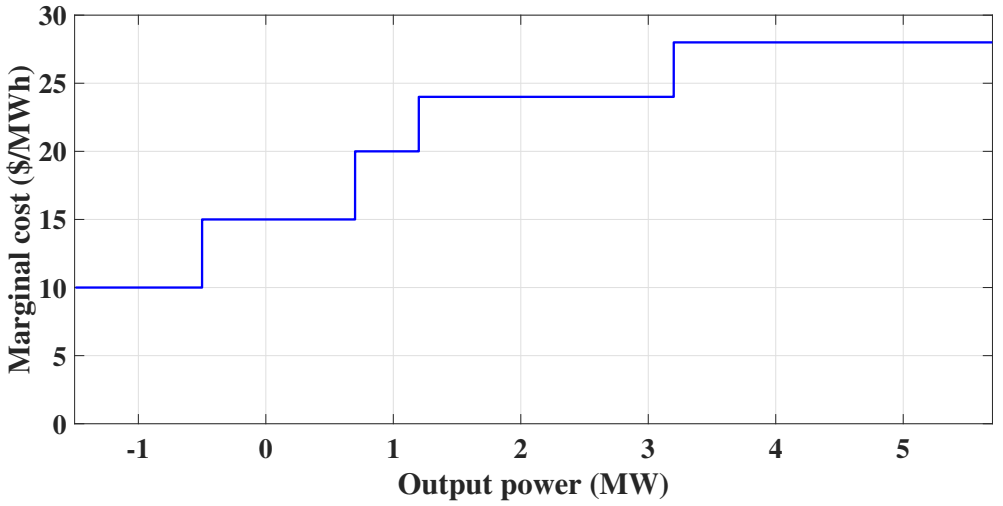

Figure 4.3: DSO marginal cost function (price-quantity pairs) submitted to ISO

coordination case (when participating in the ISO market through the DSO).

4.4 Conclusion

In this chapter, an ISO-DSO market coordination framework is proposed to leverage the wholesale market participation of DER aggregators based on parametric programming. The DSO builds the bid-in cost function based on the DSO market participants' offering prices considering their operational constraints and the physical constraints of the distribution network including the power balance equations and voltage limitation constraints. The simulation results performed on the small system indicate the proposed coordination model will result in the same market outcomes as the ideal case in which the DER aggregators directly participate in the wholesale market.

5. A Two-stage Stochastic Programming DSO Framework for Comprehensive Market Participation of DER Aggregators under Uncertainty

5.1 Introduction

The installed capacity of DERs is increasing, thanks to their low operational costs and growing demand. Being capable of providing fast ramping services, DER aggregators can effectively participate in the wholesale energy and regulation markets. However, uncontrolled participation of DER aggregators may cause security issues to distribution system operations. Hence, there is a need for an entity to enable DER aggregators to participate in the wholesale market and monitor the distribution system for secure and reliable operation.

Many topics have been examined in the context of market participation of DERs. In [80, 81], the concepts of DER aggregator and virtual power plant are introduced to enable DERs for wholesale market participation. A decentralized approach using Dantzig-Wolfe decomposition is presented for DER coordination in [82]. The proposed approach allows households to participate in the electricity market to minimize the total cost. In [83, 84], a microgrid is presented for wholesale market participation. The mentioned works ignore distribution grid operations. Hence, they neglect distribution grid security/reliability constraints which are necessary for DER's market participation. In [85], a biding strategy for market participation of a virtual power plant is proposed considering a demand response market which is considered as a stage between day-ahead and real-time markets. In [86], a bidding strategy is proposed for day-ahead and real-time markets participation of EV aggregators. In [85, 86], in order to consider power balance equations, DC load flow is proposed, which is inappropriate due to high impedances in distribution grids.

Inspired by the smart grid technologies and growing DER installed capacity, the system operators call for a distribution level electricity market in which DERs can easily participate while assuring distribution grid security/reliability. The concept of distribution system operator (DSO) is presented recently in order to integrate DERs while operating the distribution network based on a retail market framework [87–89]. In [87], a DSO is introduced for operating a day-ahead retail market. The distribution locational marginal price (D-LMP) is presented as a method for paying the market participants. However, the distribution network operation and corresponding security constraints are not included in the proposed model. In [88], the authors proposed a two-stage stochastic programming approach for a DSO to operate day-ahead energy and reserve markets. In [89], a distribution market operator (DMO) is proposed which collects offers from microgrids in order to participate in the wholesale market. To represent the relationship between D-LMP and transmission-level LMP, a penalty factor is defined. Both [88] and [89] adopt DC load flow, which is inappropriate for distribution grid modeling.

To the best of our knowledge, the DSO framework for comprehensive market participation of DER aggregators under uncertainty in the retail market as well as wholesale energy and regulation markets has not been studied yet. In this chapter, a two-stage stochastic programming DSO framework is proposed for comprehensive market participation of DER aggregators under uncertainty. Various DER aggregators, including Energy storage aggregators (ESAGs), demand response aggregators (DRAGs), electric vehicle (EV) aggregating charging stations (EVCSs), dispatchable distributed

generation (DDG) aggregators (DDGAGs), and renewable energy aggregators (REAGs), are considered. The proposed DSO optimally coordinates these DER aggregators for their participations in the retail market and wholesale energy/regulation markets, while maintaining distribution grid security. Case studies verify the effectiveness of the proposed DSO framework.

5.2 Two-stage Stochastic DSO Market Formulation

In this chapter, the DSO is defined as an entity which interacts with DER aggregators and end-user customers on one side and trades with the wholesale market on the other side. The DSO collects offers from various types of DER aggregators and runs the retail market as well as coordinates the offers for constructing an aggregated offer for participating in the wholesale energy and regulation markets which is operated by the independent system operator (ISO) whose pay-for-performance regulation market is considered [90, 91].

The wholesale electricity market involves two stages: the day-ahead stage and balancing stage. For instance, California ISO (CAISO), which is adopted here, is a two-settlement market consisting of day-ahead and real-time markets, which is used for adjusting balance between supply and demand [90]. Market participants can participate in the day-ahead market and correct their share by participating in the real-time market in the case that their production or consumption has changed. In practice, usually, there is a difference between the offer of a participant and its production or consumption, especially for renewable energy producers. Hence, participation in the real-time market is necessary for them.

One important characteristic of a DSO is being capable of handling uncertainties in the system operation. An appropriate method for a market operator to cover uncertainties is using two-stage stochastic programming [92]. In this method, in the objective function, expected operational costs, including costs related to the day-ahead operation and costs related to the compensating actions in the real-time, is minimized. In this model, here-and-now variables are decisions related to the day-ahead market and wait-and-see variables are decisions related to the real-time market. Day-ahead market prices usually can be predicted with high accuracy [93]. Hence, sources of uncertainties are inelastic loads, renewable energy aggregator production, and real-time prices. The two-stage stochastic programming introduced in [94] is adopted here.

5.2.1 Objective Function

The DSO minimizes the distribution grid's total operational cost, considering 1) costs of buying/selling energy and selling regulation services to the wholesale energy and regulation markets; 2) costs of paying DER aggregators for their retail market participations. The objective function of the proposed two-stage stochastic programming is given by (4.1).

$$min \sum_{t \in T} [P_t^{sub} \pi_t^e - r_t^{sub,up} \pi_t^{cap,up} - r_t^{sub,dn} \pi_t^{cap,dn} \\ - r_t^{sub,up} S_t^{up} \mu_t^{up} \pi_t^{mil,up} - r_t^{sub,dn} S_t^{dn} \mu_t^{dn} \pi_t^{mil,dn}$$

$$
\begin{aligned}
&+ \sum_{k\in\{K2,K4\}} P_{t,k}\pi^{e}_{t,k} - \sum_{k_3\in K_3} P_{t,k_3}\pi^{e}_{t,k_3} \\
&+ \sum_{k\in K}[r^{up}_{t,k}\pi^{cap,up}_{t,k} + r^{dn}_{t,k}\pi^{cap,dn}_{t,k} \\
&+ r^{up}_{t,k}S^{up}_{t}\mu^{up}_{t}\pi^{mil,up}_{t,k} + r^{dn}_{t,k}S^{dn}_{t}\mu^{dn}_{t}\pi^{mil,dn}_{t,k}] \\
&- \sum_{k_1\in K_1}\sum_{a\in A} P_{a,t,k_1}\pi^{e}_{a,t,k_1} \\
&+ \sum_{w\in W}\Omega_w(P^{sub,b,rl}_{t,w}\pi^{e,b,rl}_{t,w} - P^{sub,s,rl}_{t,w}\pi^{e,s,rl}_{t,w})]
\end{aligned} \tag{5.1}
$$

where t and T are the index and set for the entire operating timespan; k and $K = \{K_1, K_2, K_3, K_4\}$ are the index and set for all DER aggregators; k_1 (K_1), k_2 (K_2), k_3 (K_3), k_4 (K_5), and a (A) are the indices (sets) for all DRAGs, ESAGs, EVCSs, DDGAGs, and demand blocks, respectively; $P^{sub}_{t}, r^{sub,up}_{t}$, and $r^{sub,dn}_{t}$ are the DSO's aggregated quantity offers to the wholesale energy, regulation capacity-up and capacity-down markets, respectively; $\pi^{e}_{t}, \pi^{cap,up}_{t}$ ($\pi^{cap,dn}_{t}$), and $\pi^{mil,up}_{t}$ ($\pi^{mil,dn}_{t}$) are the wholesale energy, regulation capacity-up (capacity-down), and regulation mileage-up (mileage-down) prices, respectively; $P_{t,k}, r^{up}_{t,k}$ and $r^{dn}_{t,k}$ are the energy, regulation capacity-up and capacity-down quantity offers made by DER aggregator k with corresponding prices $\pi^{e}_{t,k}, \pi^{cap,up}_{t,k}, \pi^{cap,dn}_{t,k}$, respectively; μ^{up}_{t} and μ^{dn}_{t} are historical scores for providing regulation mileage-up and mileage-down services; S^{up}_{t} and S^{dn}_{t} are the regulation mileage-up and mileage-down ratios (the expected mileage for $1MW$ provided regulation capacity); P_{a,t,k_1} and π^{e}_{a,t,k_1} are the power consumption and the corresponding energy price at each demand block; Ω_w is the probability of scenario w; $P^{sub,b,rl}_{t,w}$ is amount of power purchased from the wholesale real-time market with corresponding price $\pi^{e,b,rl}_{t,w}$; $P^{sub,s,rl}_{t,w}$ is amount of power sold to the wholesale real-time market with price $\pi^{e,s,rl}_{t,w}$.

In (5.1), the wholesale energy market is modeled as a producer in the DSO, while the wholesale regulation market is modeled as a consumer in the DSO. Therefore, cost terms related to the energy and regulation markets are associated with the positive and negative signs, respectively. The DSO is modeled as a price taker in the wholesale energy and regulation markets.

5.2.2 Constraints for Demand Response Aggregators (DRAGs)

The operating constraints for DRAGs are as follows:

$$\sum_{a\in A} P_{a,t,k_1} - r^{cap,dn}_{t,k_1} \geq 0; \quad \forall t \in T, \forall k_1 \in K_1 \tag{5.2}$$

$$\sum_{a\in A} P_{a,t,k_1} + r^{cap,up}_{t,k_1} \leq \sum_{a\in A} P^{max}_{a,k1}; \quad \forall t \in T, \forall k_1 \in K_1 \tag{5.3}$$

$$0 \leq P_{a,t,k_1} \leq P^{max}_{a,k1}; \quad \forall a \in A, \forall t \in T, \forall k_1 \in K_1 \tag{5.4}$$

$$0 \leq r^{cap,up}_{t,k_1} \leq r^{cap,up,max}_{t,k_1}; \quad \forall t \in T, \forall k_1 \in K_1 \tag{5.5}$$

$$0 \leq r^{cap,dn}_{t,k_1} \leq r^{cap,dn,max}_{t,k_1}; \quad \forall t \in T, \forall k_1 \in K_1 \tag{5.6}$$

where $P^{max}_{a,t,k1}$ is the maximum power consumption at each demand block; $r^{cap,up,max}_{t,k1}$ and $r^{cap,dn,max}_{t,k1}$ are the maximum allowed regulation capacity-up and capacity-down quantity offers, respectively.

Equations (5.2)-(5.3) ensure the total power consumed by the DRAG for buying/selling energy and offering regulation service is less than the maximum power consumption across all demand blocks within the DRAG. Equation (5.4) limits the amount of power offered by each demand block to its maximum value. Equations (5.5)-(5.6) limit the regulation capacity-up and capacity-down quantity offers to their maximum values.

5.2.3 Constraints for Energy Storage Aggregators (ESAGs)

The operating constraints for ESAGs are as follows:

$$\begin{aligned} P_{t,k_2} = E_{t-1,k_2} - E_{t,k_2} + (1/\eta^{di}_{k_2}) r^{cap,up}_{t,k_2} \mu^{up}_t \\ - (\eta^{ch}_{k_2}) r^{cap,dn}_{t,k_2} \mu^{dn}_t; \quad \forall t \in T, \forall k_2 \in K_2 \end{aligned} \tag{5.7}$$

$$P_{t,k_2} = (1/\eta^{di}_{k_2}) P^{di}_{t,k_2} - (\eta^{ch}_{k_2}) P^{ch}_{t,k_2}; \quad \forall t \in T, \forall k_2 \in K_2 \tag{5.8}$$

$$r^{cap,up}_{t,k_2} = r^{cap,up,di}_{t,k_2} + r^{cap,dn,ch}_{t,k_2}; \quad \forall t \in T, \forall k_2 \in K_2 \tag{5.9}$$

$$r^{cap,dn}_{t,k_2} = r^{cap,dn,di}_{t,k_2} + r^{cap,up,ch}_{t,k_2}; \quad \forall t \in T, \forall k_2 \in K_2 \tag{5.10}$$

$$E^{min}_{k_2} \le E_{t,k_2} \le E^{max}_{k_2}; \quad \forall t \in T, \forall k_2 \in K_2 \tag{5.11}$$

$$0 \le P^{di}_{t,k_2} \le b_{t,k_2} DR^{max}_{k_2}; \quad \forall t \in T, \forall k_2 \in K_2 \tag{5.12}$$

$$0 \le r^{cap,up,di}_{t,k_2} \le b_{t,k_2} DR^{max}_{k_2}; \quad \forall t \in T, \forall k_2 \in K_2 \tag{5.13}$$

$$0 \le r^{cap,dn,di}_{t,k_2} \le b_{t,k_2} DR^{max}_{k_2}; \quad \forall t \in T, \forall k_2 \in K_2 \tag{5.14}$$

$$0 \le P^{ch}_{t,k_2} \le (1 - b_{t,k_2}) CR^{max}_{k_2}; \quad \forall t \in T, \forall k_2 \in K_2 \tag{5.15}$$

$$0 \le r^{cap,up,ch}_{t,k_2} \le (1 - b_{t,k_2}) CR^{max}_{k_2}; \forall t \in T, \forall k_2 \in K_2 \tag{5.16}$$

$$0 \le r^{cap,dn,ch}_{t,k_2} \le (1 - b_{t,k_2}) CR^{max}_{k_2}; \forall t \in T, \forall k_2 \in K_2 \tag{5.17}$$

$$\begin{aligned} r^{cap,dn,di}_{t,k_2} \le P^{di}_{t,k_2} \le DR^{max}_{k_2} - r^{cap,up,di}_{t,k_2}; \\ \forall t \in T, \forall k_2 \in K_2 \end{aligned} \tag{5.18}$$

$$\begin{aligned} r^{cap,dn,ch}_{t,k_2} \le P^{ch}_{t,k_2} \le CR^{max}_{k_2} - r^{cap,up,ch}_{t,k_2}; \\ \forall t \in T, \forall k_2 \in K_2 \end{aligned} \tag{5.19}$$

where E_{t,k_2} is the charging level; P^{ch}_{t,k_2} (P^{di}_{t,k_2}) and $\eta^{ch}_{k_2}$ ($\eta^{di}_{k_2}$) are the charging (discharging) power and charging (discharging) efficiencies, respectively; $r^{cap,up,ch}_{t,k_2}$ ($r^{cap,dn,ch}_{t,k_2}$) and $r^{cap,up,di}_{t,k_2}$ ($r^{cap,dn,di}_{t,k_2}$) are the regulation capacity-up (capacity-down) offers in charging and discharging modes, respectively; $CR^{max}_{k_2}$ and $DR^{max}_{k_2}$ are the maximum charging and discharging rates, respectively; b_{t,k_2} is a binary variable indicating the charging ($b_{t,k_2} = 0$) and discharging ($b_{t,k_2} = 1$) modes.

ESAG's power injection is given by (5.7). ESAG's quantity offers for energy and regulation capacity-up/down markets are decomposed into charging and discharging terms by (5.8)-(5.10).

The charge level of ESAGs is limited by (5.11). Equations (5.12)-(5.17) assure that ESAG's offers to the energy and regulation capacity-up/down markets are lower than their maximum values. In equations (5.18)-(5.19), the total power offered by ESAG to the energy and regulation capacity-up/down markets lies within the charging and discharging rates.

5.2.4 Constraints for EV Charging Stations (EVCSs)

EVCSs are modeled as EV charging aggregators and are assumed to have unidirectional power flow. Constraints related to the operation of EVCSs are as follows:

$$0 \leq P_{t,k_3} \leq ER_{k_3}^{max} b_{k_3}; \quad \forall t \in T^{'}, \forall k_3 \in K_3 \tag{5.20}$$

$$0 \leq r_{t,k_3}^{cap,up} \leq ERR_{k_3}^{max} b_{k_3}; \quad \forall t \in T^{'}, \forall k_3 \in K_3 \tag{5.21}$$

$$0 \leq r_{t,k_3}^{cap,dn} \leq ERR_{k_3}^{max} b_{k_3}; \quad \forall t \in T^{'}, \forall k_3 \in K_3 \tag{5.22}$$

$$P_{t,k_3} + r_{t,k_3}^{cap,up} \leq ER_{k_3}^{max}; \quad \forall t \in T^{'}, \forall k_3 \in K_3 \tag{5.23}$$

$$P_{t,k_3} - r_{t,k_3}^{cap,dn} \geq 0; \quad \forall t \in T^{'}, \forall k_3 \in K_3 \tag{5.24}$$

$$\begin{aligned} 0.9CL_{k_3}^{max} b_{k_3} \leq E_{k_3}^{int} b_{k_3} + \sum_{t \in T^{'}} [P_{t,k_3} + r_{t,k_3}^{cap,up} \mu_t^{up} \\ - r_{t,k_3}^{cap,dn} \mu_t^{dn}] \gamma_{k_3}^{ch} \leq CL_{k_3}^{max} b_{k_3}; \ \forall k_3 \in K_3 \end{aligned} \tag{5.25}$$

where $T^{'} \subseteq T$ is the set of hours when EVs are available at the charging station; $ER_{k_3}^{max}$ is the maximum charging rate; $ERR_{k_3}^{max}$ is the maximum allowed regulation capacity offers, $CL_{k_3}^{max}$ is the maximum charge level; $E_{k_3}^{int}$ is the initial charge level; $\gamma_{k_3}^{ch}$ is the charging efficiency; b_{k_3} is a binary variable which enables the DSO not to allocate the minimum power to EVCSs when their offering price is low.

In (5.20)-(5.22), EVCS's offers to the energy and regulation capacity-up/down markets are limited by their corresponding maximum values. In (5.23)-(5.24), the total power offered by EVCS to the energy and regulation capacity-up/down markets lies within the maximum charging rate. Equation (5.25) assures the charge level of EVs is full.

5.2.5 Constraints for Dispatchable DG Aggregators (DDGAGs)

The operating constraints for DDGAGs are as follows:

$$P_{t,k_4} + r_{t,k_4}^{cap,up} \leq P_{k_4}^{max}; \quad \forall t \in T, \forall k_4 \in K_4 \tag{5.26}$$

$$P_{t,k_4} - r_{t,k_4}^{cap,dn} \geq P_{k_4}^{min}; \quad \forall t \in T, \forall k_4 \in K_4 \tag{5.27}$$

$$0 \leq r_{t,k_4}^{cap,up} \leq RU_{k_4}; \quad \forall t \in T, \forall k_4 \in K_4 \tag{5.28}$$

$$0 \leq r_{t,k_4}^{cap,dn} \leq RD_{k_4}; \quad \forall t \in T, \forall k_4 \in K_4 \tag{5.29}$$

where $P_{k_4}^{max}$ and $P_{k_4}^{min}$ are the maximum and minimum power generations, respectively; RU_{k_4} and RD_{k_4} are the maximum ramp-up and ramp-down rates, respectively.

In (5.26)-(5.27), the total power offered by DDGAG to the energy and regulation capacity-up/down markets lie within the DDGAG's maximum and minimum power generations. In (5.28)-(5.29), the DDGAG's regulation capacity-up/down offers are limited by its maximum ramp-up/down rates.

5.2.6 Distribution Power Flow Equations

The linearized power flow equations are adopted from [95]:

$$\begin{aligned}
&\sum_{k_1\in K_1}\sum_{a\in A} H_{n,k_1}P_{a,t,k_1} + \sum_{k_3\in K_3} H_{n,k_3}P_{t,k_3} + P^D_{t,n} \\
&- \sum_{k_2\in K_2} H_{n,k_2}P_{t,k_2} - \sum_{k_4\in K_4} H_{n,k_4}P_{t,k_4} \\
&- \sum_{k_5\in K_5} H_{n,k_5}P_{t,k_5} + H^{sub}_n P^{sub}_t + \sum_{j\in J} Pl_{j,t}A_{j,n} = 0; \\
&\forall t\in T,\ \forall n\in N
\end{aligned} \tag{5.30}$$

$$\begin{aligned}
&\sum_{k_1\in K_1}\sum_{a\in A} H_{n,k_1}P_{a,t,k_1}tan\phi_{k_1} + Q^D_{t,n} \\
&- \sum_{k_4\in K_4} H_{n,k_4}P_{t,k_4}tan\phi_{k_4} \\
&+ H^{sub}_n Q^{sub}_t + \sum_{j\in J} Ql_{j,t}A_{j,n} = 0; \quad \forall t\in T,\ \forall n\in N
\end{aligned} \tag{5.31}$$

$$\begin{aligned}
&V_{m,t} = V_{n,t} - (r_j Pl_{j,t} + x_j Ql_{j,t}); \\
&\forall t\in T,\ \forall m\in N,\ \forall n\in N,\ C(m,n)=1,\ A(j,n)=1
\end{aligned} \tag{5.32}$$

$$V^{min} \le V_{n,t} \le V^{max}; \quad \forall t\in T,\ \forall n\in N \tag{5.33}$$

$$-Pl^{max} \le Pl_{j,t} \le Pl^{max}; \quad \forall t\in T,\ \forall j\in J \tag{5.34}$$

$$-Ql^{max} \le Ql_{j,t} \le Ql^{max}; \quad \forall t\in T,\ \forall j\in J \tag{5.35}$$

$$\begin{aligned}
r^{sub,up}_t &= \sum_{k_2\in K_2} r^{cap,up}_{t,k_2} + \sum_{k_4\in K_4} r^{cap,up}_{t,k_4} \\
&+ \sum_{k_1\in K_1} r^{cap,dn}_{t,k_1} + \sum_{k_3\in K_3} r^{cap,dn}_{t,k_3}; \quad \forall t\in T
\end{aligned} \tag{5.36}$$

$$\begin{aligned}
r^{sub,dn}_t &= \sum_{k_2\in K_2} r^{cap,dn}_{t,k_2} + \sum_{k_4\in K_4} r^{cap,dn}_{t,k_4} \\
&+ \sum_{k_1\in K_1} r^{cap,up}_{t,k_1} + \sum_{k_3\in K_3} r^{cap,up}_{t,k_3}; \quad \forall t\in T
\end{aligned} \tag{5.37}$$

$$\begin{aligned}
&P^D_{t,n,w} - P^D_{t,n} - H^{sub}_n (P^{sub,RT}_{t,w} - P^{sub,b,RT}_{t,w}) \\
&- \sum_{k_5\in K_5} H_{n,k_5}(P_{t,k_5,w} - P_{t,k_5} - P^{spill}_{t,k_5,w}) \\
&+ \sum_{j\in J} Pl_{j,t,w}A_{j,n} - \sum_{j\in J} Pl_{j,t}A_{j,n} = 0; \\
&\forall t\in T,\ \forall n\in N,\ \forall w\in W
\end{aligned} \tag{5.38}$$

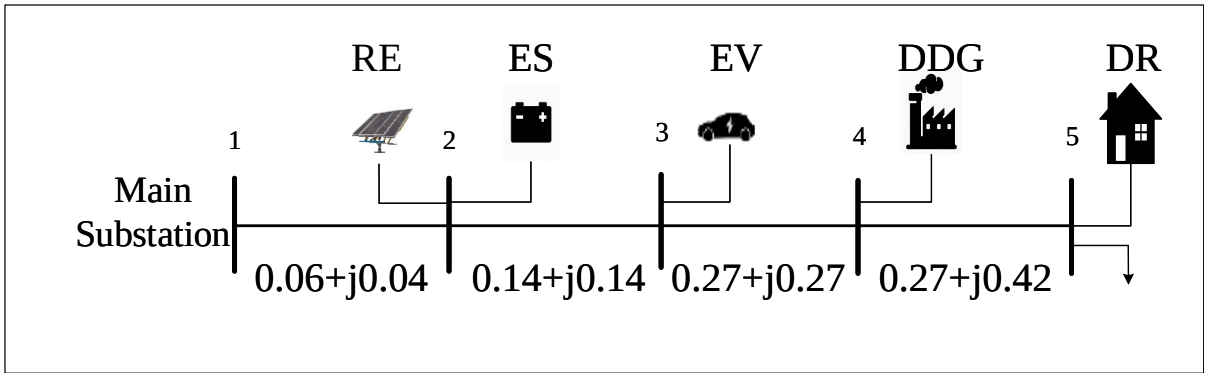

Figure 5.1: The small distribution network for case studies.

$$Q^D_{t,n,w} - Q^D_{t,n} - H^{sub}_n Q^{sub,RT}_{t,w} + \sum_{j\in J} Ql_{j,t,w} A_{j,n} - \sum_{j\in J} Ql_{j,t} A_{j,n} = 0; \quad \forall t \in T,\ \forall n \in N,\ \forall w \in W \tag{5.39}$$

$$V_{m,t,w} - V_{m,t} = V_{n,t,w} - V_{n,t} - (r_j Pl_{j,t,w} - r_j Pl_{j,t} + x_j Ql_{j,t,w} - x_j Ql_{j,t}); \forall t \in T,\ \forall m \in N,\ \forall n \in N,\ C(m,n) = 1,\ A(j,n) = 1,\ \forall w \in W \tag{5.40}$$

$$V^{min} \le V_{n,t,w} \le V^{max}; \quad \forall t \in T,\ \forall n \in N,\ \forall w \in W \tag{5.41}$$

$$-Pl^{max} \le Pl_{j,t,w} \le Pl^{max}; \forall t \in T, \forall j \in J, \forall w \in W \tag{5.42}$$

$$-Ql^{max} \le Ql_{j,t,w} \le Ql^{max}; \forall t \in T, \forall j \in J, \forall w \in W \tag{5.43}$$

$$P^{sub,b,rl}_{t,w}, P^{sub,s,rl}_{t,w} \ge 0; \forall t \in T, \forall w \in W \tag{5.44}$$

where k_5 (K_5) are the indices (sets) for all REAGs; $P^{spill}_{t,k_5,w}$ is the power of REAGs curtailed in each scenario; $H_{n,k}$ is the mapping matrix of DER aggregator k to bus n; $P^D_{t,n}$ and $Q^D_{t,n}$ are the inelastic active and reactive power loads at each node; $Pl_{j,t}$ and $Ql_{j,t}$ are the active and reactive power flow at branch j; $A_{j,n}$ is the incidence matrix of branches and buses; ϕ is the phase angle; $C_{m,n}$ is the connecting nodes matrix.

Equations (5.30)-(5.37) are related to the power flow equations in the day-ahead stage. Specifically, active and reactive power flows are represented by (5.30)-(5.31); voltage drop at each line is represented by (5.32) and is limited by (5.33); active and reactive power limits at each line are represented by (5.34)-(5.35); DSO's aggregated offers for participating in the wholesale energy and regulation capacity-up/down markets are represented by (5.36)-(5.37). Equations (5.38)-(5.43) are related to adjustments in the real-time stage. Specifically, Equations (5.38)-(5.40) are active power, reactive power, and voltage adjustments, respectively; Equations (5.41)-(5.43) ensure that bus voltages, line active and reactive power flows lie within their limits in each scenario, respectively. Equation (5.44) restricts the sign of trading power in the real-time stage.

Table 5.1: REAG's production

Scenario Index	1	2	3	4	5
Production (MW)	1	1.5	3	2	2.5
Probability	0.1	0.1	0.6	0.1	0.1

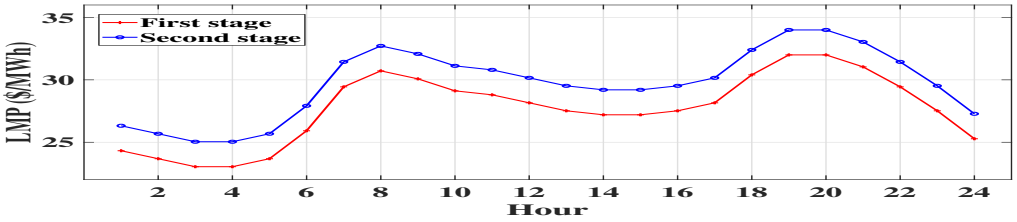

Figure 5.2: First-stage (day-ahead) and second-stage (real-time) LMPs under single source of uncertainty.

5.3 Case Studies

In this section, two-stage stochastic programming introduced in Section 5.2 is used to obtain simulation results. Case studies are performed on the small distribution network in Fig.5.1. The system contains 5 nodes, where $N = \{1, 2, 3, 4, 5\}$; 4 lines, where $J = \{1, 2, 3, 4\}$; a DRAG, where $k_1 = \{1\}$; an ESAG, where $k_2 = \{2\}$; an EVCS, where $k_3 = \{3\}$; a DDGAG, where $k_4 = \{4\}$; a REAG, where $k_5 = \{5\}$, and an inelastic load. The studies are performed over 24 hours, $T = \{1, 2, ..., 24\}$. EVs are available during Hours 16~24, $T' = \{16, 17, ..., 24\}$. Initial charge level of ESAG is $8MW$. The following parameters are assumed: $\eta^{ch}_{k_2} = \eta^{di}_{k_2} = 1$, $E^{min}_{k_2} = 2MW$, $E^{max}_{k_2} = 10MW$, $DR^{max}_{k_2} = CR^{max}_{k_2} = 5MW$, $E^{int}_{k_3} = 2MW$, $ER^{max}_{k_3} = 5MW$, $ERR^{max}_{k_3} = 0.5MW$, $P^{min}_{k_4} = 0$, $P^{max}_{k_4} = 5MW$, $RU_{k_4} = RD_{k_4} = 1MW$, $P^{max}_{a,t,k_1} = 10MW$, $r^{cap,up,max}_{k_1} = r^{cap,dn,max}_{k_1} = 1MW$.

In the deterministic case, inelastic load is considered to be 3 MW at all times and is located at Node 5. Also, the maximum power production of REAG is considered to be 3 MW. Hourly energy prices, capacity up/down prices, and hourly regulation signals are generated by using hourly factors introduced in [96] and are given in [97]. Case studies below focus on uncertainty. Market outcomes in deterministic cases can be found in [97].

Single Source of Uncertainty

In this case, for simplicity, only one source of uncertainty is considered, which is the REAG production given in Table. 5.1. Wholesale real-time market prices are considered to be 2 $\$/MWh$ higher than the corresponding day-ahead market prices. It is assumed the DSO can only buy energy from the real-time market. In two-stage stochastic programming, the first-stage LMP corresponds to the day-ahead market price, which is the dual variable of the power balance equation (5.30). The second-stage LMP corresponds to the real-time price, which is equal to the dual variable of power balance adjustment equation (5.38) divided by probability of occurrence of each scenario. Fig. 5.2

shows the first-stage (day-ahead) and second-stage (real-time) LMPs. Market participants are first settled by day-ahead LMPs. After that, market participants which need real-time compensation due to their uncertainties are settled by real-time LMPs.

Fig. 5.3a shows the REAG's second-stage (real-time) revenue in each scenario. In Scenario 3, REAG's scheduled power in the day-ahead stage is the same as that in the real-time stage. Hence, there is no need for real-time correction. In other scenarios, REAG's scheduled power in the day-ahead stage is higher than that in the real-time stage. This power deficiency should be compensated by purchasing from the wholesale real-time market. As a result, the REAG's second-stage (real-time) revenue is negative, which means it purchases power from the wholesale real-time market. Fig. 5.3b shows the REAG's first-stage (day-ahead) revenue, expected second-stage (real-time) revenue, and expected total revenue.

Multiple Sources of Uncertainties

As mentioned above, there are three sources of uncertainties including REAG production, inelastic load, and real-time prices. Random scenarios can be generated using scenario generation methods based on the probability distribution function. Scenario reduction methods can be applied to reduce computation burden. In this case, for simplicity, normal distribution in Fig. 5.4 with mean value μ and standard deviation σ is considered as the probability distribution of random variables. Seven scenarios from -3σ to 3σ are considered. The mean value of each random variable is assumed to be the same as its value in the deterministic case. The standard deviation σ is considered to be 5%, 15%, and 8% for real-time prices, inelastic load, and REAG production, respectively. The REAG production scenarios are considered to change in the opposite direction of the real-time prices and inelastic load. In the second-stage (real-time), the price of selling energy to the wholesale market is considered to 0.8 of the price of buying energy from it.

Fig. 5.5 shows the first-stage (day-ahead) LMPs and second-stage (real-time) LMPs in different scenarios. LMPs in Scenarios $1\sim3$ equal the real-time prices of selling energy to the wholesale market, since in these scenarios, the demand is lower than the production in the retail market operated by the DSO. However, in Scenarios $5\sim7$ the LMPs equal the real-time prices of buying energy from the wholesale market, since in these scenarios the demand is greater than the production.

Sensitivity Analysis

Sensitivity analysis is carried out on the REAG's revenue with respect to changing the real-time prices in both previous case studies.

Fig. 5.6a shows the changes in REAG's first-stage (day-ahead) revenue, expected second-stage (real-time) revenue, and total revenue with respect to changes in the real-time prices under one source of uncertainty. 25 sensitivity cases are simulated. In each case, the base-case wholesale real-time market prices are multiplied by i, where i varies from 1 to 25. When $i = 1$, the REAG's

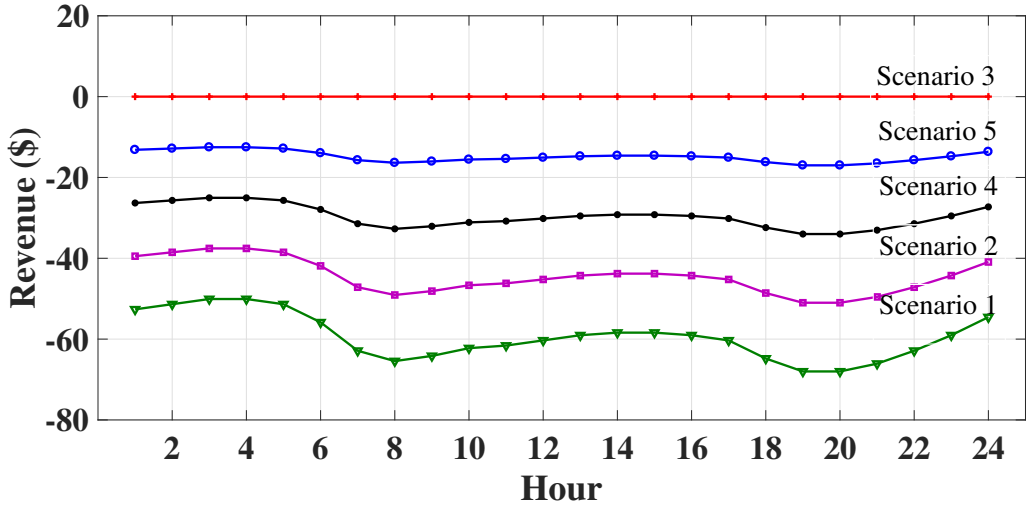

(a)

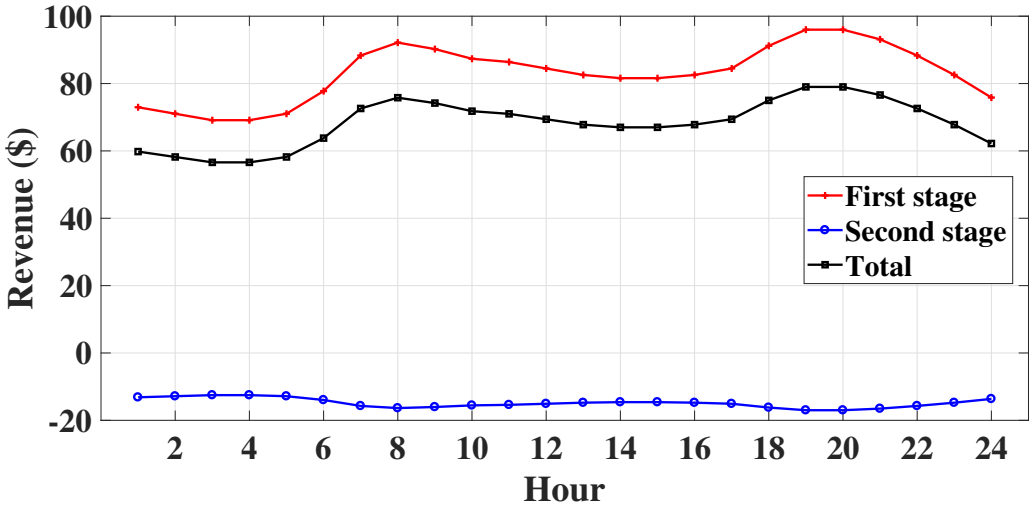

(b)

Figure 5.3: Under single source of uncertainty, (a) REAG's second-stage (real-time) revenue under each scenario; (b) REAG's first-stage (day-ahead) revenue, expected second-stage (real-time) revenue, and total expected revenue.

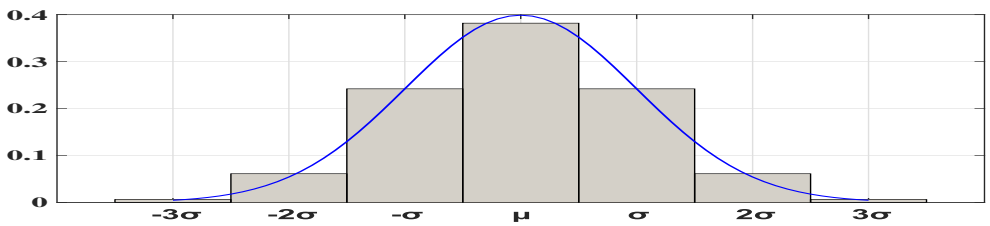

Figure 5.4: Normal distribution used under multiple sources of uncertainties.

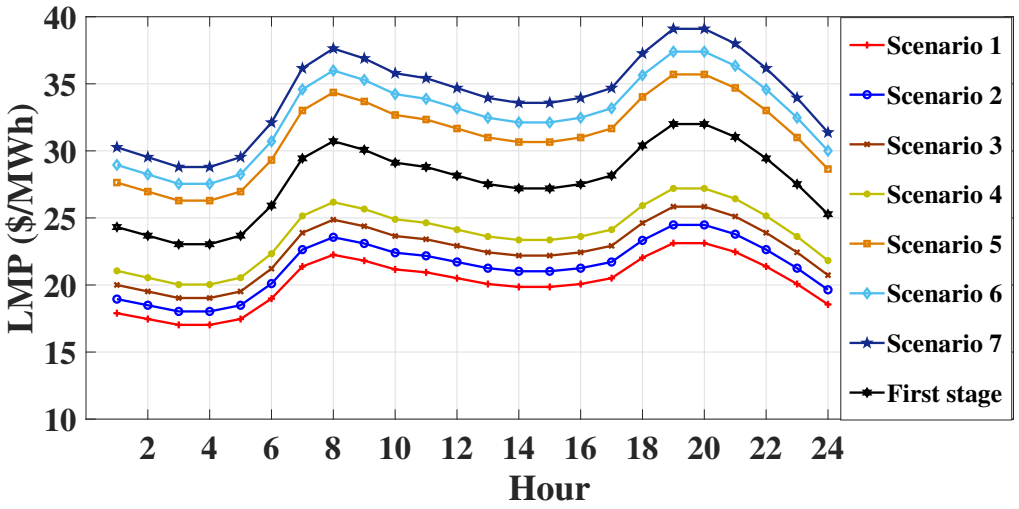

Figure 5.5: Under multiple sources of uncertainties, the REAG's first-stage (day-ahead) LMP and second-stage (real-time) LMPs in different scenarios.

second-stage (real-time) compensation cost is very low. Hence, its first-stage (day-ahead) revenue is high. Also, the REAG's second-stage (real-time) revenue is negative, which indicates the REAG buys power from the real-time market to compensate its power deficiency. Two factors affect the second stage revenues: 1) real-time prices; 2) amount of power deficiency that should be compensated in the real-time market. These two factors are negatively correlated with each other, which means when one factor increases the other factor decreases. The total effect of the two factors depends on the studied sensitivity case. For instance, when $i = 3$, effect of real-time price on second-stage revenue is higher than that of power deficiency, which decreases the second-stage revenue. However, when i increases, the effect of power deficiency grows. Hence, the second-stage revenue becomes zero after $i = 10$. However, the REAG's first-stage revenue and total revenue always decrease when the real-time prices increase.

Fig. 5.6b shows the changes in REAG's first-stage (day-ahead) revenue, expected second-stage (real-time) revenue, and total revenue with respect to changes in the real-time prices under multiple sources of uncertainties. To increase REAG's real-time compensation cost, REAG's real-time selling/purchasing prices are multiplied/divided by i, where i varies from 1 to 25. When i is small, the real-time compensation cost is low. Hence, the DSO schedules the REAG production at its mean value and covers the variations of inelastic load and REAG production by trading with the wholesale market. When i increases, the real-time compensation cost becomes expensive. As a result, the DSO schedules the REAG production at a lower level to avoid trading with the wholesale market and compensate inelastic load variation by REAG production. This causes the REAG's expected second-stage (real-time) revenue to increase when i becomes greater. After $i = 14$, the DSO schedules the minimum production for REAG, which causes the curves to become constant.

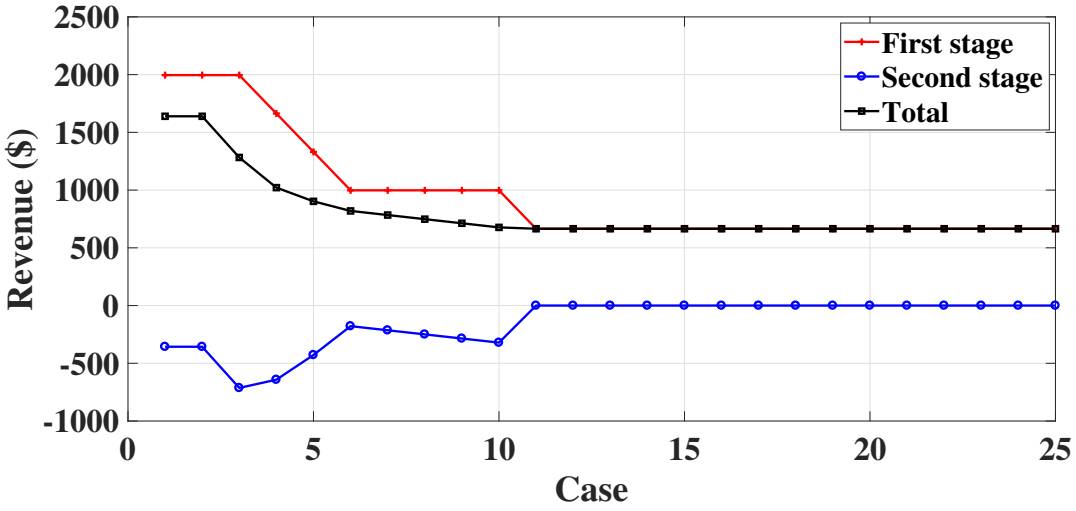

(a)

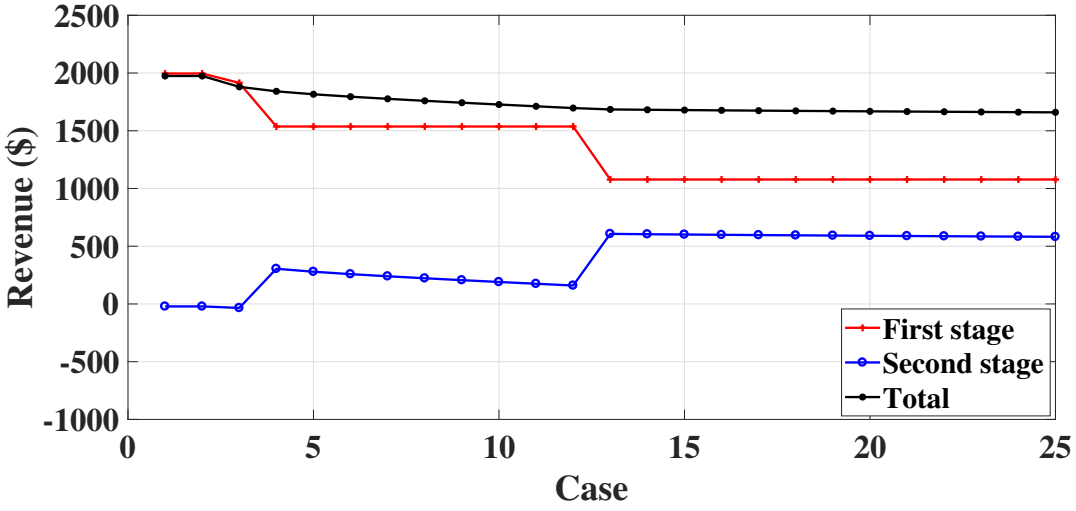

(b)

Figure 5.6: Changes in REAG's first-stage (day-ahead) revenue, expected second-stage (real-time) revenue, and total revenue with respect to changes in the real time prices under (a) one source of uncertainty; (b) multiple sources of uncertainties.

5.4 Conclusion

This chapter proposes a two-stage stochastic programming DSO framework for coordination of DER aggregators to participate in the retail market as well as wholesale energy and regulation markets. Various kinds of DER aggregators are modeled in the proposed DSO framework. Case studies carried out on a small distribution network show key factors between the first-stage (day-ahead) and second-stage (real-time) LMPs. The REAG participates in day-ahead and real-time markets with uncertainties. Sensitivity analysis shows as the real-time price increases, the DSO schedules less power production to REAG as an uncertain market participant.

6. DER Coordination for Frequency Regulation Service Provision

This chapter summarizes the work outlined in **Task 3.2** and **Task 3.3** of the proposal. As part of the final report, we review the distributed energy resource (DER) coordination problem within small power systems referred to as microgrids. We describe the centralized as well as a distributed solution methodology and its implementation that enables microgrids to coordinate multiple DERs in order to provide frequency regulation services to the bulk grid. We also provide details on the controller hardware-in-the-loop (CHIL) testbed that is used extensively to test the centralized as well as the distributed approach. We finally provide results that we obtained as part of the testing of the two approaches for coordinating the DERs in the ***Banshee*** distribution system operated as a microgrid [98]. In the appendix, we provide a review of the so called ratio consensus algorithm that is used as the basis for the distributed DER coordination within a microgrid.

6.1 Introduction

The DER coordination probles also referred to as the provision of regulation services problem is described in detail in [99] and [100]. Here we summarize the problem formulation and its control implementation both in a centralized and a distributed fashion. In terms of provision of regulation services, we focus on the frequency regulation ancillary service program offered by PJM, which is a regional transmission organization (RTO) in the United States that coordinates the movement of wholesale electricity in all or parts of 13 states and the District of Columbia. It operates an ancillary services market with frequency regulation being one such service. The participating entities in this service include large enough DERs, aggregations of DERs, or microgrid deployments. The control objective for the participating entities is to coordinate and control the real power injections of the controllable DERs within their jurisdiction such that the net active power injection into the bulk grid tracks a frequency regulation signal sent from the PJM RTO.

PJM, in its real-time regulation market, provides the participating entities with two different regulation signals, *RegA* and *RegD*. RegA signal is the slower signal that is meant to recover larger, longer fluctuations in system condition whereas RegD signal is the fast, dynamic signal that requires regulation units to respond almost instantaneously. In the control function described here, we focus on the frequency regulation service in response to a PJM RegD signal [101], as it is better suited to microgrid applications which are typically comprised of DERs that can respond almost instantaneously. In microgrid applications, the controllable DERs are adjusted such that the change in active power flow between the microgrid and the bulk grid at the point of common coupling (PCC) bus is in accordance with the RegD signal requirements. The DERs are adjusted according to their participation factors that can capture their respective capacity limits or can capture their cost curves.

6.2 DER Coordination Problem

To formulate the provision of regulation services problem, we first describe a general AC microgrid network. Afterwards, we provide details on the centralized as well as the distributed implementation of the solution.

6.2.1 Microgrid Network Preliminaries

We consider a balanced three-phase ac microgrid. We assume that all loads are operated as constant power type or in the so-called PQ mode. We also assume that the microgrid network is comprised of short transmission lines. Thus, the lumped-parameter circuit describing the terminal behavior of the line connecting bus i and bus j reduces to the series element of the Π-equivalent circuit model. We also assume that all the quantities are in per-unit.

For an $(n+1)$-bus microgrid, let $\mathcal{G}_p = (\mathcal{V}_p, \mathcal{E}_p)$ be a directed simple graph representing the interconnections between buses. The vertex or bus set, $\mathcal{V}_p$, is defined to be $\mathcal{V}_p := \{0, 1, ..., n\} = \{0\} \cup \mathcal{V}_p^{(g)} \cup \mathcal{V}_p^{(\ell)}$, $\mathcal{V}_p^{(g)} \cap \mathcal{V}_p^{(\ell)} = \emptyset$, where bus 0 is assigned to the point of common coupling (PCC) bus, and $\mathcal{V}_p^{(g)}$ and $\mathcal{V}_p^{(\ell)}$ denote generator and load bus sets, respectively. Each bus has only a generator or load connected to it, but not both, and without loss of generality, we partition the bus set such that $\mathcal{V}_p^{(g)} := \{1, 2, ..., m\}$, $\mathcal{V}_p^{(\ell)} := \{m+1, m+2, ..., n\}$. The edge or branch set, $\mathcal{E}_p$, is defined to be $\mathcal{E}_p \subseteq \{(i, j) : i \neq j, i, j \in \mathcal{V}_p\}$, where the edge $(i, j) \in \mathcal{E}_p$ if buses i and j, $i \neq j$, are connected electrically with the flow of power from bus i to bus j assigned to be positive. Let $\mathcal{N}_p(i) := \{j \in \mathcal{V}_p : (i, j) \in \mathcal{E}_p\}$, and define $\mathcal{D}_p(i) = |\mathcal{N}_p(i)|$.

Let $v_i(t)$ and $\theta_i(t)$ respectively denote the magnitude and the phase of the voltage phasor associated with bus i at time t, relative to a reference frame that rotates at some nominal frequency, e.g., 60 Hz. The net active and reactive power injection at bus i, respectively denoted by $p_i(t)$ and $q_i(t)$, are given by

$$p_i(t) := G_{ii} v_i(t)^2 + v_i(t) \sum_{j \in \mathcal{N}_p(i)} v_j(t) \Big(G_{ij} \cos\big(\theta_i(t) - \theta_j(t)\big) + B_{ij} \sin\big(\theta_i(t) - \theta_j(t)\big) \Big), \tag{6.1}$$

$$q_i(t) := -B_{ii} v_i(t)^2 + v_i(t) \sum_{j \in \mathcal{N}_p(i)} v_j(t) \Big(G_{ij} \sin\big(\theta_i(t) - \theta_j(t)\big) - B_{ij} \cos\big(\theta_i(t) - \theta_j(t)\big) \Big), \tag{6.2}$$

where $-G_{ij}$ and $-B_{ij}$ represent the conductance and susceptance of the lines connecting buses i and j, respectively, and $G_{ii} := -\sum_{j \in \mathcal{N}_p(i)} G_{ij}$, $B_{ii} := -\sum_{j \in \mathcal{N}_p(i)} B_{ij}$. Given the above definitions, we now describe the centralized as well as the distributed frequency regulation service implementation.

6.2.2 Centralized Frequency Regulation Service Implementation

We start by assuming that the time is discretized into fixed-time intervals, referred to as round, and indexed by $r = 0, 1, 2...$, and variables of interest, e.g., voltages, phase angles, active power injections etc., are indexed accordingly, e.g., $v_i[r]$, $\theta_i[r]$, and $p_i[r]$, respectively denote the magnitude, phase angle of the voltage phasor at round r, and active power injection at bus i at round

r. The processor that implements the centralized regulation service control function takes as inputs the regulation signal value, denoted by $\delta^p[r]$, active power set point at each controllable DER bus, $u_i^p[r],\ i \in \mathcal{V}_p^{(g)}$, and tie-line active power measurement, $p_0[r]$. Let $\Delta u_0^p[r] = \delta^p[r] - p_0[r]$ represent the mismatch between the tie-line active power measurement and the regulation signal in round r. Then, the controller updates the set-point for each DER at bus $i \in \mathcal{V}_p^{(g)}$ according to:

$$u_i^p[r+1] = u_i^p[r] + \gamma_i \Delta u_0^p[r], \tag{6.3}$$

where γ_i represents the participation factor for the DER at bus $i \in \mathcal{V}_p^{(g)}$.

6.2.3 Distributed Frequency Regulation Service Implementation

In our implementation of the distributed frequency regulation service, each DER adjusts its active power set-point according to (6.3), but in order to do so, the DERs will compute the $\Delta u_i^0[r]$, in a distributed fashion. To this end, we assume that the microgrid is endowed with multiple, geographically dispersed, computing devices referred to as distributed control nodes. Each distributed control node can acquire information locally from its associated asset, e.g., for each $i \in \mathcal{V}_p^{(g)}$, a control node has access to the corresponding DER participation factor, γ_i, and DER active power set point $u_i^p[r]$. In addition, the control nodes can exchange information among their neighboring control nodes. We also assume that there is a control node at the PCC bus. We assume that this node has access to the tie-line active power measurement, $p_0[r]$, and it also receives the regulations signal, $\delta^p[r]$, from an aggregator or the ISO itself. This allows the PCC bus control node to compute the mismatch, $\Delta u_0^p[r]$, between the tie-line active power measurement and the regulation signal in round r. The control nodes along with the PCC bus control node can then use the information they acquire locally, e.g., from measurements, and via exchanges with their neighbors, as inputs to the ratio consensus algorithm. Through the ratio-consensus algorithm, each control node learns the mismatch value, $\Delta u_0^p[r]$ in a distributed manner. Once $\Delta u_0^p[r]$ is computed, its value is used by each DER control node to adjust the DER active power set-points.

We now describe how the ratio-consensus algorithm is initialized to achieve the distributed computation of the tie-line mismatch from the desired regulation signal. The detailed review of the ratio consensus algorithm is provided in the appendix. Let the PCC control node receive the regulation signal $\delta^p[r]$. In order for each control node to learn $\Delta u_0^p[r]$ in a distributed fashion, for $i \in \{0\} \cup \mathcal{V}_p^{(g)}$, we set:

$$y_i[0] = \begin{cases} \Delta u_0^p[r], & \text{if } i = 0 \\ 0, & \text{if } i \in \mathcal{V}_p^{(g)}, \end{cases} \tag{6.4}$$

$$z_i[0] = \begin{cases} 1, & \text{if } i = 0 \\ 0, & \text{if } i \in \mathcal{V}_p^{(g)}. \end{cases} \tag{6.5}$$

Then, according to the ratio consensus algorithm, we have that

$$\lim_{k \to \infty} \frac{y_i[k]}{z_i[k]} = \Delta u_0^p[r].$$

Then $\Delta u_0^p[r] = \lim_{k\to\infty} \frac{y_i[k]}{z_i[k]}$. This can then be used in (6.3) to adjust the setpoints of each DER at bus $i \in \mathcal{V}_p^{(g)}$.

6.3 C-HIL Testbed

Over the last few years, we have developed a C-HIL testbed to carry out the verification and validations tasks of the different microgrid control functions. This section describes in detail the general framework and underlying infrastructure of our C-HIL testbed, which comprises a physical layer and a cyber layer. We provide an overview of the testbed and explain the functions of both layers. We also describe the hardware and software that constitutes each layer of the C-HIL testbed.

6.3.1 Overview

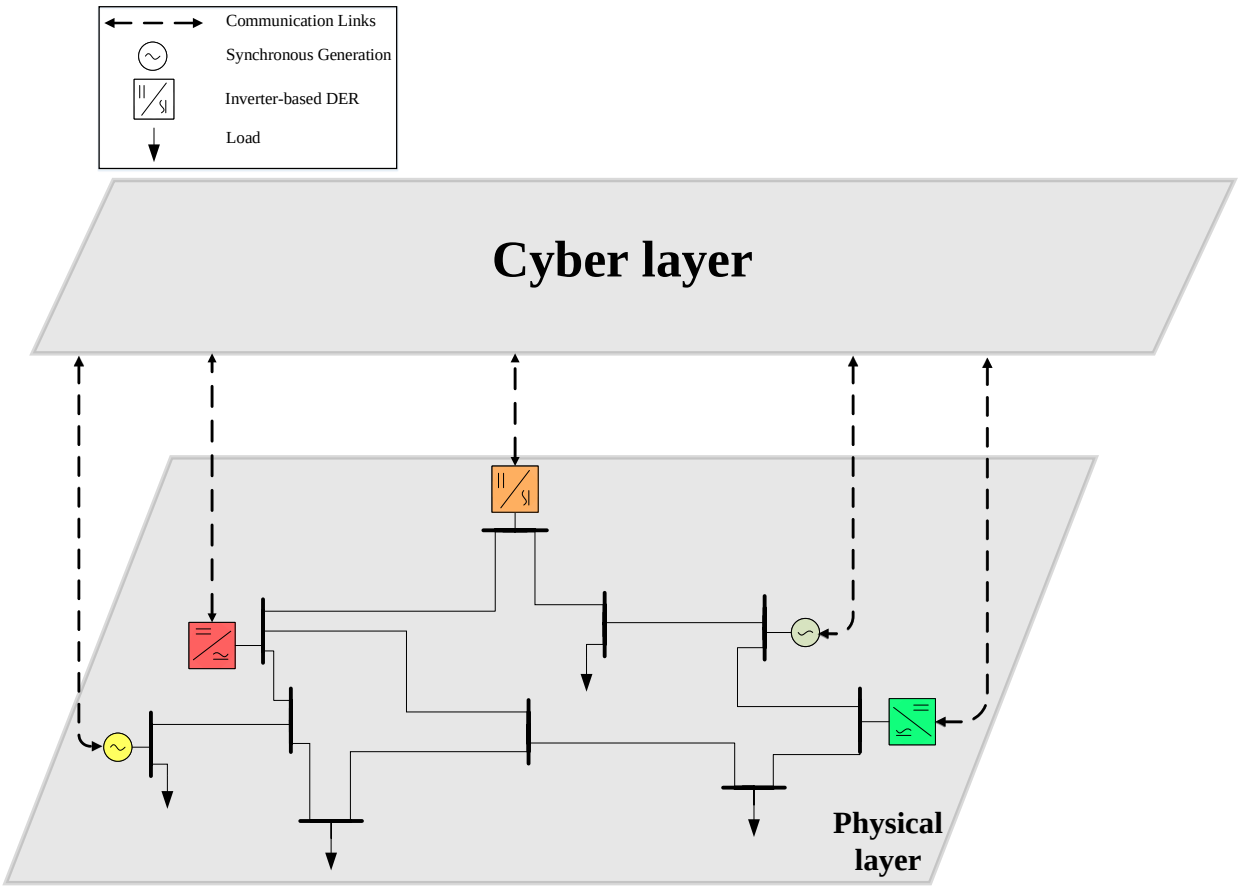

Figure 6.1: Typical microgrid architecture

Figure 6.1 depicts the general architecture of a microgrid, where the electrical network, loads and generators form what we refer to as the physical layer of the microgrid, and a second layer, which we refer to as the cyber layer, that can be conceptually thought of as the collection of components and entities that ensure coordination and control of the resources in the physical layer. Similar to the architecture in Figure 6.1, our C-HIL testbed comprises two layers, which we also refer to as

the physical and cyber layers. In this respect, the physical layer comprises equipment that is used to emulate power devices such as DERs and their associated lower-level controllers, loads, and the electrical power network in a real-time fashion.

Power system dynamic phenomena span a wide range of time scales varying from microseconds to minutes. The phenomena taking place in the slower time scales (typically occurring in minutes) are usually treated as steady state, and emulating such phenomena using a computer simulation, e.g., in MATLAB/Simulink, provides relatively accurate results. While MATLAB/Simulink and other analogous software packages can carry out detailed power system simulations at small time-steps, it is devoid of the capability to capture and emulate real-time behavior. More specifically, it could take hours to simulate a few seconds of detailed power system operations. The need to emulate real-time behavior of power system operations makes the real-time simulator a key component of the testbed physical layer; thus, in our testbed, DERs, loads, and the electrical power network are modeled using a real-time simulator.

The cyber layer of the C-HIL testbed comprises the components used to emulate operations of the communication, coordination, and control infrastructure of a microgrid. In particular, the cyber layer is made up of the equipment that emulates different decision-making architectures—centralized, decentralized, and distributed. The cyber layer also includes equipment that emulates the topology and operations of a microgrid's underlying communication infrastructure. The cyber layer components monitor the states of the microgrid, e.g., voltages, frequency, and active and reactive power injections, and use this information to initiate appropriate coordination and control actions within the physical layer. Such a closed-loop operation between the physical and cyber layer emulates the real-time behavior of a microgrid and allows for high-fidelity testing of the various control architectures.

6.3.2 C-HIL Testbed Physical-Layer Infrastructure

The physical layer in our testbed is composed of Typhoon HIL real-time simulator. The Illinois C-HIL testbed is currently equipped with five ultra-high-fidelity real-time simulation hardware devices: one Typhoon HIL 402 and four Typhoon HIL 603s (see Figure 6.2). By allowing real-time simulation step sizes as low as 0.5 μs and PWM sampling of 20 ns, and implementing very detailed models of system components, these devices can accurately emulate the effects of switching transients and electromagnetic transients on a microgrid. We have also implemented reduced-order models of the DERs, loads, and the network on the Typhoon HIL devices to reduce the modeling complexity and, as a result, lower the computational cost of emulating a large system.

Figure 6.2: Typhoon 402 & 603

6.3.3 C-HIL Testbed Cyber-Layer Infrastructure

The cyber layer in our testbed is composed of microcontroller-based lower level controllers and control nodes that allow the emulation of centralized, decentralized, and distributed control architectures. In addition, the cyber layer includes the communication infrastructure needed for secure monitoring of the system emulated in the physical layer, and the relaying of control commands to individual DERs.

Lower-level Control Platform

Based on the state of operations within the emulated system, the cyber layer sends out the appropriate control actions for the controllable DERs and loads in the physical layer. These control actions are carried out by the lower-level controllers. The Typhoon HIL real-time emulator can be used to model the lower-level controllers for the generator sources. However, our C-HIL testbed is equipped with multiple Texas Instruments MSP-EXP432e401y Ethernet boards for implementation of lower-level DER control schemes. Such schemes include governor control, frequency droop control, voltage droop control, and virtual oscillator control. The C-HIL testbed consists of hundred such devices stacked up in ten metal cabinets (see Figure 6.3).

Figure 6.3: A single TI MSP-EXP432e401y (left), back view of a cabinet with ten such controllers (middle), and front view of a cabinet with ten such controllers (right)

Control Nodes

The decision-making entities in the cyber layer are referred to as control nodes. Depending on the type of control architecture—centralized, decentralized or distributed—the appropriate control node is utilized. For the emulation of a centralized control architecture, the cyber layer makes use of a single National Instruments' (NI's) Compact RIO (cRIO) 9068 as the sole control node (see Figure 6.4). The cRIO 9068 controller is an industrial-grade real-time microcontroller which provides an easy way to build and implement centralized control architectures using the NI Labview system design software. For implementing a distributed decision-making architecture, the cyber layer utilizes multiple Arduino-based hardware devices as control nodes. These Arduino-based control nodes implement the necessary algorithms and protocols needed to realize the control architecture.

Figure 6.4: NI cRIO 9068 device

Communication

To implement the coordination and control tasks effectively, the testbed makes use of several different bidirectional communication links between the various components. The Typhoon HIL simulator provides several options for communication with external devices. Out of these options, we employ the modbus TCP/IP protocol as it is one of the industry standards for communication. The cRIO 9068 controller also provides the capabilities to implement modbus TCP/IP protocol which allows us to interface the controller with the lower-level TI controllers and the Typhoon HIL devices. Similar to the Typhon devices and cRIO controller's communication, the TI MSP-EXP432e401y also makes use of its ethernet board to allow the implementation of the modbus TCP/IP protocol and setup communication links with the devices in the testbed. To set up the TCP/IP private network in the testbed, we make use of an ethernet switch; this infrastructure provides the capabilities to set up a centralized control architecture in the testbed.

A similar setup is used when using multiple Arduino-based control nodes. The control nodes implement two standard protocols to facilitate communication in this setup: (1) Zigbee protocol for peer-to-peer wireless communication among control nodes, and (2) Modbus TCP/IP protocol for Ethernet communication between each control node and the lower-level controllers, and between each control node and the physical layer emulator, i.e., the Typhoon HIL device. The control nodes employ the Zigbee protocol and communicate among themselves wirelessly via a MaxStream XB24-DMCIT-250 revB XBee wireless module that is interfaced to an Arduino Due. To employ the modbus TCP/IP protocol for establishing bidirectional communication link with the lower-level controllers, as well as with appropriate physical layer emulator, the control nodes use the Ethernet shield model W5100 that is also interfaced with the Arduino Due device. A laboratory prototype of the Arduino Due based control node is shown in Figure 6.5. An overview of the C-HIL testbed architecture described above is provided in Figure 6.6.

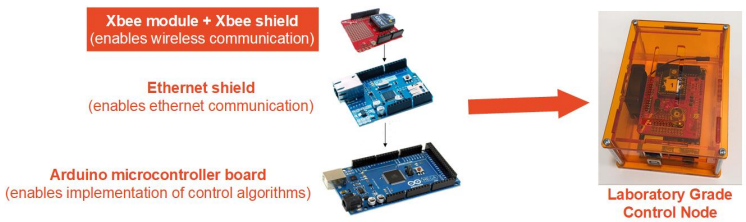

Figure 6.5: Laboratory Grade Control Node Prototype

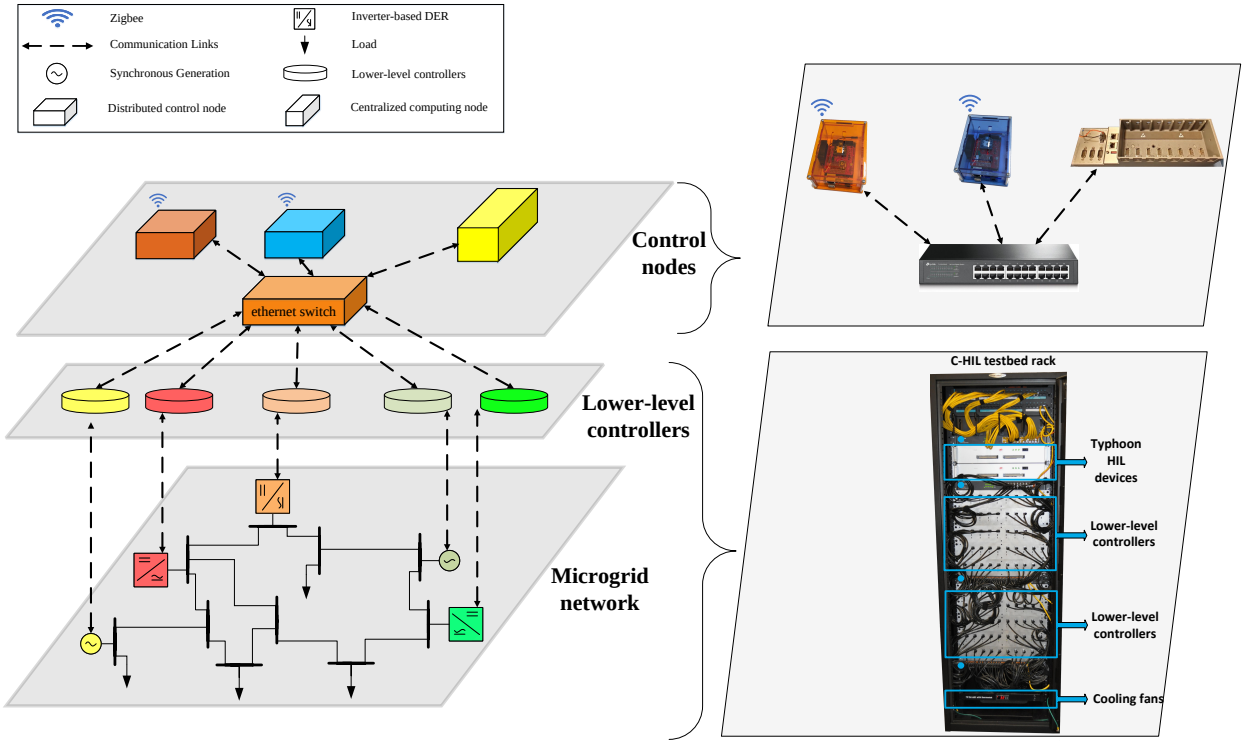

Figure 6.6: Illinois cHIL Testbed

6.3.4 Control Architecture Implementation on the Illinois C-HIL Testbed

In terms of implementation of a centralized control architecture on the Illinois C-HIL testbed, we make use of the NI cRIO 9068 as described earlier. The DERs, loads and the microgrid network are emulated in the Typhoon HIL device. We use the Modubus TCP/IP protocol to set up a bidirectional communication interface between the cRIO 9068 and the Typhoon HIL device. The cRIO 9068 device acquires the operating points of the assets emulated in the Typhoon HIL device and uses that information along with the control objectives to calculate modified operating points for the controllable assets. To close the control loop, the cRIO sends these new operating points to the controllable assets emulated in the Typhoon HIL device. The C-HIL setup for testing the centralized control architecture is shown in Figure 6.7 (right). For the experiments where we use the lower-level controllers to implement the lower-level DER control schemes, a unidirectional communication link between the cRIO and the Typhoon HIL device, cRIO and lower-level controller, and lower level controllers and the Typhoon HIL device is sufficient for closed-loop operation.

In terms of implementation of a distributed control architecture on the C-HIL testbed, multiple Arduino Due microcontrollers serve as the distributed control nodes. As mentioned before, each device is interfaced with an ethernet shield which allows the control nodes to communicate with the Typhoon HIL device via the Modbus TCP/IP protocol so as to enable the monitoring and control of the emulated microgrid assets. In addition, each control node also has a wireless module which allows the control nodes to communicate and exchange information with their neighbors.

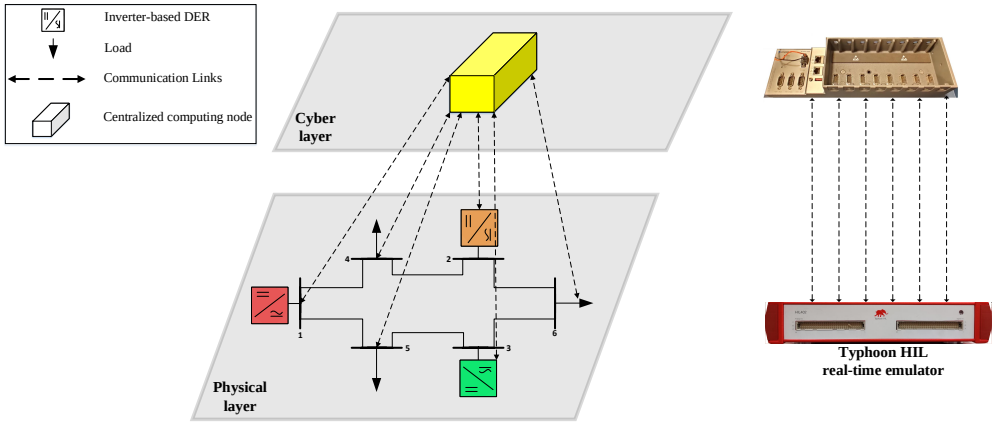

Figure 6.7: a) A centralized computing node connected to DERs and controllable loads and b) the associated C-HIL setup

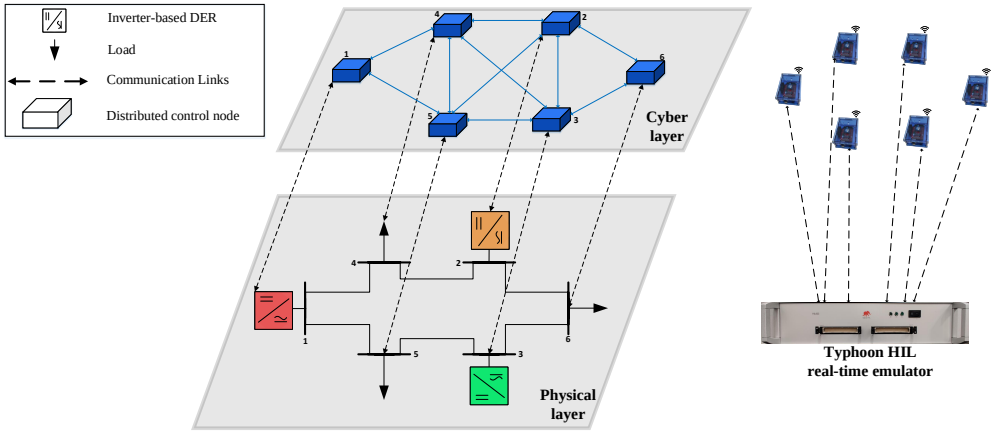

Figure 6.8: a) Six distributed control nodes connected to DERs and controllable loads and b) the associated C-HIL setup

The C-HIL setup for the distributed architecture is shown in Figure 6.8 (right). Each control node implements several distributed algorithms, which enable the distributed implementation of different control functions. In particular, the ratio-consensus algorithm serves as the base for implementing a wide range of control functions, including secondary frequency control, secondary voltage control, and provision of ancillary services to the bulk grid. The speed at which the distributed architecture carries out the specific control function depends on how fast the distributed algorithms converge. The rate of convergence heavily depends on the connectivity of the communication network. For example, for the case where each distributed control node is directly connected to every other control node in the system, the convergence speed is the same as that achieved with the centralized scheme. Each control node uses the distributed algorithms with the information they acquire locally and from neighboring exchanges to calculate new set points for the controllable assets of the microgrid. To close the loop, they send out the new set points to the DERs and controllable loads within a microgrid emulated in the Typhoon device.

6.4 C-HIL Testing of the DER Coordination Problem

In this section, we provide the results we obtained as part of the C-HIL testing of the centralized as well as the distributed approach to DER coordination in the Banshee system. We start by providing details on the implementation of the Banshee distribution network. Afterwards, we provide details on the centralized as well as the distributed test setup before providing the test results for the two approaches.

6.4.1 Banshee Distribution Network and its Implementation

For the testing activities, we make use of the Illinois CHIL testbed (described in detail in section 6.3), and a realistic power distribution network operated as a microgrid. This distribution network, known as the Banshee system [98], resembles emerging microgrids around the world, making it a reliable test system to evaluate the performance. We make use of the Typhoon HIL real-time emulators that are used to simulate the Banshee distribution network and the DERs and loads connected to it (see Fig. 6.9). The Banshee system is emulated on four Typhoon HIL 603 devices connected with each other using the serial connectors. The Banshee system under test contains four DERs as follows: DER 1(4 MVA capacity) in feeder 1, DER 2 and 3 (3 MVA capacity each) in feeder 2, and DER 4 (3.5 MVA capacity) in feeder 3 of the Banshee microgrid respectively.

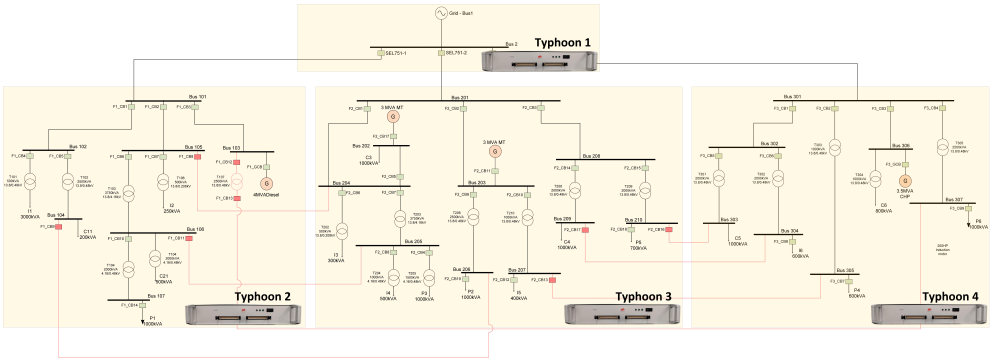

Figure 6.9: Banshee distribution network emulation of Typhoon HIL 603

Out of the four Typhoon HIL devices in the test setup, the grid-side source and its impedance are emulated on a single typhoon HIL 603 device, while each feeder is emulated on the other three devices, respectively. Such partioning is made possible by the use of the so called device coupling elements. In addition to the device coupling elements, we also make use of the core coupling elements. Each Typhoon device has a limited number of cores. Optimized placement of core coupling elements allows us to ensure no core within a Typhoon device is overloaded and the processing stability of the Banshee network under testing is not jeopardized. Via the means of images, we next describe the implementation of the Banshee network and the DERs connected in it. Figure 6.10 describes the Banshee distribution network's schematic with the different device and core coupling elements placed. Figure 6.11 zooms in on the device coupling element and two core coupling elements placed in feeder 3 of the Banshee distribution network. Figure 6.12 describes the location in the network of the four DERs.

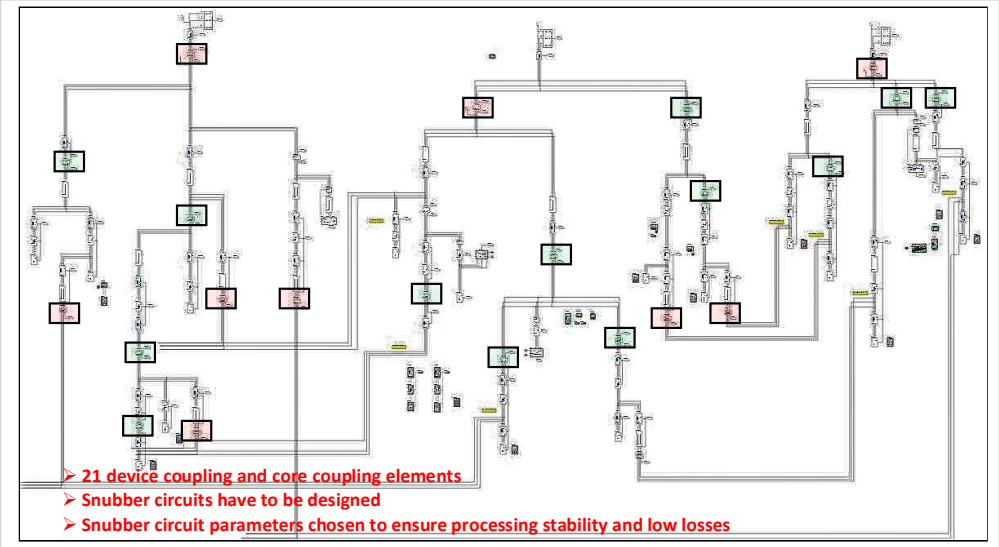

Figure 6.10: Banshee network with the device coupling and core coupling elements

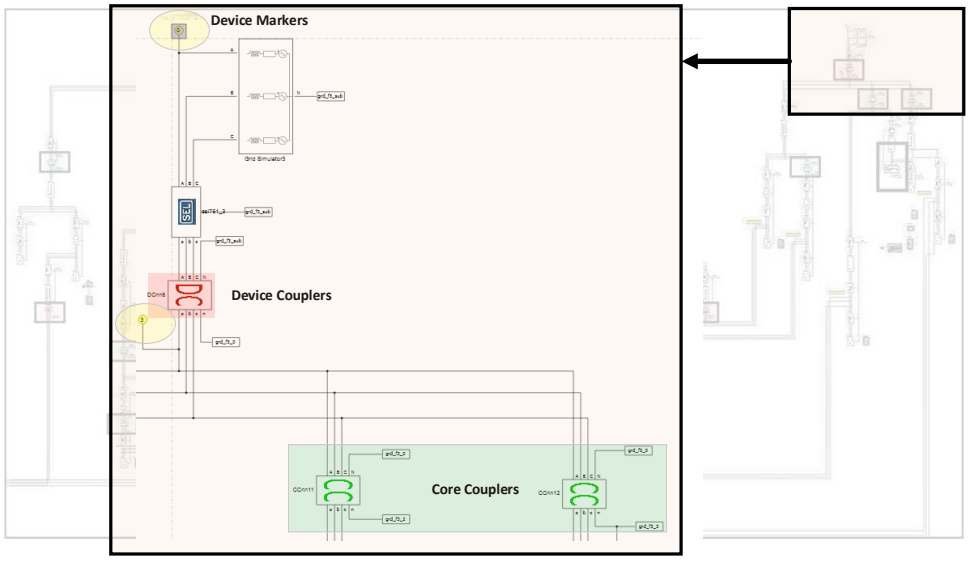

Figure 6.11: Device coupling and core coupling elements in feeder 3

6.4.2 Centralized and Distributed Test Setup

In Fig. 6.13, we provide a C-HIL test setup framework with a single centralized computing node as part of the cyber layer. The centralized computing device monitors and controls each DER modeled as part of Banshee network in the Typhoon HIL emulator as described in the physical layer of the test setup framework.

In Fig. 6.14, we provide a C-HIL test setup framework with the different distributed control nodes exchanging information using a communication graph described in the cyber layer. The control nodes with which a particular control node can exchange information with are referred to as the

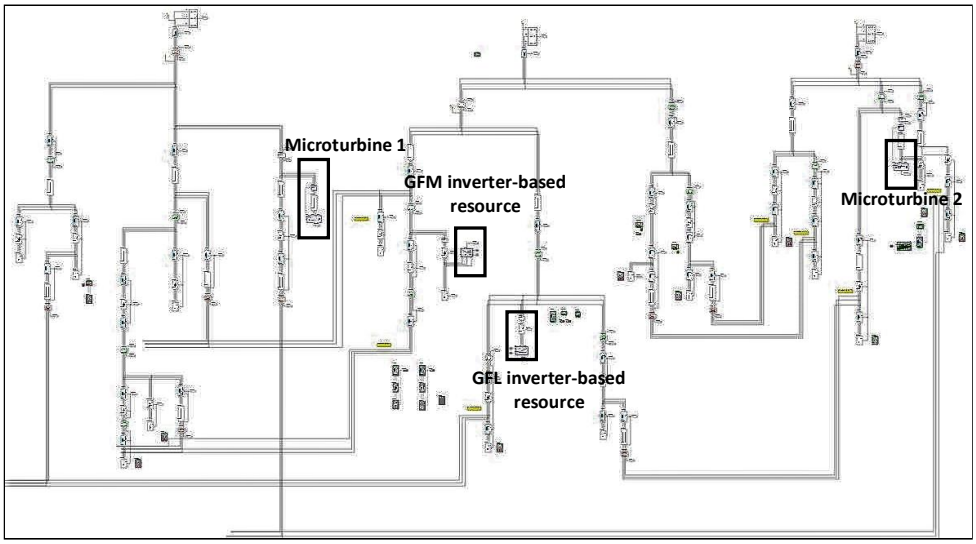

Figure 6.12: DERs in Banshee distribution network

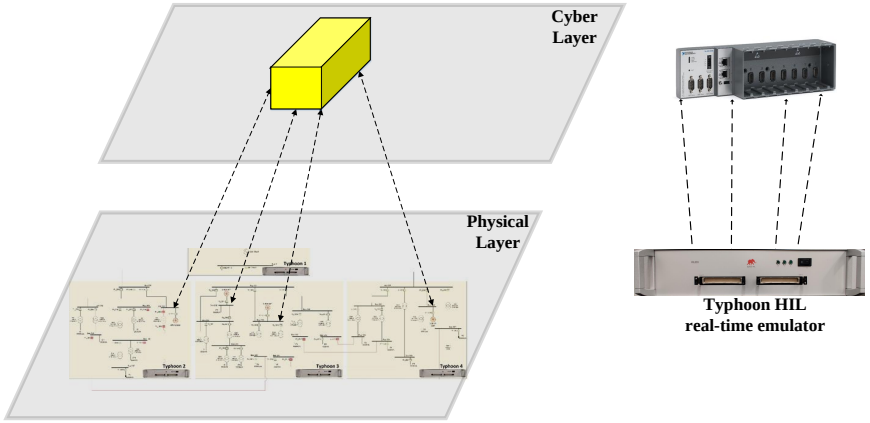

Figure 6.13: a) centralized computing node connected connected to DERs and b) the associated C-HIL setup

neighbors of that particular control node. For example, from Fig. 6.14, we can see that control nodel 1 (also the leader control node) can exchange information with the control node 2 and control node 4 and hence control nodes 2 and 4 are the nighbors of control node 1. Each distributed control node monitors and control their respective DERs modeled as part of Banshee network in the Typhoon HIL emulator as described in the physical layer of the test setup framework. The speed of the DER coordination depends on the communication graph employed in the setup. A complete commiunication graph where all control nodes can exchange information with each other can operate as fast as the centralized approach.

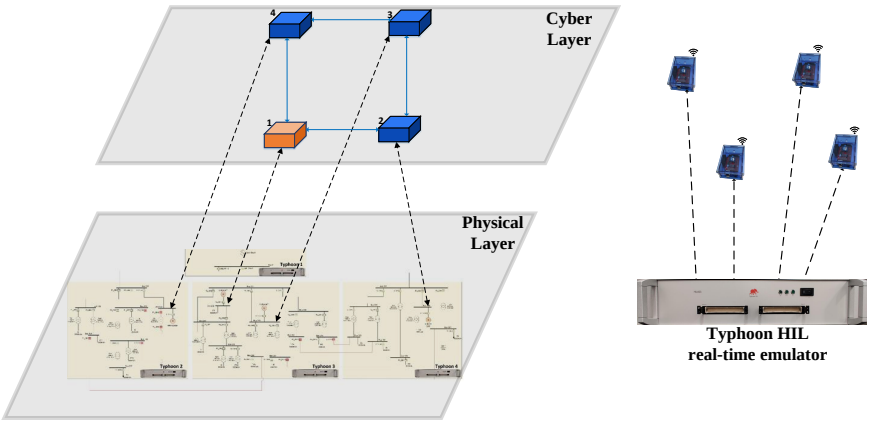

Figure 6.14: a) Four distributed control nodes connected to DERs and b) the associated C-HIL setup

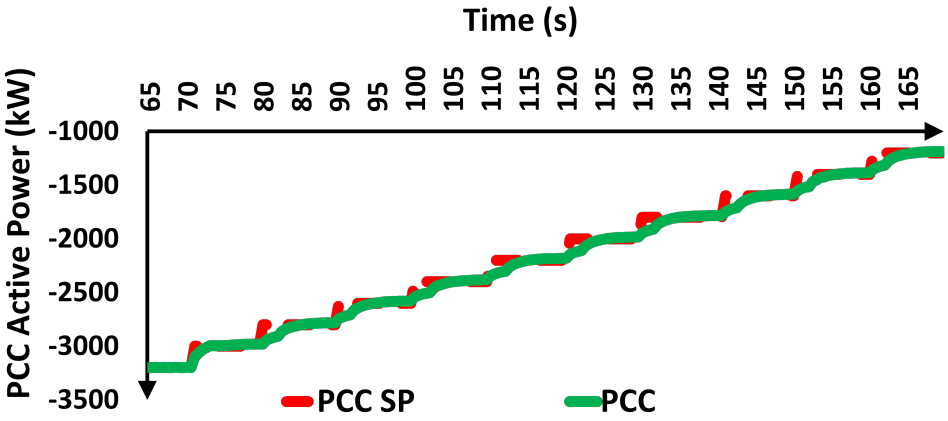

Figure 6.15: PCC active power injections

6.4.3 Centralized Results

In Fig. 6.15, we provide the results obtained from the C-HIL testing of the centralized approach utilized in the DER coordination problem. We plot the injections at the PCC bus in Fig. 6.15. At the 65 second mark the centralized controller starts receiving the tie-line regulation signal every 10 seconds. From Fig. 6.15, we can see how the DERs increase their generation to reduce the net injection by the bulk grid into Banshee system by 2 MW in about 100 seconds; thus, providing frequency regulation service to the external grid. The active power injection into the Banshee system at the 65 second mark is 3200 kW and in decrements of 200 kW, the active power injection at PCC bus drops down to 1200 kW. As shown in Fig. 6.15, the controller responds to the frequency regulation signals and coordinates the DERs to increase the generation within the microgrid in order to meet the regulation requirements.

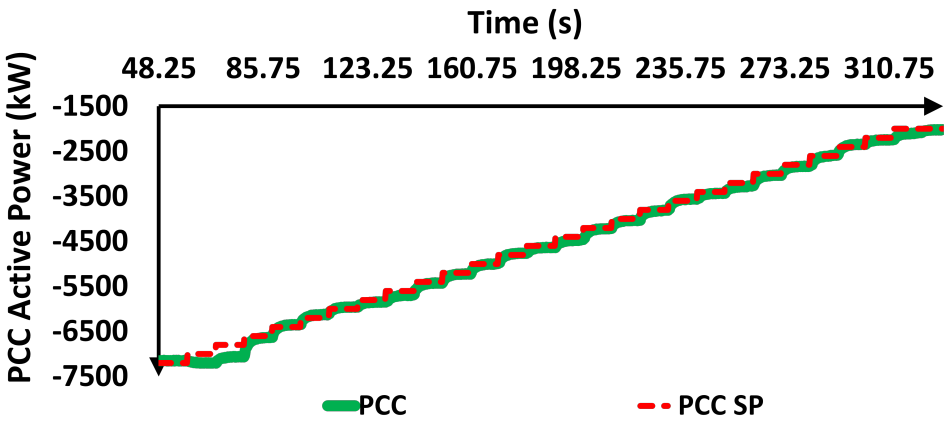

Figure 6.16: PCC active power injections

6.4.4 Distributed Results

In Fig. 6.16, we provide the results obtained from the CHIL testing of the distributed approach utilized in the DER coordination problem. We plot the active power injections at the PCC bus in Fig. 6.16. At the 50 second mark the leader control node (orange node in Fig. 6.14) starts receiving from the operator the tie-line active power mismatch every 10 seconds. From Fig. 6.16, we can see how the DERs are coordinated in a distributed fashion to track PCC active power set point which requires the injection from the bulk grid into the Banshee microgrid to be reduced by 5.2 MW in the space of four and a half minutes. The active power injection into the Banshee system at the 50 second mark is -7200 kW and in decrements of 200 kW, the active power injection at PCC bus drops down to -2000 kW and at the end of this regulation period the injection settles to 2 MW. As shown in Fig. 6.16, the distributed control nodes make use of local information and neighboring exchanges to respond to the frequency regulation signals and coordinates the four DERs to increase the generation within the microgrid in order to meet the regulation requirements.

7. Conclusions

This project aims at resolving several challenges in the DER-penetrated distribution power grids, including the voltage stability issues, transmission and distribution coordination for DER market participation, as well as centralized and distributed DER control for aggregated grid services provision. The report focuses on three core areas: 1) mitigating FIDVR events by using VFD driven air conditioners and DERs; 2) transmission and distribution coordination for enabling the wholesale market participation of DERs while ensuring distribution grid operation security and reliability; and 3) centralized and distributed coordination of DERs for the aggregated provision of frequency regulation services. The following works are presented in this report.

- FIDVR mitigation techniques by using DERs and VFD driven air conditioners are proposed. By properly modeling the VFD driven air conditioners, which is a relatively new technology in residential air conditioning, in the composite dynamic load models, this project investigates the impact of increasing VFD driven air conditioner penetration and DER penetration within a large-scale power system on reducing the severity of FIDVR events.
- The transmission and distribution coordination frameworks are proposed, which enables the wholesale market participation of massive DERs while ensuring secure operation of the distribution grids. A non-profit distribution system operator (DSO) is adopted as the coordinator between the wholesale market operation and the distribution grid operation. A parametric programming approach and a two-stage stochastic programming approach are proposed for the DSO to coordinate the wholesale market participation of aggregated DERs while satisfying the distribution grid operating constraints.
- The centralized and distributed methodologies which enable the coordination of multiple DERs are presented and implemented in order for the aggregated DERs to provide frequency regulation services to the bulk power systems. Details on the controller hardware-in-the-loop (CHIL) testbed that is used to test the centralized and distributed DER coordination approaches are presented in this project.

A. Appendix: Ratio Consensus Algorithm

The ratio-consensus algorithm serves as a primitive for solving many coordination and control problems in a distributed fashion [102–106]. Here, we discuss a variant of the original algorithm proposed in [107, 108] that is robust against packet drops in the communication links; this robust variant has been implemented in the C-HIL testbed.

A.1 Cyber Layer Model

The communication network interconnect the control nodes by a directed graph $\mathcal{G}_c = \{\mathcal{V}_c, \mathcal{E}_c\}$, where $\mathcal{V}_c := \{1, 2, \ldots, N\}$ is the vertex set, with each vertex—or node—corresponding to a DER or load; and where $\mathcal{E}_c \subseteq \mathcal{V}_c \times \mathcal{V}_c$ is the edge set, with the ordered pair $(i, j) \in \mathcal{E}_c$ if node i can receive information from node j. For notational convenience, we require self-loops for all nodes, that is, $(i, i) \in \mathcal{E}_c$, $\forall i \in \mathcal{V}_c$.

We define the set of vertices from which the local controller of DER i can receive information to be $\mathcal{N}_i^- := \{j \in \mathcal{V}_c : (i, j) \in \mathcal{E}_c\}$. Similarly, we define the set of vertices to which i can send information to be $\mathcal{N}_i^+ := \{j \in \mathcal{V}_c : (j, i) \in \mathcal{E}_c\}$, and we refer to $\mathcal{N}_i^-$ and $\mathcal{N}_i^+$ as the in- and out-neighborhood of node i, respectively. Furthermore, we denote the cardinality of the out-neighborhood, referred to as the out-degree, of node i as $\mathcal{D}_i^+ := |\mathcal{N}_i^+|$. Throughout the remainder, we assume that the directed graph $\mathcal{G}_c$ is strongly connected.

A.2 The Ratio-Consensus Algorithm

Consider a microgrid with n DERs and assume that the communication network describing the exchange of information between them can be described by the graph-theoretic model described above, i.e., a strongly connected graph $\mathcal{G}_c = \{\mathcal{V}_c, \mathcal{E}_c\}$. The local controller of each DER i participating in the ratio-consensus algorithm maintains two values, y_i and z_i, referred to as internal states, which are (independently) updated at each iteration to be a linear combination of the previous internal states of all nodes in its in-neighborhood. Specifically, for each iteration $k \geq 0$, node i updates its internal states as

$$y_i[k+1] = \sum_{j \in \mathcal{N}_i^-} \frac{1}{\mathcal{D}_j^+} y_j[k], \tag{A.1}$$

$$z_i[k+1] = \sum_{j \in \mathcal{N}_i^-} \frac{1}{\mathcal{D}_j^+} z_j[k], \tag{A.2}$$

where $\mathcal{D}_j^+$ is the out-degree of DER $j \in \mathcal{N}_i^-$. Note that given the self-loop requirement, the update for each internal state includes a weighted value of the previous local internal state of each node. Assuming that $z_i[k] \neq 0$, $\forall k$, at each iteration, the local controller of generator i computes

$$\gamma_i[k] = \frac{y_i[k]}{z_i[k]}. \tag{A.3}$$

Let $y_i[k],\ \forall i$, be the result of iteration (A.1) for some $y_i[0],\ \forall i$, and $z_i[k],\ \forall i$, be the result of iteration (A.2) for some $z_i[0]$, where $z_i[0] > 0,\ \forall i$; then, we have that $\lim_{k\to\infty} \gamma_i[k] = \frac{\sum_{j=1}^{n} y_j[0]}{\sum_{j=1}^{n} z_j[0]},\ \forall i$ (see [102] for a proof).

A.2.1 Robust Implementation

Rather than broadcast the latest state values as in (A.1) – (A.2), nodes participating in the modified ratio-consensus algorithm broadcast the sum of the weighted states up to and including the current iteration k. For the case when all links are available, i.e., no packets are lost, the weighted states for iteration k can be inferred from the information a DER receives from its in-neighbors. If a link is temporarily unavailable, however, the modification to the algorithm allows the receiving nodes to recover any lost information at the next successful iteration.

As before, each node maintains two states, $y_i[k]$ and $z_i[k]$, that are updated at each iteration. Using the modified algorithm, however, each node maintains two additional states, $\mu_i[k]$ and $\sigma_i[k]$, which are the values broadcasted to the out-neighbors of DER i at iteration k. The values of $\mu_i[k]$ and $\sigma_i[k]$ are the sum of $y_i[k]/\mathcal{D}_i^+$ and $z_i[k]/\mathcal{D}_i^+$ since the iterative process began, and thus, they are updated as follows:

$$\mu_i[k+1] = \mu_i[k] + \frac{1}{\mathcal{D}_i^+} y_i[k] = \sum_{t=0}^{k} \frac{1}{\mathcal{D}_i^+} y_i[t], \tag{A.4}$$

$$\sigma_i[k+1] = \sigma_i[k] + \frac{1}{\mathcal{D}_i^+} z_i[k] = \sum_{t=0}^{k} \frac{1}{\mathcal{D}_i^+} z_i[t], \tag{A.5}$$

with $\mu_i[0] = 0$ and $\sigma_i[0] = 0$. To account for the fact that the values received from in-neighbors are accumulated sums, each DER i updates its states as

$$\begin{aligned} y_i[k+1] &= \frac{1}{\mathcal{D}_i^+} y_i[k] + \sum_{\substack{j\in\mathcal{N}_i^- \\ i\neq j}} (\nu_{ij}[k+1] - \nu_{ij}[k]), \\ z_i[k+1] &= \frac{1}{\mathcal{D}_i^+} z_i[k] + \sum_{\substack{j\in\mathcal{N}_i^- \\ i\neq j}} (\tau_{ij}[k+1] - \tau_{ij}[k]), \end{aligned} \tag{A.6}$$

where the values of $\nu_{ij}[k+1]$ and $\tau_{ij}[k+1]$ depend on the successful receipt of a packet from

DER j during iteration k, and are given by[1]

$$\begin{aligned} \nu_{ij}[k+1] &= \begin{cases} \mu_j[k+1], & \text{if } (i,j) \in \mathcal{E}_c[k], \\ \nu_{ij}[k], & \text{if } (i,j) \notin \mathcal{E}_c[k], \end{cases} \\ \tau_{ij}[k+1] &= \begin{cases} \sigma_j[k+1], & \text{if } (i,j) \in \mathcal{E}_c[k], \\ \tau_{ij}[k], & \text{if } (i,j) \notin \mathcal{E}_c[k]. \end{cases} \end{aligned} \tag{A.7}$$

Under some mild assumptions, the algorithm above can be shown to be robust against communication packet drops, i.e., the nodes will eventually obtain $\frac{\sum_{j=1}^{n} y_j[0]}{\sum_{j=1}^{n} z_j[0]}$ with probability one (see [107,108] for a proof).

[1]In order to take into account for the possibility that communication links may not be available at every iteration, it is necessary to slightly modify the graph-theoretic model describing the exchange of information among DERs introduced earlier. To this end, we denote the graph representing the network interconnecting the DERs as $\mathcal{G}_c[k] = \{\mathcal{V}_c, \mathcal{E}_c[k]\}$, where $\mathcal{V}_c$ is independent of k as defined before, and $\mathcal{E}_c[k]$ is the set of edges where $(i,j) \in \mathcal{E}_c[k]$ if DER i can receive information from DER j at iteration k. We assume that $\mathcal{E}_c[k] \subseteq \mathcal{E}_c$, $\forall k \geq 0$, where $\mathcal{E}_c$ is as defined in Section A.1, and describes the scenario in which all communication links are available.

References

[1] "WECC composite load model specifications," 1 2015. [Online]. Available: https://www.wecc.org/_layouts/15/WopiFrame.aspx?sourcedoc/Reliability/WECC%20Composite%20Load%20Model%20Specifications%2001-27-2015.docx

[2] "WECC specifications for modeling distributed generation in power flow and dynamics," 2 2015. [Online]. Available: https://www.wecc.org/Reliability/IID%202020%20APR.pdf

[3] *Interconnection and Interoperability of Distributed Energy Resources with Associated Electric Power System Interfaces*, New York, NY, 2018, no. IEEE Std 1547-2018.

[4] *PSLF User Manual*, V22.0.1 ed., General Electric Inc., Schenectady, NY, 2021.

[5] M. Baker, "Air-conditioning was once taboo in seattle. not anymore." *The New York Times*, 6 2021. [Online]. Available: https://www.nytimes.com/2021/06/25/us/western-heat-wave.html

[6] M. Isaac and D. P. van Vuuren, "Modeling global residential sector energy demand for heating and air conditioning in the context of climate change," *Energy Policy*, vol. 37, no. 2, pp. 507–521, 2009. [Online]. Available: https://www.sciencedirect.com/science/article/pii/S0301421508005168

[7] R. J. Bravo, R. Yinger, and P. Arons, "Fault induced delayed voltage recovery (FIDVR) indicators," in *2014 IEEE PES T&D Conference and Exposition*, 2014, pp. 1–5.

[8] *Undervoltage Load Shedding*. North American Electric Reliability Corporation, 11 2015, no. PRC-010-1. [Online]. Available: https://www.nerc.com/pa/Stand/Reliability%20Standards/PRC-010-1.pdf

[9] *Load Shedding Plans*. North American Electric Reliability Corporation, 5 2012, no. EOP-003-2. [Online]. Available: https://www.nerc.com/files/EOP-003-2.pdf

[10] R. Bravo and S. Robles, *2012 FIDVR Events Analysis: Valley Distribution Circuits*. Lawrence Berkeley National Laboratory, 7 2013. [Online]. Available: https://eta.lbl.gov/publications/2012-fidvr-events-analysis-valley

[11] ——, *2013 FIDVR Events Analysis on Valley Distribution Circuits*. Lawrence Berkeley National Laboratory, 12 2013. [Online]. Available: https://eta.lbl.gov/publications/2013-fidvr-events-analysis-valley

[12] S. Robles, *2014 FIDVR Events Analysis on Valley Distribution Circuits*, 6 2015. [Online]. Available: https://eta.lbl.gov/publications/2014-fidvr-events-analysis-valley

[13] A. Gaikwad, *Technical Update on Load Modeling*. Palo Alto, CA: Electric Power Research Institute, 12 2018, no. 3002013562. [Online]. Available: https://www.epri.com/research/products/000000003002013562

[14] Y. Liu, V. Vittal, J. Undrill, and J. H. Eto, "Transient model of air-conditioner compressor single phase induction motor," *IEEE Transactions on Power Systems*, vol. 28, no. 4, pp. 4528–4536, 2013.

[15] Q. Huang and V. Vittal, "Application of electromagnetic transient-transient stability hybrid simulation to FIDVR study," *IEEE Transactions on Power Systems*, vol. 31, no. 4, pp. 2634–2646, 2016.

[16] S. Nekkalapu, V. Vittal, J. Undrill, B. Keel, B. Gong, and K. Brown, "Synthesis of load and feeder models using point on wave measurement data," *IEEE Open Access Journal of Power and Energy*, vol. 8, pp. 198–210, 2021.

[17] R. Bravo, R. Yinger, D. Chassin, H. Huang, N. Lu, I. Hiskens, and Venkataramanan, "Final project report load modeling transmission research," 3 2010.

[18] H. Bai and V. Ajjarapu, "A novel online load shedding strategy for mitigating fault-induced delayed voltage recovery," *IEEE Transactions on Power Systems*, vol. 26, no. 1, pp. 294–304, 2011.

[19] A. Joseph, M. Cvetković, and P. Palensky, "Predictive mitigation of short term voltage instability using a faster than real-time digital replica," in *2018 IEEE PES Innovative Smart Grid Technologies Conference Europe (ISGT-Europe)*, 2018, pp. 1–6.

[20] M. Paramasivam, A. Salloum, V. Ajjarapu, V. Vittal, N. B. Bhatt, and S. Liu, "Dynamic optimization based reactive power planning to mitigate slow voltage recovery and short term voltage instability," *IEEE Transactions on Power Systems*, vol. 28, no. 4, pp. 3865–3873, 2013.

[21] Y. Zhang, Y. Xu, Z. Y. Dong, and P. Zhang, "Real-time assessment of fault-induced delayed voltage recovery: A probabilistic self-adaptive data-driven method," *IEEE Transactions on Smart Grid*, vol. 10, no. 3, pp. 2485–2494, 2019.

[22] W. Hartmann, "Advanced feeder protection applications," in *2017 Annual Pulp, Paper And Forest Industries Technical Conference (PPFIC)*, 2017, pp. 1–6.

[23] P. Mitra, *Technical Reference on the Composite Load Model*. Palo Alto, CA: Electric Power Research Institute, 9 2020, no. 3002019209. [Online]. Available: https://www.epri.com/research/products/000000003002019209

[24] "Reliability guideline developing load model composition data," 2 2017. [Online]. Available: https://www.nerc.com/pa/RAPA/rg/ReliabilityGuidelines/Reliability_Guideline_-_Load_Model_Composition_-_2017-02-28.pdf

[25] W. Wang, M. Diaz-Aguiló, K. B. Mak, F. de León, D. Czarkowski, and R. E. Uosef, "Time series power flow framework for the analysis of FIDVR using linear regression," *IEEE Transactions on Power Delivery*, vol. 33, no. 6, pp. 2946–2955, 2018.

[26] R. J. Bravo and D. P. Chassin, "Fault induced delayed voltage recovery (FIDVR) model validation," in *2016 IEEE/PES Transmission and Distribution Conference and Exposition (T&D)*, 2016, pp. 1–4.

[27] "Load model data tool (LMDT)," 9 2019. [Online]. Available: https://svn.pnl.gov/LoadTool

[28] A. Gaikwad, P. Markham, and P. Pourbeik, "Implementation of the WECC composite load model for utilities using the component-based modeling approach," in *2016 IEEE/PES Transmission and Distribution Conference and Exposition (T&D)*, 2016, pp. 1–5.

[29] "Load component export tool (LCET) v3.1," 5 2019. [Online]. Available: https://www.epri.com/research/products/000000003002015441

[30] "Technical reference document dynamic load modeling," 12 2016. [Online]. Available: https://www.nerc.com/comm/PC/LoadModelingTaskForceDL/Dynamic%20Load%20Modeling%20Tech%20Ref%202016-11-14%20-%20FINAL.PDF

[31] P. Regulski, D. S. Vilchis-Rodriguez, S. Djurović, and V. Terzija, "Estimation of composite load model parameters using an improved particle swarm optimization method," *IEEE Transactions on Power Delivery*, vol. 30, no. 2, pp. 553–560, 2015.

[32] F. Bu, Z. Ma, Y. Yuan, and Z. Wang, "WECC composite load model parameter identification using evolutionary deep reinforcement learning," *IEEE Transactions on Smart Grid*, vol. 11, no. 6, pp. 5407–5417, 2020.

[33] S. Son, S. H. Lee, D.-H. Choi, K.-B. Song, J.-D. Park, Y.-H. Kwon, K. Hur, and J.-W. Park, "Improvement of composite load modeling based on parameter sensitivity and dependency analyses," *IEEE Transactions on Power Systems*, vol. 29, no. 1, pp. 242–250, 2014.

[34] K. Zhang, H. Zhu, and S. Guo, "Dependency analysis and improved parameter estimation for dynamic composite load modeling," in *2017 IEEE Power Energy Society General Meeting*, 2017, pp. 1–1.

[35] "Gridpack project on github," 01 2020. [Online]. Available: https://github.com/GridOPTICS/GridPACK

[36] S. Djokic, J. Milanovic, and D. Kirschen, "Sensitivity of ac coil contactors to voltage sags, short interruptions, and undervoltage transients," *IEEE Transactions on Power Delivery*, vol. 19, no. 3, pp. 1299–1307, 2004.

[37] A. Honrubia Escribano, E. Gómez-Lázaro, G. Jiménez-Moreno, and A. Molina-García, "Analysis of the ac-contactor electrical behavior under voltage dips," in *The XIX International Conference on Electrical Machines - ICEM 2010*, 2010, pp. 1–5.

[38] G. Karady, S. Saksena, B. Shi, and N. Senroy, *Effects of Voltage Sags on Loads in a Distribution System*. Tempe, AZ: Power Systems Engineering Research Center, 10 2005, vol. 05–63. [Online]. Available: https://pserc.wisc.edu/wp-content/uploads/sites/755/2018/08/T-16_Final-Report_Oct-2005.pdf

[39] Y. Li, *Variable Frequency Drive Applications in HVAC Systems*. InTech, 12 2015. [Online]. Available: http://www.intechopen.com/books/new-applications-of-electric-drives/variable-frequency-drive-applications-in-hvac-systems

[40] "HVAC packaged unit vs. split system: Differences, benefits, and how to choose." [Online]. Available: https://www.petro.com/resource-center/hvac-packaged-unit-vs-split-system

[41] R. J. Bravo and M. Norwalk, "Dynamic performance of air conditioners with variable frequency drive," in *2016 IEEE/PES Transmission and Distribution Conference and Exposition (T&D)*, 2016, pp. 1–5.

[42] P. Mitra, D. Ramasubramanian, A. Gaikwad, and J. Johns, "Modeling the aggregated response of variable frequency drives (VFDs) for power system dynamic studies," *IEEE Transactions on Power Systems*, vol. 35, no. 4, pp. 2631–2641, 2020.

[43] "Central air conditioning." [Online]. Available: https://www.energy.gov/energysaver/central-air-conditioning

[44] B. Sapkota, "Voltage stability assessment and enhancement of a large power system using static and dynamic approaches," Ph.D. dissertation, Arizona State University, Tempe, AZ, 5 2010.

[45] "Solar power will account for nearly half of new u.s. electric generating capacity in 2022," 01 2022. [Online]. Available: https://www.eia.gov/todayinenergy/detail.php?id=50818

[46] P. Gagnon, R. Margolis, and C. Phillips, "Rooftop photovoltaic technical potential in the united states," 11 2019. [Online]. Available: https://www.osti.gov/biblio/1575064

[47] "Technical requirements for generating facilities interconnecting to the distribution system," 2012.

[48] "Distributed generation interconnection handbook," 02 2022. [Online]. Available: https://srpnet.com/menu/electricbiz/PDFX/Distributed_Generation_Interconnection_Handbook.pdf

[49] R. K. Varma and S. Mohan, "Mitigation of fault induced delayed voltage recovery (FIDVR) by PV-STATCOM," *IEEE Transactions on Power Systems*, vol. 35, no. 6, pp. 4251–4262, 2020.

[50] B. Park and M. M. Olama, "Mitigation of motor stalling and FIDVR via energy storage systems with signal temporal logic," *IEEE Transactions on Power Systems*, vol. 36, no. 2, pp. 1164–1174, 2021.

[51] W. Wang and F. de León, "Quantitative evaluation of DER smart inverters for the mitigation of FIDVR in distribution systems," *IEEE Transactions on Power Delivery*, vol. 35, no. 1, pp. 420–429, 2020.

[52] P. Pourbek, *PROPOSAL FOR DER_A MODEL*, 10 2016. [Online]. Available: https://www.wecc.org/Reliability/DER_A_Final_061919.pdf

[53] *Reliability Guideline Parameterization of the DER_A Model*. Atlanta, GA: North American Electric Reliability Corporation, 9 2019. [Online]. Available: https://www.nerc.com/comm/PC_Reliability_Guidelines_DL/Reliability_Guideline_DER_A_Parameterization.pdf

[54] Z. Ma, Z. Wang, Y. Wang, R. Diao, and D. Shi, "Mathematical representation of WECC composite load model," *Journal of Modern Power Systems and Clean Energy*, vol. 8, no. 5, pp. 1015–1023, 2020.

[55] *Reliability Guideline DER Data Collection for Modeling in Transmission Planning Studies*. Atlanta, GA: North American Electric Reliability Corporation, 9 2020. [Online]. Available: https://www.nerc.com/comm/PC_Reliability_Guidelines_DL/Reliability_Guideline_DER_Data_Collection_for_Modeling.pdf

[56] *Standard for Interconnecting Distributed Resources with Electric Power Systems*, New York, NY, 2003, no. IEEE Std 1547-2003.

[57] *Reliability Guideline Bulk Power System Reliability Perspectives on the Adoption of IEEE 1547-2018*. Atlanta, GA: North American Electric Reliability Corporation, 3 2019. [Online]. Available: https://www.nerc.com/comm/PC_Reliability_Guidelines_DL/Guideline_IEEE_1547-2018_BPS_Perspectives.pdf

[58] *Standard for Interconnecting Distributed Resources with Electric Power Systems*, New York, NY, 2014, no. IEEE Std 1547-2014a.

[59] "Rule 21 interconnection," 2022. [Online]. Available: https://www.cpuc.ca.gov/Rule21/

[60] *Standard for Inverters, Converters, Controllers and Interconnection System Equipment for Use With Distributed Energy Resources*. Northbrook, IL: Underwriter's Laboratories, Inc, 9 2021. [Online]. Available: https://standardscatalog.ul.com/ProductDetail.aspx?productId=UL1741

[61] *Standard Conformance Test Procedures for Equipment Interconnecting Distributed Energy Resources with Electric Power Systems and Associated Interfaces*, New York, NY, 2020, no. IEEE Std 1547.1-2020.

[62] A. Cisco Sullberg, M. Wu, V. Vittal, B. Gong, and P. Augustin, "Examination of composite load and variable frequency drive air conditioning modeling on FIDVR," *IEEE Open Access Journal of Power and Energy*, vol. 8, pp. 147–156, 2021.

[63] Federal Energy Regulatory Commission, "Order no. 2222: Participation of distributed energy resource aggregations in markets operated by regional transmission organizations and independent system operators," 2020.

[64] M. Mousavi and M. Wu, "A dso framework for market participation of der aggregators in unbalanced distribution networks," *IEEE Transactions on Power Systems*, 2021.

[65] H. Chen, L. Fu, L. Bai, T. Jiang, Y. Xue, R. Zhang, B. Chowdhury, J. Stekli, and X. Li, "Distribution market-clearing and pricing considering coordination of dsos and iso: An epec approach," *IEEE Trans. Smart Grid*, 2021.

[66] A. Hassan and Y. Dvorkin, "Energy storage siting and sizing in coordinated distribution and transmission systems," *IEEE Trans. Sustain. Energy*, vol. 9, no. 4, pp. 1692–1701, 2018.

[67] F. Moret, A. Tosatto, T. Baroche, and P. Pinson, "Loss allocation in joint transmission and distribution peer-to-peer markets," *IEEE Transactions on Power Systems*, vol. 36, no. 3, pp. 1833–1842, 2020.

[68] Y. K. Renani, M. Ehsan, and M. Shahidehpour, "Optimal transactive market operations with distribution system operators," *IEEE Transactions on Smart Grid*, vol. 9, no. 6, pp. 6692–6701, 2017.

[69] S. Wang, B. Sun, X. Tan, T. Liu, and D. H. Tsang, "Real-time coordination of transmission and distribution networks via nash bargaining solution," *IEEE Trans. Sustain. Energy*, 2021.

[70] S. Yin, J. Wang, and H. Gangammanavar, "Stochastic market operation for coordinated transmission and distribution systems," *IEEE Trans. Sustain. Energy*, 2021.

[71] R. Haider, S. Baros, Y. Wasa, J. Romvary, K. Uchida, and A. M. Annaswamy, "Toward a retail market for distribution grids," *IEEE Transactions on Smart Grid*, vol. 11, no. 6, pp. 4891–4905, 2020.

[72] M. Bragin and Y. Dvorkin, "Tso-dso operational planning coordination through l 1-proximal surrogate lagrangian relaxation," *IEEE Transactions on Power Systems*, 2021.

[73] M. Khodadadi, M. H. Golshan, and M. P. Moghaddam, "Non-cooperative operation of transmission and distribution systems," *IEEE Trans. Ind. Informat.*, 2020.

[74] A. Bemporad and C. Filippi, "An algorithm for approximate multiparametric convex programming," *Computational optimization and applications*, vol. 35, no. 1, pp. 87–108, 2006.

[75] F. Borrelli, A. Bemporad, and M. Morari, "Geometric algorithm for multiparametric linear programming," *Journal of optimization theory and applications*, vol. 118, no. 3, pp. 515–540, 2003.

[76] T. Gal and J. Nedoma, "Multiparametric linear programming," *Management Science*, vol. 18, no. 7, pp. 406–422, 1972.

[77] M. Kvasnica, P. Grieder, and M. Baotić, "Multi-Parametric Toolbox (MPT)," 2004. [Online]. Available: http://control.ee.ethz.ch/~mpt/

[78] J. Löfberg, "Yalmip : A toolbox for modeling and optimization in matlab," in *In Proceedings of the CACSD Conference*, Taipei, Taiwan, 2004.

[79] R. Oberdieck, N. A. Diangelakis, M. M. Papathanasiou, I. Nascu, and E. N. Pistikopoulos, "Pop–parametric optimization toolbox," *Industrial & Engineering Chemistry Research*, vol. 55, no. 33, pp. 8979–8991, 2016.

[80] M. Di Somma, G. Graditi, and P. Siano, "Optimal bidding strategy for a der aggregator in the day-ahead market in the presence of demand flexibility," *IEEE Trans. Ind. Electron.*, vol. 66, no. 2, pp. 1509–1519, Feb 2019.

[81] A. Baringo, L. Baringo, and J. M. Arroyo, "Day-ahead self-scheduling of a virtual power plant in energy and reserve electricity markets under uncertainty," *IEEE Trans. Power Syst.*, vol. 34, no. 3, pp. 1881–1894, May 2019.

[82] M. F. Anjos, A. Lodi, and M. Tanneau, "A decentralized framework for the optimal coordination of distributed energy resources," *IEEE Trans. Power Syst.*, vol. 34, no. 1, pp. 349–359, Jan 2019.

[83] G. Liu, Y. Xu, and K. Tomsovic, "Bidding strategy for microgrid in day-ahead market based on hybrid stochastic/robust optimization," *IEEE Trans. on Smart Grid*, vol. 7, no. 1, pp. 227–237, Jan 2016.

[84] F. Lezama, J. Soares, P. Hernandez-Leal, M. Kaisers, T. Pinto, and Z. Vale, "Local energy markets: Paving the path toward fully transactive energy systems," *IEEE Trans. Power Syst.*, vol. 34, no. 5, pp. 4081–4088, Sep. 2019.

[85] H. T. Nguyen, L. B. Le, and Z. Wang, "A bidding strategy for virtual power plants with the intraday demand response exchange market using the stochastic programming," *IEEE Trans. Ind. Appl.*, vol. 54, no. 4, pp. 3044–3055, July 2018.

[86] H. Yang, S. Zhang, J. Qiu, D. Qiu, M. Lai, and Z. Dong, "Cvar-constrained optimal bidding of electric vehicle aggregators in day-ahead and real-time markets," *IEEE Trans. Ind. Informat.*, vol. 13, no. 5, pp. 2555–2565, Oct 2017.

[87] M. N. Faqiry, A. K. Zarabie, F. Nassery, H. Wu, and S. Das, "A day-ahead market energy auction for distribution system operation," in *2017 IEEE International Conference on Electro Information Technology (EIT)*, May 2017, pp. 182–187.

[88] J. C. do Prado, H. Vakilzadian, W. Qiao, and D. P. F. Möller, "Stochastic distribution system market clearing and settlement via sample average approximation," in *2018 North American Power Symposium (NAPS)*, Sep. 2018, pp. 1–6.

[89] S. Parhizi and A. Khodaei, "Interdependency of transmission and distribution pricing," in *2016 IEEE Power Energy Society Innovative Smart Grid Technologies Conference (ISGT)*, Sep. 2016, pp. 1–5.

[90] California iso. [Online]. Available: https://goo.gl/bBGvVG

[91] R. Khalilisenobari and M. Wu, "Optimal participation of price-maker battery energy storage systems in energy, reserve and pay as performance regulation markets," in *2019 North American Power Symposium (NAPS)*, 2019, pp. 1–6.

[92] J. Zhao, T. Zheng, E. Litvinov, F. Zhao, and I. N. England, "Pricing schemes for two-stage market clearing models," in *Technical Conference: Increasing Real-Time and Day-Ahead Market Efficiency through Improved Software, FERC*, 2013.

[93] A. Sadeghi-Mobarakeh, A. Shahsavari, H. Haghighat, and H. Mohsenian-Rad, "Optimal market participation of distributed load resources under distribution network operational limits and renewable generation uncertainties," *IEEE Trans. on Smart Grid*, vol. 10, no. 4, pp. 3549–3561, July 2019.

[94] J. M. Morales, A. J. Conejo, H. Madsen, P. Pinson, and M. Zugno, *Integrating renewables in electricity markets: operational problems*. Springer Science & Business Media, 2013, vol. 205.

[95] M. E. Baran and F. F. Wu, "Network reconfiguration in distribution systems for loss reduction and load balancing," *IEEE Trans. Power Del.*, vol. 4, no. 2, pp. 1401–1407, April 1989.

[96] M. Mousavi, M. Rayati, and A. M. Ranjbar, "Optimal operation of a virtual power plant in frequency constrained electricity market," *IET Gener. Transm. Distrib.*, vol. 13, no. 11, pp. 2123–2133, 2019.

[97] M. Mousavi and M. Wu, "A dso framework for comprehensive market participation of der aggregators," *arXiv preprint arXiv:2006.06673*, 2020.

[98] R. Salcedo, E. Corbett, C. Smith, E. Limpaecher, R. Rekha, J. Nowocin, G. Lauss, E. Fonkwe, M. Almeida, P. Gartner, S. Manson, B. Nayak, I. Celanovic, C. Dufour, M. O. Faruque, K. Schoder, R. Brandl, P. Kotsampopoulos, T. Ham Ha, A. Davoudi, A. Dehkordi, and K. Strunz, "Banshee distribution network benchmark and prototyping platform for hardware-in-the-loop integration of microgrid and device controllers," *The Journal of Engineering*, vol. 2019, no. 8, pp. 5365–5373, 2019.

[99] S. C. Utomi, "Hardware-in-the-loop platform for the coordination of distributed energy resources to provide frequency regulation services," Master's thesis, University of Illinois at Urbana-Champaign, Apr. 2018.

[100] O. Azofeifa, S. Nigam, O. Ajala, C. Sain, S. Utomi, A. D. Domínguez-García, and P. W. Sauer, "Controller hardware-in-the-loop testbed for distributed coordination and control architectures," in *Proc. of North American Power Symposium, Wichita, KS*, Oct. 2019.

[101] PJM. (2019, Mar.) Normalized signal test: RegD. [Online]. Available: https://www.pjm.com/markets-and-operations/ancillary-services.aspx

[102] A. D. Domínguez-García and C. N. Hadjicostis, "Distributed algorithms for control of demand response and distributed energy resources," in *Proc. of the IEEE Conference on Decision and Control*, 2011, pp. 27–32.

[103] S. T. Cady, A. D. Domínguez-García, and C. N. Hadjicostis, "Robust implementation of distributed algorithms for control of distributed energy resources," in *Proc. of the North American Power Symposium*, 2011, pp. 1–5.

[104] A. D. Domínguez-García, S. T. Cady, and C. N. Hadjicostis, "Decentralized optimal dispatch of distributed energy resources," in *Proc. of the IEEE Conference on Decision and Control*, 2012, pp. 3688–3693.

[105] B. A. Robbins, C. N. Hadjicostis, and A. D. Domínguez-García, "A two-stage distributed architecture for voltage control in power distribution systems," *IEEE Transactions on Power Systems*, vol. 28, no. 2, pp. 1470–1482, May 2013.

[106] S. T. Cady, A. D. Domínguez-García, and C. N. Hadjicostis, "A distributed generation control architecture for islanded ac microgrids," *IEEE Transactions on Control Systems Technology*, vol. 23, no. 5, pp. 1717–1735, Sep. 2015.

[107] A. D. Domínguez-García, C. N. Hadjicostis, and N. Vaidya, "Resilient networked control of distributed energy resources," *IEEE Journal on Selected Areas in Comm.*, vol. 30, no. 6, pp. 1137–1148, July 2012.

[108] C. N. Hadjicostis, N. Vaidya, and A. D. Domínguez-García, "Robust distributed average consensus via exchange of running sums," *IEEE Transactions on Automatic Control*, vol. 61, no. 6, pp. 1492–1507, June 2016.